

Aus der Klinik und Poliklinik für Nuklearmedizin
Klinik der Ludwig-Maximilians-Universität München

Direktor: Prof. Dr. med. Peter Bartenstein

**Binding Characteristics of Next Generation
Tau-Positron-Emission-Tomography to Improve
Differential Diagnosis of Neurodegenerative Disorders**

Dissertation

zum Erwerb des Doktorgrades der Medizin
an der Medizinischen Fakultät der
Ludwig-Maximilians-Universität zu München



vorgelegt von
Mengmeng Song
aus
Shandong, V.R. China
2021

Mit Genehmigung der Medizinischen Fakultät
der Universität München

Berichterstatter: Priv.-Doz. Dr. med. Matthias Brendel

Mitberichterstatter: Priv.-Doz. Dr. med. Andreas Zwergal
Prof. Dr. med. Oliver Pogarell

Mitbetreuung durch den
promovierten Mitarbeiter: Dr. Leonie Beyer

Dekan: Prof. Dr. med. Thomas Gudermann

Tag der mündlichen Prüfung: 20.10. 2021

Affidavit



Affidavit

Song, Mengmeng

Surname, first name

Street

Zip code, town, country

I hereby declare, that the submitted thesis entitled:

Binding Characteristics of Next Generation Tau-Positron-Emission-Tomography to Improve Differential Diagnosis of Neurodegenerative Disorders

is my own work. I have only used the sources indicated and have not made unauthorized use of services of a third party. Where the work of others has been quoted or reproduced, the source is always given.

I further declare that the submitted thesis or parts thereof have not been presented as part of an examination degree to any other university.

Munich, 22.04.2021

place, date

Mengmeng Song

Signature doctoral candidate

Table of content

AFFIDAVIT	3
TABLE OF CONTENT	4
LIST OF ABBREVIATIONS.....	5
LIST OF PUBLICATIONS	6
1. CONTRIBUTION TO THE PUBLICATIONS.....	7
1.1 CONTRIBUTION TO PAPER I	7
1.2 CONTRIBUTION TO PAPER II.....	7
2. INTRODUCTION.....	8
2.1 TAUOPATHIES.....	8
2.1.1 <i>Tau protein</i>	9
2.1.2 <i>Classification of tauopathies</i>	10
2.1.3 <i>Neuropathology of AD, PSP, and CBD</i>	11
2.1.4 <i>Tau Positron Emission Tomography (tau-PET) imaging</i>	12
2.2 THE FIRST-GENERATION TAU-PET RADIOTRACERS.....	13
2.2.1 <i>Clinical application in Alzheimer's disease</i>	13
2.2.2 <i>Clinical application in non-AD tauopathies</i>	15
2.2.3 <i>Limitations and challenges</i>	16
2.3 [¹⁸ F]PI-2620, A SECOND-GENERATION TAU-PET RADIOTRACER.....	17
2.3.1 <i>Preclinical study of [¹⁸F]PI-2620</i>	18
2.3.2 <i>Clinical application of [¹⁸F]PI-2620</i>	19
3. SUMMARY (ENGLISCH).....	22
4. ZUSAMMENFASSUNG (DEUTSCH)	24
5. PAPER I	26
6. PAPER II	42
REFERENCES	54
ACKNOWLEDGEMENTS.....	62

List of abbreviations

AD	Alzheimer's disease
AGD	argyrophilic grain disease
A β	amyloid-beta
CBD	corticobasal degeneration
CBS	corticobasal syndrome
HCs	healthy controls
MAO	monoamine oxidases
MAPT	microtubule-associated protein tau
MCI	mild cognitive impairment
NDC	non-demented control
NFTs	neurofibrillary tangles
PD	Parkinson's disease
PET	positron emission tomography
PHFs	paired helical filaments
PiD	Pick's disease
PSP	progressive supranuclear palsy
PSPRS	PSP rating scale
PSP-RS	PSP Richardson syndrome
ROIs	regions of interest
SPs	senile plaques
TDP-43	transactivation response DNA binding protein 43
SUVR	standardized-uptake-value-ratio

List of publications

1. Song, M., et al. Binding characteristics of [18F]PI-2620 distinguish the clinically predicted tau isoform in different tauopathies by PET. *Journal of Cerebral Blood Flow & Metabolism*, 2021. 41(11): p. 2957–2972.
2. Beyer, L., et al. Early-phase [18F]PI-2620 tau-PET imaging as a surrogate marker of neuronal injury. *Eur J Nucl Med Mol Imaging*, 2020. 47(12): p. 2911-2922.

1. Contribution to the publications

1.1 Contribution to paper I

For the paper entitled “Binding characteristics of [¹⁸F]PI-2620 distinguish the clinically predicted tau isoform in different tauopathies by PET”, I retrieved data from PACS, performed image pre and post-processing and all data analysis. I drafted the manuscript together with the senior author, and contributed to the revision of the manuscript for important intellectual content. The data analysis and the study design were based on the intellectual discussion between me and the senior author. I designed all figures and tables.

1.2 Contribution to paper II

As a co-author of the paper entitled “Early-phase [¹⁸F]PI-2620 tau-PET imaging as a surrogate marker of neuronal injury” , I performed data retrieval and subsequent image post-processing, including spatial normalization and kinetic modelling maps generation. I drafted the manuscript and added intellectual content.

2. Introduction

2.1 Tauopathies

With aging populations in industrialized nations, neurodegenerative disorders are gradually being paid more attention. This is a worrying problem since such diseases have both significant social and economic impact in terms of direct medical and accompanying social care costs.

Neurodegenerative disorders are described as diseases with chronic and advancing loss of neuronal structure or function ranges from initial synaptic dysfunction to extensive neuron death in the central and peripheral nervous system [1]. These disorders can be broadly classified by their clinical symptoms, with movement disorders and impaired cognitive function being the most common features [2-4]. However, most patients usually have mixed clinical features rather than a pure syndrome presentation [3]. On the other hand, neurodegenerative diseases can also be categorized and termed according to a variety of modified and deposited proteins which play a major role in disease neuropathology [4], such as tauopathies, α -synucleinopathies, amyloid-beta ($A\beta$) proteinopathies, and transactivation response DNA binding protein-43 (TDP-43) proteinopathies, etc. [2, 3, 5]. Thus, currently there is a mixture between clinical and biomolecular definition of neurodegenerative disorders.

Disorders associated with pathological tau protein accumulation in neurons and glia are termed tauopathies [6-11]. The pathological accumulation of misfolded hyperphosphorylated tau is a hallmark of a various of neurodegenerative diseases, such as Alzheimer's disease (AD), Pick's disease (PiD), some of atypical parkinsonian syndromes, subtypes of frontotemporal dementia, etc. [12, 13].

Although current treatments are still not able to cure or change the progressive course of tauopathies, but can only relieve the related symptoms [14], scientific research has

achieved huge progress not only in better understanding the disease mechanisms but also in diagnosing early stages of neurodegeneration diseases by biomarkers.

2.1.1 Tau protein

Tau is a microtubule-associated protein tau (*MAPT*) gene-encoded protein [15] which is primarily located in nerve cell axons in neurons [16] and contribute to the formation of the core of early assembling microtubules, as well as control microtubular stability and regulate its transport processes [6, 17-20].

Tau isoforms are expressed by alternate splicing of pre-mRNA. In the adult human brain, six tau isoforms with different length (from 352 to 441 amino acids) have been reported [6, 16, 21-26]. These isoforms differ in the inclusion of an exons 2 and 3 encoded amino acid sequence insert, as well as in the existence of an exon 10 encoded repeat segment which serves as a microtubule-binding domain [16, 22, 27-29]. Depending on the inclusion or exclusion of the exon 10 encoded microtubule-binding domain repeat, tau protein is divided into four repeats (4R) or three repeats (3R) isoforms respectively [3, 11, 16, 21, 25-27, 30]. In normal condition, 3R and 4R tau isoforms are equal in amount in the brain. The splicing of six different tau protein isoforms is illustrated in **Figure 1**.

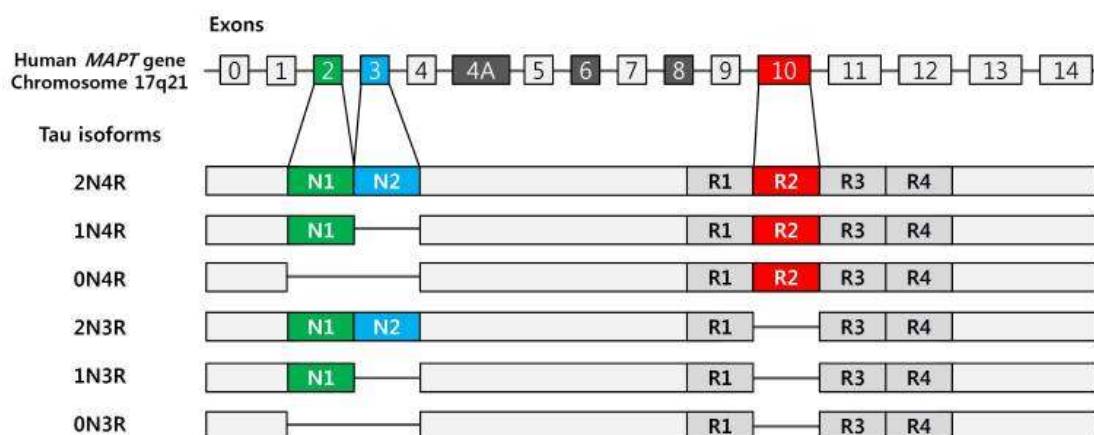


Figure 1. Six tau isoforms expressed in the adult human brain. Tau is encoded by the human *MAPT* gene on chromosome 17q21. N1 (green) and N2 (blue) are expressed

by the alternative splicing of exons 2 and 3 respectively, resulting different number of inserts (0/1/2N). Depending on the inclusion or exclusion of the R2 (red) insert, tau isoforms are thus divided into 3R- or 4R-tau, respectively. (From Park et al., BMB Rep 2016 [31])

Tau is natively unfolded and normally phosphorylated [18, 32]. Under pathological conditions, however, tau is abnormally hyperphosphorylated [33]. The specific mechanisms underlying pathologically tau aggregation are yet to be investigated, however, it is reported that the hyperphosphorylation of tau debilitate its microtubules binding while raise tau protein level in cytosol [34], resulting in protein self-aggregation and neurofibrillary tangles (NFTs) formation [26], which are further classified as paired helical filaments (PHFs), twisted ribbons, and/or straight filaments [33, 35].

2.1.2 Classification of tauopathies

Although all tauopathies share tau immunoreactivity in postmortem analysis, tauopathies are heterogeneous in both biochemistry and morphology.

On one hand, tauopathies can be biochemically categorized according to the different tau isoform compositions of their filaments, thus being subdivided into 3R tauopathies predominantly composing of 3R tau, 4R tauopathies predominantly composing of 4R tau, and 3R/4R-tauopathies in which NFTs contain a mixture of 3R and 4R tau [11, 36, 37].

On the other hand, tauopathies can be categorized depending on the primary driver. In primary tauopathies, tau is the principal pathogenic protein, whereas other etiologies contribute, even primarily, to secondary tauopathies. Primary tauopathies consist pure 3R-tauopathies (e.g., Pick's disease), pure 4R-tauopathies (e.g., progressive supranuclear palsy (PSP), corticobasal degeneration (CBD), and argyrophilic grain disease (AGD) [3, 9]), or mixed 3R/4R-tauopathies (e.g., the NFT predominant senile dementia (NFT-dementia) [38]). In terms of secondary tauopathies, the best-known example is AD,

which is the most common fatal neurodegenerative disease, contributing to about 60-70% of dementia. One of the microscopical neuropathology of AD is the intracellular NFTs which are composed predominantly of tau protein [39-42]. However, AD is also characterized by the extracellular deposition of amyloid plaques, and genetic studies showed AB to have initial or primary alterations in amyloid metabolism [43]. Biochemical evidence consistently points to A β as the primary driving force of the disease [44]. As a result, the deposition of A β has been regarded widely as the initial pathological event of neurodegenerative processing in AD, which leads to senile plaques (SPs) and NFT formation, neuronal dysfunction, and finally clinical syndromes like cognitive decline or movement disorders [26].

Besides, tauopathies can be categorized by other neuropathological phenotypes, such as the relative amounts of tau inclusions, the presence of varying cell types, and the involvement of distinct neuroanatomical areas [10, 11].

2.1.3 Neuropathology of AD, PSP, and CBD

AD, as outlined above, accounts for the most prevalence of tauopathies. It is marked by predominantly PHF of tau, which contains all six isoforms and has an approximately equal 3R to 4R ratio in the microtubule-binding domain, mixed with straight filaments [8, 45-47]. However, tau accumulation in AD differs in distinguishable spatial and temporal phases (Braak stages) [40, 48]. For instance, by performing immunohistochemistry with 3R and 4R tau specific monoclonal antibodies, evidence showed that the extracellular tangles are disproportionally 3R tau immunoreactive in the medial temporal lobe [13].

In contrast, PSP and CBD tau aggregation form straight filaments of tau, which are located mainly in subcortical nuclei and primarily composed of the 4R tau isoform [8, 49-53]. Although they share similar tauopathy, anatomically PSP demonstrates denser NFTs and neuropil threads mainly in the basal ganglia, cerebellum, and brainstem, without much influence on the neocortex [54]. As for CBD, the pathology largely overlaps with PSP but tended to affect a higher proportion of the cortex and also the subcortical

white matter [7, 55]. Furthermore, CBD and PSP also vary in astroglial tau pathology: PSP is characterized by astrocytic tufts, while CBD comprises astrocytic plaques [11].

The clinical presentation of a corticobasal syndrome (CBS) can have different underlying neuropathological correlates. Here, the majority of A β -negative cases with a clinical phenotype of CBS (~50%) obtained the neuropathological diagnosis of a 4R-positive CBD in autopsy, but 25% are characterized by AD neuropathology and 25% are non-tauopathies [56].

2.1.4 Positron Emission Tomography imaging for tauopathies

Positron Emission Tomography (PET) technology demonstrates its increasing importance in imaging patients with neurodegenerative disorders. ^{18}F -fluorodeoxyglucose (^{18}F FDG), a glucose analog, is uptake in the brain where it gets phosphorylated without the possibility of further metabolization. Thus the phosphorylated ^{18}F FDG is trapped in the cells and emits its radiation at the place of its uptake. Hence, PET imaging with ^{18}F FDG has been used extensively to visualize regional glucose metabolism alterations in neurodegenerative disorders. In tauopathies, ^{18}F FDG-PET imaging enables the evaluation of synaptic dysfunction and neuronal injury which is accompanied by hypometabolism.

Apart from ^{18}F FDG-PET, the continuous development of novel radiotracers facilitated the direct detection of aggregated proteins in various neurodegenerative disorders in recent years. For instance, by accurately identifying A β deposits, amyloid-PET facilitated the early diagnosis for AD. Tau-PET imaging allowed in vivo imaging of the presence and spatial extent of brain tau deposition in addition to clinical assessments, facilitating characterization and quantification of tau in the human brain. However, the detection of tau in the brain is more difficult when comparing to that of A β , because of the generally lower amount of tau deposition when compared to A β , while the existence of various tau isoforms makes the detection even complicated [57]. Tau-specific PET radiotracers for non-invasive detection of tau inclusions in the brain have been developed in recent years

[58, 59], which facilitates earlier diagnosis of tauopathies with higher accuracy, as well as in disease progression tracking and therapeutic efficacy assessment [25].

Besides, some A β - and tau-tracers have also indicated their potential as surrogate markers of neuronal injury, which is included in the A/T/N classification scheme of AD diagnosis [60]. Preliminary data showed that the perfusion-phase images deriving from PET with these tracers are comparable to [^{18}F]FDG imaging [61-68]. Such characteristic suggests a potential to get two biomarkers with a one-stop-shop, allowing to reduce examination cost and radiation exposure, which holds great promise in its future application.

2.2 The first-generation tau-PET radiotracers

To date, the first-generation tau-PET radiotracers include benzothiazole derivatives [^{11}C]PBB3, THK compounds [^{18}F]THK5105, [^{18}F]THK5117, [^{18}F]THK5317, and [^{18}F]THK5351, and [^{18}F]AV1451 ([^{18}F]flortaucipir, T807). These first-generation tau-PET radiotracers have been widely tested for NFT deposition imaging in vitro and in vivo [25, 69-72]. Autoradiography showed specific binding of the radiotracers mentioned above to both intracellular and extracellular neurofibrillary tangles [73-76]. Furthermore, these first-generation tau-radiotracers provided topographic distribution and quantitative estimates of tau pathology closely matching the known patterns in autopsy, both in AD and non-AD tauopathies [73, 77-81].

2.2.1 Clinical application in Alzheimer's disease

Non-invasive imaging of [^{18}F]THK5105 PET demonstrated significantly higher retention in cortical areas which are known to have more PHF-tau in AD brains, with marked tracer retention in the inferior temporal cortex [82]. Besides, this study also observed a significant correlation of [^{18}F]THK5105 retention with clinical severity of dementia or neuronal loss. In a clinical PET study of [^{18}F]THK5117, Harada et al. revealed a higher tracer binding in the temporal lobe in AD subjects when compared to healthy elderly subjects [74]. As shown in a longitudinal PET study, the changes of regional [^{18}F]THK5117 binding

correlated well with cognitive decline in AD patients, suggesting an attribution of cognitive decline to the progression of neurofibrillary pathology [83].

However, these THK compounds exhibited non-negligible retention in the subcortical white matter. To reduce nonspecific tracer retention in the white matter, Harada and colleagues at Tohoku University in Japan developed a novel tau-PET tracer, [^{18}F]THK5351. The first human PET study exhibited more favorable pharmacokinetics with a faster clearance and a sequent lower retention in the subcortical white matter [73].

Of the first-generation tau radiotracers, [^{18}F]AV1451 is the most widely studied one to date. Binding affinities of [^{18}F]AV1451 to NFTs in AD have been investigated in vivo and in vitro since the first human brain imaging publication in 2013 [84].

Evidence showed that [^{18}F]AV1451 has a higher binding affinity to the 3R- and 4R-tau isoforms in PHF and a higher binding selectivity for tau than A β in AD brains [75, 84-86]. On a group level, tau-PET imaging with [^{18}F]AV1451 demonstrated its clinical usefulness for discriminating AD from non-AD neurodegenerative diseases and cognitively normal individuals. Recent clinical PET studies have shown that comparing to cognitively normal individuals, patients with clinically diagnosed AD dementia and mild cognitive impairment (MCI) showed markedly higher levels of [^{18}F]AV1451 retention in brain regions that are susceptible to contain an elevated burden of PHF-tau lesions, especially in the hippocampus, parietal lobe, as well as mesial and lateral temporal lobes [77, 78, 87-92]. Furthermore, the off-target binding of [^{18}F]AV1451 is lower than [^{18}F]THK5351 when it comes to the thalamus, basal ganglia, and white matter [93].

Additionally, autoradiographic binding patterns of [^{18}F]AV1451 were found to be consistent with the predicted topographic Braak staging of NFTs in postmortem AD brains [94]. Furthermore, evidence from in vivo studies demonstrated a significant correlation between [^{18}F]AV1451 retention and AD disease severity, supported by increasing neocortical tracer binding from A β + cognitively normal aged cases to MCI, and more advanced AD dementia [91].

Also, the association of the tau-PET signal to cognitive performance was investigated. Unlike the A β -PET tracer signal which is over the whole cortex, [^{18}F]AV1451 uptake is limited to brain regions being associated with corresponding clinical symptoms and areas with hypometabolism [95, 96]. This is consistent with some neuropathological studies of [^{18}F]AV1451 reporting the correlation between location and quantification of tracer binding and clinical symptoms and the degree of cognitive impairment [97-102], whereas the association between A β -PET and cognition is generally weaker and less region-specific [96, 103]. The body of evidence for excellent performance of [^{18}F]AV1451 in imaging of AD led to its FDA approval in 2020.

2.2.2 Clinical application in non-AD tauopathies

So far, most studies about tau-PET focused on AD patients, with the primary emphasis on detecting of PHFs in the AD brain. Meanwhile, radiotracers have been shown to bind to 4R tau in relatively rare neurodegenerative disorders including PSP and CBS.

For example, in clinically diagnosed PSP patients, significantly higher [^{18}F]THK5351 retention was observed in the midbrain and the globus pallidus [80, 104, 105]. Quantitative analysis indicated strong discriminations of clinically diagnosed PSP patients from healthy controls (HCs) and Parkinson's disease (PD) patients based on bilateral elevated [^{18}F]AV1451 retention in the globus pallidus, the subthalamic nucleus, the putamen, the midbrain, and the dentate nucleus [106-109]. These clinical findings suggest a binding affinity of [^{18}F]THK5351 and [^{18}F]AV1451 to the 4R tau aggregation in PSP. Furthermore, some of the abovementioned studies also observed a correlation of regional tracer uptake with the PSP rating scale (PSPRS) indicated disease severity [80, 108].

In patients with CBS, asymmetric and significantly higher accumulation of [^{18}F]THK5351 was seen in the frontal, parietal, and globus pallidus than in normal controls and AD patients [110]. Similarly, compared to controls, tau-PET with [^{18}F]AV1451 in CBS patients

also exhibited increased binding in the motor-related subcortex or cortex, the corticospinal tract, and the symptom-contralateral thalamus [111, 112]. Besides, previous longitudinal tau imaging observations demonstrated that the tracer binding increases during disease advancement in CBS patients [113, 114]. Furthermore, in an autopsy-diagnosed CBD patient, the regional [^{18}F]AV1451 tau-PET uptake correlated with 4R-tau burden assessed by histopathological assay, indicating a high affinity of [^{18}F]AV1451 to 4R-tau deposits in CBD [115]. Some other postmortem studies for [^{18}F]THK5351 and [^{18}F]AV1451 also confirmed the in vivo binding in CBD patients [110, 111, 114, 116].

2.2.3 Limitations and challenges

Although many breakthroughs have been achieved in the diagnosis of tauopathies using the first-generation tau-PET radiotracers, a certain amount of the signal from the first-generation tau-PET tracers was proven to be off-target binding. For instance, beside binding to tau, both [^{18}F]THK5351 and [^{18}F]AV1451 were reported to show affinity to the monoamine oxidases (MAO) A or B -- [^{18}F]AV1451 was found to bind to MAO-A with a similar affinity when compared to its affinity to tau fibrils [117, 118] while the high binding affinity of [^{18}F]THK5351, especially in the thalamus, was attributed to MAO-B [119-121]. Furthermore, several studies found a decreased in vivo uptake of [^{18}F]THK5351 upon MAO-B inhibitor treatment [121, 122].

Besides, [^{11}C]PBB3 and [^{18}F]AV1451 were reported to bind to vascular structures (choroid plexus for both, and dural venous sinuses for [^{11}C]PBB3) [123, 124]. These findings weaken the clinical validity of the above tau tracers, especially in detecting tau aggregations in deeper brain regions or the limbic cortex. Furthermore, off-target binding to neuromelanin has been described for all mentioned tau tracers, especially for [^{18}F]AV1451 [75, 94, 124]. This can affect image assessment and quantification especially in the mid-brain (substantia nigra) with a physiologically high concentration of neuromelanin [125]. Furthermore, age-related increases of [^{18}F]AV1451 binding have been found in the basal

ganglia of aged patients independent with clinical diagnosis. This finding was associated with the accumulation of iron in these areas [85, 87, 126-128].

As a lot of regions of interest (ROIs) in both PSP and CBS overlap with the off-target binding areas, it suggests off-target binding possibly be responsible at least partially for the in vivo retention. Off-target binding of tau-PET tracers obscures visual interpretation of tau-PET images and complicates the diagnoses and differentiation from other diseases, and is therefore one of the major challenges and limitations in the development of novel tau radiotracers.

On the other hand, these first-generation tracers bind mostly to AD-typical 3/4R tau isoforms of PHFs compared to other isoforms and filaments. Binding to different tau isoforms and folds would allow tau-PET tracers to detect various tauopathies [129]. Thus, the development of new radiotracers with more sensitivity and, more importantly, specificity for other tau isoforms would contribute to a better diagnosis and understanding of tauopathies. For example, Rosler et al. suggested to develop novel tau tracers more specific for 4R-tau, which would allow the discrimination of 4R-tauopathies from HCs and non-tauopathies, as well as offer early inter-tauopathies discrimination at a single-patient level [11].

2.3 [¹⁸F]PI-2620, a second-generation tau-PET radiotracer

These abovementioned factors made the clinical application of first-generation tau-PET tracers challenging, which accelerated the continuous development of second-generation tau-PET tracers. The primary aims in the development of second-generation tau-PET tracers were to minimize off-target binding and therefore improve the binding specificity. Based on the efforts of several academic and commercial groups, several second-generation tau-PET tracers, such as [¹⁸F]RO6958948 (RO-948), [¹⁸F]MK-6240, [¹⁸F]GTP-1, and [¹⁸F]PI-2620 emerged. Chemical structures of the several widely-investigated tracers for tau-PET are shown in **Figure 2**. The in vitro autoradiography and first-

in-human studies of most of the abovementioned second-generation tracers demonstrated a high binding affinity to NFTs in AD, with absent and significantly lower off-target binding to A β and MAO-A/B [130-133]. Among the second-generation tracers, [^{18}F]PI-2620, showed especially promising results in preclinical experiments and first-in-human studies in tauopathies.

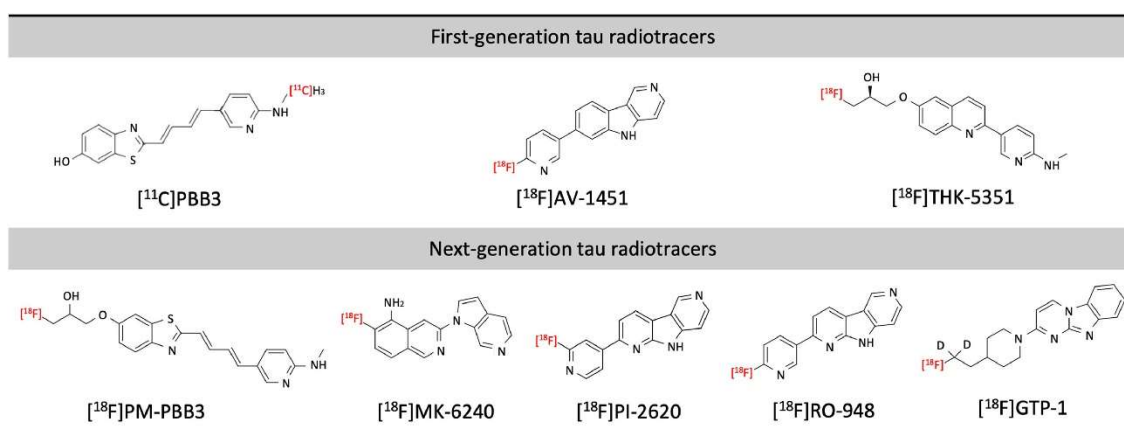


Figure 2. Chemical structures of several widely-investigated tracers for tau-PET (From Beyer and Brendel, Semin Nucl Med 2020 [134]).

2.3.1 Preclinical study of [^{18}F]PI-2620

A series of compounds were tested in a preclinical study to select a leading candidate for clinical validation [130]. Taken all the in vitro and in vivo results together, [^{18}F]PI-2620 (compound 7), which is structurally similar to FTP, was finally chosen for further clinical evaluations with superior properties.

To evaluate the binding properties of [^{18}F]PI-2620 to pathological tau aggregates, self-competition experiments using isolated PHFs, K18 fibrils (depicting 4R pathology), and brain homogenates of AD, PSP, and PiD subjects were performed. The result displayed superior binding properties to not only both 3R and 4R tau, but also to various tau aggregate folds in both AD and non-AD tauopathies. Besides the above mentioned binding

assays, selective binding of [^{18}F]PI-2620 to pathological tau was confirmed on AD and PSP brain sections. Furthermore, observations of the very low background binding on the non-demented control (NDC) brain section without pathological tau verified its high binding specificity. Overall, [^{18}F]PI-2620 displayed a high selectivity for tau without relevant off-target binding to A β or MAO-A and -B .

2.3.2 Clinical application of [^{18}F]PI-2620

To confirm the suitability of [^{18}F]PI-2620 for detecting pathological tau aggregates, several clinical studies of [^{18}F]PI-2620 are currently ongoing worldwide.

The first-in-human [^{18}F]PI-2620 PET studies in AD subjects showed significantly higher tracer uptake in temporal and parietal lobes, precuneus, and posterior cingulate cortex, and fast washout from non-target regions when compared to NDC [135-138]. Besides, Mueller et al. also observed a strong correlation of [^{18}F]PI-2620 uptake in neocortical regions with the severity of cognitive disablement [135]. Another human study of [^{18}F]PI-2620 PET indicated fast tracer kinetics with a tolerable effective dose and low test-retest variability [139].

These studies confirmed that [^{18}F]PI-2620 is a promising noninvasive tool to image tau deposition in AD. However, previous studies applied various acquisition protocol in clinical practice of [^{18}F]PI-2620 PET. In both Muller et al. 's and Bullich et al.'s studies [135, 139], time-standardized-uptake-value-ratio (time-SUVR) curves reached a plateau at around 40 min post-injection (p.i.) for most subjects whereas SUVR continued to increase during the whole scan in some AD subjects, and static PET scans between 45 and 75 min robustly discriminated AD subjects from HCs. Other studies of [^{18}F]PI-2620 PET proposed equilibrium time at 60 to 90 min p.i. [140] and 80 to 90 min p.i. [138].

To study the potential of [^{18}F]PI-2620 as a biomarker in clinically diagnosed PSP patients, our group performed the first large-scale multicenter observational study [141]. Postmor-

tem autoradiography assay demonstrated the [^{18}F]-PI-2620 binding in the unblocked basal ganglia and the frontal cortex of PSP Richardson syndrome (PSP-RS, classic subtype of PSP) patients to colocalized with AT8 positive tau aggregation. As for in vivo binding, significant difference was observed between the PSP group and the control groups in PSP target regions, especially in the basal ganglia. Semiquantitative analyses and visual read yielded high sensitivity (85% and 80%) and specificity (77% and 83%) for detection of PSP-RS individuals, which further demonstrated the potential of [^{18}F]-PI-2620 for a more reliable diagnosis of PSP at the single-patient level.

Exemplary cases of [^{18}F]PI-2620 PET images in AD and non-AD tauopathies are illustrated in **Figure 3**.

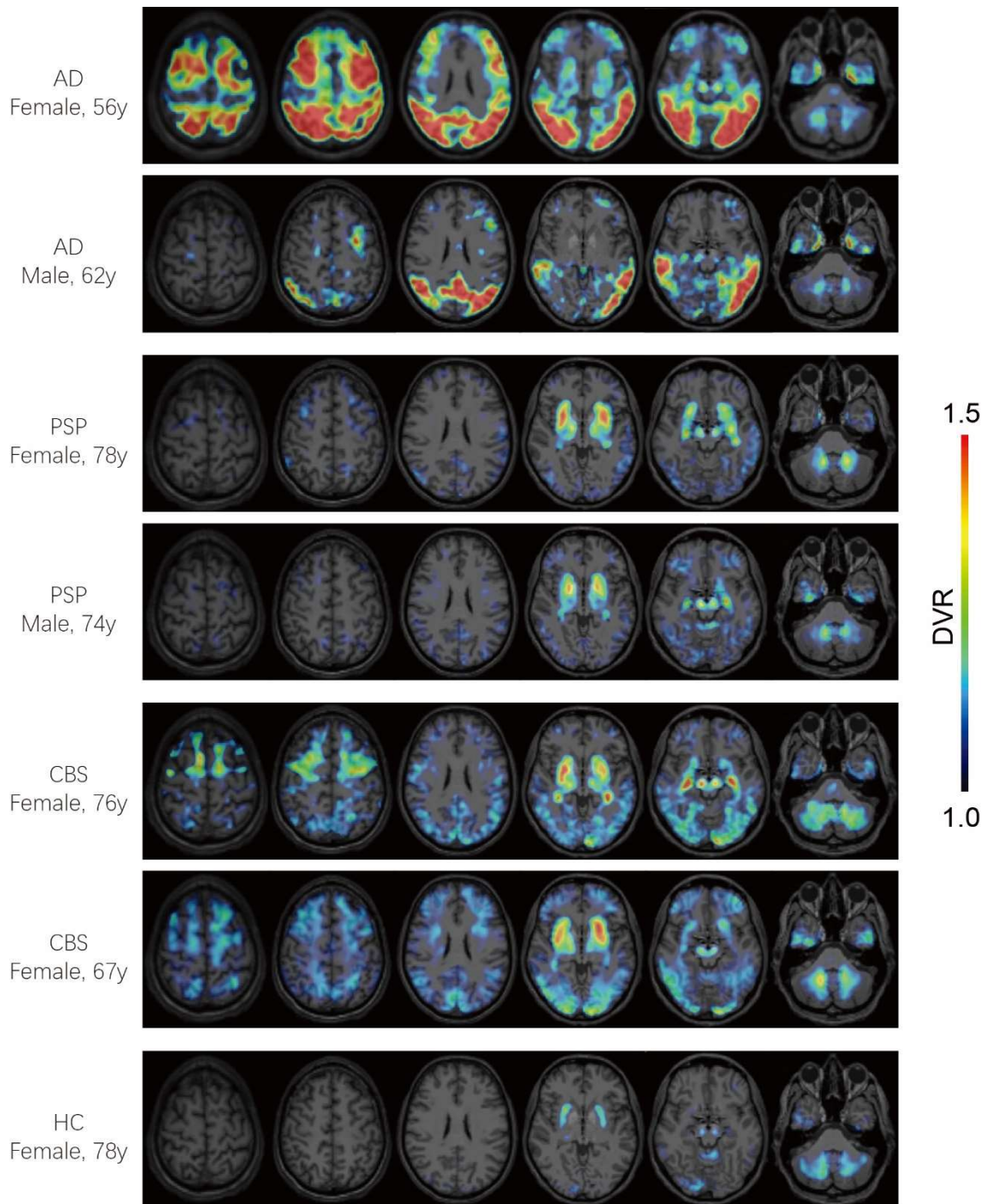


Figure 3. Exemplary axial [^{18}F]PI-2620 PET images of patients with AD and non-AD tauopathies (PSP and CBS). AD, Alzheimer's disease; PSP, progressive supranuclear palsy; CBS, corticobasal syndrome; HC, healthy control; DVR, distribution volume ratio.

3. Summary (English)

The aim of this doctoral thesis was to study the application of the novel tau radiotracer [^{18}F]PI-2620 in clinically diagnosed neurodegenerative diseases. During the research period, we investigated whether the detailed binding characteristics of [^{18}F]PI-2620 by PET are able to distinguish the clinically predicted tau isoform in different tauopathies. Furthermore, we assessed the potential of early-phase of [^{18}F]PI-2620 tau-PET imaging for neuronal injury diagnosis.

To address if [^{18}F]PI-2620 binding characteristics are able to distinguish different tau isoforms in a variety of tauopathies, kinetic modeling parameters and binding magnitude of 3/4R tauopathy (AD) and 4R tauopathy (PSP, CBS) were calculated and compared. We found that cortical [^{18}F]PI-2620-positive regions of 4R-tau cases showed higher delivery, higher efflux, and lower retention when compared to the 3/4R-tau group. Furthermore, we established a model using different kinetic and binding characteristics to discriminate 3/4R tauopathies from 4R tauopathies, which shows a stronger prediction of a 3/4R tauopathy when compared to the pure binding magnitude.

Besides, to study the early-phase of [^{18}F]PI-2620 tau-PET imaging for neuronal injury diagnosis, dynamic [^{18}F]PI-2620 tau-PET (0–60 min p.i.) and static [^{18}F]FDG PET (30–50 min p.i.) were performed in 26 subjects with neurodegenerative disorders. Semiquantitative and visual analyses of [^{18}F]PI-2620 PET were correlated with that of [^{18}F]FDG PET using two normalization approaches (scaling by the global mean and cerebellar normalization). By VOI-based comparison, we found 0.5-2.5 min p.i. to be an optimal time window for [^{18}F]PI-2620 PET early-phase imaging. Furthermore, early-phase [^{18}F]PI-2620 PET approaches were observed to strongly correlate with [^{18}F]FDG PET in all cortical target regions, especially when it came to global mean normalization. Furthermore, the visual assessment revealed that the regional pattern of hypoperfusion of early-phase [^{18}F]PI-2620 PET to be consistent with the hypometabolism pattern of [^{18}F]FDG PET, indicating moderate to high regional agreements between them.

In conclusion, the research work of this doctoral thesis revealed that [¹⁸F]PI-2620 PET is able to distinguish the clinically predicted 3/4R- from 4R-tauopathies. Furthermore, the established early-phase perfusion imaging can serve as a surrogate biomarker of neuronal injury. These findings demonstrate a promising perspective of [¹⁸F]PI-2620 as a novel second-generation tau-PET tracer, likely facilitating to contribute to a better understanding of tauopathies.

4. Zusammenfassung (Deutsch)

Ziel dieser Promotionsarbeit war die Anwendung des neuen Positronen Emissions Tomographie (PET) Tau-Radiotracers [^{18}F]PI-2620 bei klinisch diagnostizierten neurodegenerativen Erkrankungen zu untersuchen. Es wurde untersucht, ob sich die Bindungseigenschaften von [^{18}F]PI-2620 für klinisch vorhergesagte Tau-Isoformen bei verschiedenen Tauopathien unterscheiden. Zudem wurde das Potenzial der Frühphase der [^{18}F]PI-2620 Tau-PET Bildgebung für die Erfassung des neuronalen Schaden evaluiert.

Um festzustellen, ob [^{18}F]PI-2620 in der Lage ist, verschiedene Tau-Isoformen in einer Vielzahl von Tauopathien zu unterscheiden, wurden kinetische Modellierungsparameter und die Bindungsgröße von 3/4R-Tauopathien (AD) und 4R-Tauopathien (CBS, PSP) berechnet und verglichen. Wir fanden heraus, dass kortikale [^{18}F]PI-2620-positive Regionen von 4R-Tau-Fällen im Vergleich zur 3/4R-Tau-Gruppe durch eine höhere Ablösung des Tracers von der Zielstruktur gekennzeichnet waren. Weiterhin zeigte sich für die 4R-Tau-Gruppe eine höhere Anflutung und eine geringere Retention. Darüber wurde ein Modell erstellt, welches die unterschiedlichen Bindungseigenschaften verwendete, um 3/4R-Tauopathie von 4R-Tauopathie zu unterscheiden. Hier zeigte sich eine stärkere Vorhersage einer 3/4R-Tauopathie für die Gesamtheit der Parameter im Vergleich zur alleinigen Betrachtung der Bindungsgröße.

Um die Frühphase der [^{18}F]PI-2620 Tau-PET Bildgebung für die Erfassung des neuronalen Schadens zu untersuchen, wurden dynamische [^{18}F]PI-2620 Tau-PET (0–60 min p.i.) und statische [^{18}F]FDG-PET (30–50 min p.i.) Messungen jeweils bei 26 Patienten mit neurodegenerativer Erkrankung durchgeführt. Semiquantitative und visuelle Analysen der [^{18}F]PI-2620 Tau-PET wurden mit denen von [^{18}F]FDG-PET unter Verwendung von zwei Normalisierungsansätzen (globaler Mittelwert und Kleinhirnnormalisierung) korreliert. Durch einen regionen-basierten Vergleich fanden wir heraus, dass 0,5-2,5 min p.i. ein optimales Zeitfenster für die [^{18}F]PI-2620-PET

Frühphasenbildgebung zu sein scheint. Darüber hinaus wurde festgestellt, dass die Quantifizierung der [^{18}F]PI-2620-PET Frühphase in allen kortikalen Zielregionen stark mit der Quantifizierung der [^{18}F]FDG-PET korrelierte, insbesondere bei Normalisierung mittels dem globalen Mittelwerts geht. Die visuelle Bewertung ergab, dass das regionale Bild der Hypoperfusion in der [^{18}F]PI-2620-PET Frühphase dem Hypometabolismus Muster in der [^{18}F]FDG-PET ähnelte. Hier zeigte sich eine moderate bis hohe regionale Korrelation zwischen den beiden Modalitäten.

Zusammenfassend kann die [^{18}F]PI-2620-PET die klinisch vorhergesagten 3/4R- und 4R-Tauopathien unterscheiden und die Anwendung der Frühphasenbildgebung kann als Ersatzbiomarker für die Detektion des neuronalen Schadens verwendet werden. Diese Ergebnisse zeigten eine vielversprechende Perspektive von [^{18}F]PI-2620, einem neuen Tau-PET-Tracer der zweiten Generation, um zu einem besseren Verständnis von Tauopathien beizutragen.

5. Paper I

Original Article

JCBFM

Binding characteristics of [¹⁸F]PI-2620 distinguish the clinically predicted tau isoform in different tauopathies by PET

Journal of Cerebral Blood Flow & Metabolism
2021, Vol. 41(11) 2957–2972
© The Author(s) 2021



Article reuse guidelines:
sagepub.com/journals-permissions
DOI: 10.1177/0271678X211018904
journals.sagepub.com/home/jcbfm



Mengmeng Song¹, Leonie Beyer¹, Lena Kaiser¹,
Henryk Barthel², Thilo van Eimeren^{3,4,5,6}, Ken Marek^{7,8},
Alexander Nitschmann¹, Maximilian Scheifele¹, Carla Palleis⁹,
Gesine Respondek¹⁰, Maïke Kern¹, Gloria Biechele¹,
Jochen Hammes⁴, Gérard Bischof⁴, Michael Barbe⁵,
Özgür Onur⁵, Frank Jessen^{6,11,12}, Dorothee Saur¹³,
Matthias L Schroeter^{14,15,16,17}, Jost-Julian Rumpf¹³,
Michael Rullmann², Andreas Schildan², Marianne Patt²,
Bernd Neumaier^{3,4}, Olivier Barret^{7,8,18}, Jennifer Madonia^{7,8},
David S Russell^{7,8}, Andrew W Stephens¹⁹, Andre Mueller¹⁹,
Sigrun Roeber²⁰, Jochen Herms^{6,20}, Kai Bötzel⁹,
Adrian Danek⁹, Johannes Levin^{9,21,22}, Joseph Classen¹³,
Günter U Höglinger^{10,21,23}, Peter Bartenstein^{1,22},
Victor Villemagne^{24,25,26}, Alexander Drzezga^{4,6}, John Seibyl^{7,8},
Osama Sabri², Guido Boening¹, Sibylle Ziegler¹ and
Matthias Brendel^{1,22}

¹Department of Nuclear Medicine, University Hospital of Munich, LMU Munich, Munich, Germany

²Department of Nuclear Medicine, University of Leipzig, Leipzig, Germany

³Cognitive Neuroscience, Institute for Neuroscience and Medicine (INM-3), Research Centre Juelich, Juelich, Germany

⁴Department of Nuclear Medicine, University Hospital Cologne, Cologne, Germany

⁵Department of Neurology, University Hospital Cologne, Cologne, Germany

⁶German Center for Neurodegenerative Diseases (DZNE), Bonn, Germany

⁷InviCRO, LLC, Boston, MA, USA

⁸Molecular Neuroimaging, A Division of InviCRO, New Haven, CT, USA

⁹Department of Neurology, University Hospital of Munich, LMU Munich, Munich, Germany

¹⁰Department of Neurology, Medizinische Hochschule Hannover, Hannover, Germany

¹¹Department of Psychiatry, University Hospital Cologne, Cologne, Germany

¹²Center for Memory Disorders, University Hospital Cologne, Cologne, Germany

¹³Department of Neurology, University of Leipzig, Leipzig, Germany

¹⁴Clinic for Cognitive Neurology, University of Leipzig, Leipzig, Germany

¹⁵LIFE – Leipzig Research Center for Civilization Diseases, University of Leipzig, Leipzig, Germany

¹⁶Max-Planck-Institute of Human Cognitive and Brain Sciences, Leipzig, Germany

¹⁷FTLD Consortium Germany, Ulm, Germany

¹⁸Laboratoire des Maladies Neurodégénératives, Université Paris-Saclay, CEA, CNRS, MIRCen, Fontenay-aux-Roses, France

¹⁹Life Molecular Imaging GmbH, Berlin, Germany

²⁰Center for Neuropathology and Prion Research, University Hospital of Munich, LMU Munich, Munich, Germany

²¹German Center for Neurodegenerative Diseases (DZNE), Munich, Germany

²²Munich Cluster for Systems Neurology (SyNergy), Munich, Germany

²³Department of Neurology, Technical University Munich, Munich, Germany

²⁴Department of Molecular Imaging & Therapy, Austin Health, Heidelberg, VIC, Australia

²⁵The Florey Institute of Neuroscience and Mental Health, The University of Melbourne, Melbourne, VIC, Australia

²⁶Department of Medicine, Austin Health, The University of Melbourne, Melbourne, VIC, Australia

Corresponding author:

Matthias Brendel, Department of Nuclear Medicine, University of Munich, Marchioninstraße 15, Munich 81377, Germany.
Email: matthias.brendel@med.uni-muenchen.de

Abstract

The novel tau-PET tracer [^{18}F]PI-2620 detects the 3/4-repeat-(R)-tauopathy Alzheimer's disease (AD) and the 4R-tauopathies corticobasal syndrome (CBS) and progressive supranuclear palsy (PSP). We determined whether [^{18}F]PI-2620 binding characteristics deriving from non-invasive reference tissue modelling differentiate 3/4R- and 4R-tauopathies. Ten patients with a 3/4R tauopathy (AD continuum) and 29 patients with a 4R tauopathy (CBS, PSP) were evaluated. [^{18}F]PI-2620 PET scans were acquired 0-60 min p.i. and the distribution volume ratio (DVR) was calculated. [^{18}F]PI-2620-positive clusters ($\text{DVR} \geq 2.5 \text{ SD}$ vs. 11 healthy controls) were evaluated by non-invasive kinetic modelling. R_1 (delivery), k_2 & k_{2a} (efflux), DVR, 30-60 min standardized-uptake-value-ratios (SUVR_{30-60}) and the linear slope of post-perfusion phase SUVR (9-60 min p.i.) were compared between 3/4R- and 4R-tauopathies. Cortical clusters of 4R-tau cases indicated higher delivery ($R_{1\text{SRTM}}$: 0.92 ± 0.21 vs. 0.83 ± 0.10 , $p = 0.0007$), higher efflux ($k_{2\text{SRTM}}$: $0.17/\text{min} \pm 0.21/\text{min}$ vs. $0.06/\text{min} \pm 0.07/\text{min}$, $p < 0.0001$), lower DVR (1.1 ± 0.1 vs. 1.4 ± 0.2 , $p < 0.0001$), lower SUVR_{30-60} (1.3 ± 0.2 vs. 1.8 ± 0.3 , $p < 0.0001$) and flatter slopes of the post-perfusion phase (slope_{9-60} : $0.006/\text{min} \pm 0.007/\text{min}$ vs. $0.016/\text{min} \pm 0.008/\text{min}$, $p < 0.0001$) when compared to 3/4R-tau cases. [^{18}F]PI-2620 binding characteristics in cortical regions differentiate 3/4R- and 4R-tauopathies. Higher tracer clearance indicates less stable binding in 4R tauopathies when compared to 3/4R-tauopathies.

Keywords

Tau, PI-2620, binding, affinity, kinetic modelling

Received 13 August 2020; Revised 31 January 2021; Accepted 3 February 2021

Introduction

Accumulation of hyperphosphorylated microtubule-associated tau protein (MAPT, tau) in neurons and glia is a hallmark of a wide range of neurodegenerative diseases.¹ Disorders associated with the accumulation of MAPT are thus termed tauopathies, which include Alzheimer's disease (AD) as well as progressive supranuclear palsy (PSP), corticobasal degeneration (CBD), and Pick's disease (PiD) among the non-AD tauopathies. Accumulation of tau protein is closely associated with neurodegeneration and cognitive impairment.^{2,3}

The neuropathology of different tauopathies exhibits its varying isoform composition of their filaments as well as distinct neuroanatomical distribution and relative amounts of tau inclusions.⁴ Six molecular isoforms of tau are generated by alternative pre-mRNA splicing of a single gene transcript and classified according to the number of repeats of the microtubule binding domains as 3-repeat (3R) and 4-repeat (4R) tau proteins.^{5,6} Equal amounts of 3R and 4R tau isoforms exist in the normal brain. In tauopathies, tau is abnormally hyperphosphorylated and accumulates intracellularly, forming tangles of paired helical filaments (PHF), twisted ribbons and/or straight filaments.

AD accounts for the majority of tauopathy cases and is marked by predominantly PHF of tau with an approximately equal 3R to 4R ratio in the microtubule-binding domain, mixed with straight filaments.⁷⁻⁹ In contrast, PSP and CBD tau aggregation forms straight

filaments of tau, which are primarily composed of the 4R isoform.^{5,7,10-13}

Positron emission tomography (PET) emerged for non-invasive detection of tau inclusions in the brain during the recent years.^{14,15} Tau-PET tracers allow imaging of the presence and spatial extent of brain tau deposition, facilitating characterization and quantification in humans. First generation tau-radiotracers have already provided topographic distribution and quantitative estimates of tau pathology in AD and non-AD tauopathies closely matching the known patterns in autopsy.¹⁶⁻²¹ However, relevant amounts of the signal of first generation tau-PET ligands prove to be non-specific^{22,23} which accelerated the development of next-generation tau PET ligands with reduced off-target binding.^{14,24-27}

For tau-PET tracers, binding to both 3R and 4R tau isoforms and different tau-folds would allow the detection of various tauopathies.²⁸ In vitro pharmacological studies and autoradiography of the novel second generation tau-PET tracer [^{18}F]PI-2620 demonstrated its potential to bind to both 3R and 4R aggregated tau isoforms as well as to different tau aggregate folds in AD and non-AD tauopathies using AD and PSP brain sections as well as brain homogenates of PSP and PiD patients.²⁵ First in human results suggest that [^{18}F]PI-2620 is able to visualize the predominantly 3/4R-tauopathy AD^{29,30} and the mainly 4R-tauopathies corticobasal syndrome (CBS)³¹ and PSP³² by PET, but likely with a different magnitude of affinity

among them (pIC_{50} 8.5 ± 0.1 for AD brain tissue versus pIC_{50} 7.7 ± 0.1 for PSP brain tissue).²⁵ The majority of A β -negative cases with a clinical phenotype of CBS obtained the neuropathological diagnosis of a 4R-positive CBD in autopsy.³³ The lower binding affinity of [¹⁸F]PI-2620 to 4R tau *in vitro* could cause faster clearance from the target when compared to 3/4R tau *in vivo*. Although 3/4R and 4R tauopathies have obvious topographical differences in the majority of cases, a regional overlap exists among them. For instance, patients with AD-CBS (predominant 3/4R) and 4R-CBS (predominant 4R) are characterized by involvement of the motor cortex and patients with typical AD (predominant 3/4R) and argyrophilic grain disease (predominant 4R) comprise tau accumulation in parietal-temporal cortices.³⁴ Thus, detection of differences in [¹⁸F]PI-2620 binding characteristics among different tau isoforms would potentially facilitate a more reliable differential diagnosis.

The aim of this study was to determine whether, [¹⁸F]PI-2620-positive cortical and subcortical clusters have different binding characteristics as assessed by non-invasive reference tissue modelling. Finally, we performed a receiver operating curve analysis to determine if clinically diagnosed 3/4R and 4R tauopathies can be differentiated by the tracer kinetics and binding characteristics of [¹⁸F]PI-2620.

Material and methods

Cohort and study design

The subjects were either recruited and scanned at the Ludwig-Maximilians-University of Munich (LMU), Department of Nuclear Medicine or took part at the first in human study of [¹⁸F]PI-2620 at Invivo (New Haven, U.S.A.) between December 2016 and September 2020. Patients were diagnosed to belong to the AD continuum (total $n = 10$: mild cognitive impairment (MCI), $n = 5$; dementia due to AD, $n = 5$) as 3/4R tauopathy or PSP ($n = 15$)/CBS ($n = 14$) as 4R tauopathies according to current diagnostic criteria.^{35–38} In particular, the AD continuum patients were required to meet criteria for typical AD with MCI or dementia according to the diagnostic criteria of the National Institute on Aging and Alzheimer's Association.³⁹ Diagnosis of 4R-tauopathies was made according to the revised Armstrong Criteria of probable CBS³⁷ or the Movement Disorders Society criteria of possible/probable PSP or possible PSP with predominant CBS.³⁵ Inclusion criteria were age > 45 years at the time of inclusion, and stable pharmacotherapy for at least one week before the PET examination. Exclusion

criteria were severe neurological or psychiatric disorders other than AD-continuum or 4R-tauopathies. Regional quantification in predefined regions of interest in AD continuum and PSP patients as well as in healthy controls (comprising 59% of the current sample) was previously published.³² Healthy controls had no evidence of cognitive impairment following a neuropsychological battery which included the ADAS-Cog, a CDR score of 0, no family history of AD or neurological disease associated with dementia and no objective motor symptoms. PET data analyses were approved by the local institutional review board of the LMU Munich (application numbers 17-569 & 19-022) under consideration of the Helsinki Declaration of 1975 (and as revised in 1983). All participants provided written informed consent prior to the PET scan. The β -amyloid status was obtained by PET ([¹⁸F]florbetaben or [¹⁸F]flutemetamol) or cerebrospinal fluid assessment. β -amyloid-positive clinical PSP/CBS as well as β -amyloid-negative clinical AD cases were excluded from the analysis since the clinically predicted tau isoform would have been uncertain in these cases. To allow comparison of 3/4R and 4R tauopathies in matching brain regions, only visually rated [¹⁸F]PI-2620-positive cases in cortical brain areas were included into the analysis of patients. One expert reader assessed the [¹⁸F]PI-2620 distribution volume ratio (DVR) maps in 3D mode using standardized settings (lower/upper DVR threshold 1.0/1.5; cold color scale, overlay on an MRI standard template in the Montreal Neurology Institute (MNI) space. The reader evaluated binding in the frontal, parietal, temporal and occipital cortex with knowledge of the pattern in healthy controls. The intention of conservative judgement of cortical binding in DVR maps was to avoid inclusion of any artificial clusters. The reader was aware of the clinical diagnosis. Subcortical [¹⁸F]PI-2620-positivity was no prerequisite for inclusion. Figure 1(a) illustrates the selection process.

Acquisition, reconstruction and image harmonization

[¹⁸F]PI-2620 PET imaging was performed in a full dynamic setting (0–60 min p.i.) on different scanners (Munich: Siemens Biograph True point 64 PET/CT & Siemens mCT, Siemens, Erlangen, Germany; New Haven: Siemens ECAT EXACT HR+, Siemens, Erlangen, Germany; Melbourne: Philips Gemini TF 64 PET/CT, Eindhoven, The Netherlands) at three specialized neuroimaging sites using the established standard scan protocol of each center for brain PET imaging. The injected bolus dose was 217 ± 53 MBq (range: 178–334 MBq). Details on all scanners, as well

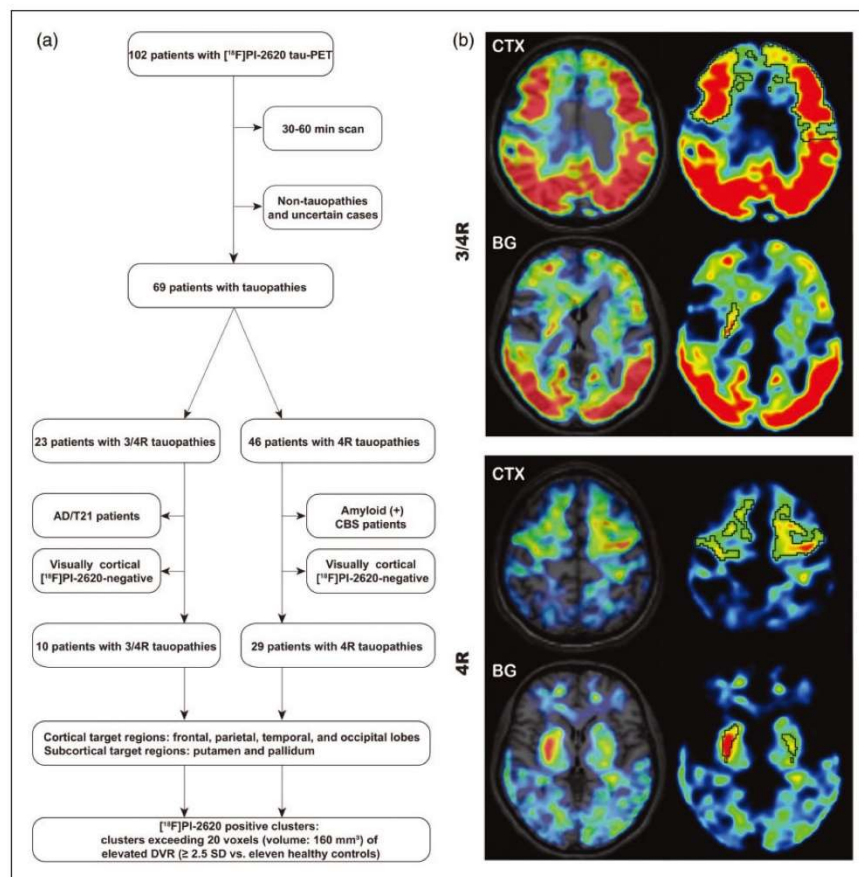


Figure 1. (a) Study flowchart. Only patients with a dynamic scan, clinical confidence on the diagnosis and a cortical [¹⁸F]PI-2620-positive PET scan were included. (b) Examples of cortical (frontal cortex) and subcortical target region definition by z-score maps in patients with clinically diagnosed 3/4R (upper panel) and 4R (lower panel) tauopathies. Clusters above a threshold of mean value + 2.5 standard deviations (black) were defined as [¹⁸F]PI-2620-positive assuming tau-positivity. CTX: cortex; BG: basal ganglia; AD: Alzheimer's disease; CBS: corticobasal syndrome.

as acquisition and reconstruction parameter are provided in the Supplement of our previous study.³² Dynamic emission recordings were framed into 6x30s, 4x60s, 4x120s and 9x300s. Data from Hofmann phantoms were used to obtain scanner specific filter functions which were then consequently used to generate images with a similar resolution (FWHM: 9 × 9 × 10 mm), following the ADNI image harmonization procedure.⁴⁰ All dynamic datasets were visually inspected for motion (~5 mm threshold) and automatically corrected for motion of more than 5 mm using the motion correction tool in PMOD (V3.9 PMOD technologies Basel, Switzerland). In brief, this tool performs coregistration of individual PET frames to each

other to guarantee a precise regional overlap of all frames in a multi-frame dataset.

Image post-processing

[¹⁸F]PI-2620 template generation. An [¹⁸F]PI-2620 PET template was generated independently of this investigation³² to allow inclusion of patients not eligible to an MRI (i.e. pacemaker, metal implants). In brief, 20 randomly chosen datasets of PSP patients, disease controls and healthy controls, which all had a T1w 3D MRI sequence were automatically processed by the PNEURO pipeline²⁰ to obtain [¹⁸F]PI-2620 images in the MNI space. Frames between 30 and 60 minutes p.i. were summed and scaled by the global mean, followed

by averaging all 20 cases to an [^{18}F]PI-2620 template in the MNI space. The template already showed robust performance in cases with high and low [^{18}F]PI-2620 positivity due to the well-defined landmarks of the tracer in the 30–60 minutes p.i. window.³²

Spatial normalization. All 50 dynamic [^{18}F]PI-2620 PET datasets (39 patients and 11 healthy controls) were transformed to the MNI space using the non-linear brain normalization of the summed 30–60 min frames to the established [^{18}F]PI-2620 PET template as described previously.³² In brief, automatized brain normalization settings in PMOD included nonlinear warping, 8 mm input smoothing, equal modality, 16 iterations, frequency cutoff 3, regularization 1.0, and no thresholding. The transformation was saved and applied to the full dynamic [^{18}F]PI-2620 PET datasets to assure a minimum of interpolation.

Quantification. In preparation of the cluster-based analysis by various kinetic models, [^{18}F]PI-2620-positive clusters had to be defined by a standardized approach. Thus, we applied the previously established quantification approach for generation of parametric images.³² The multilinear reference tissue model 2 (MRTM2⁴¹) was used to calculate distribution volume ratios (DVR; $\text{DVR} = \text{BPND} + 1$) images of each full dynamic dataset. The previously evaluated cerebellar reference tissue³² (detailed illustration in Supplemental Figure 1), excluding the dentate nucleus and the central cerebellar white matter as well as the superior and the posterior cerebellar layers ($d = 1.5\text{ cm}$ each), served as a reference region.

Generation of Z-score maps. MRTM2 images of eleven healthy controls were used to calculate average and standard deviation maps of controls. All MRTM2 maps of the 39 patients were processed by the following formula using the PMOD image algebra tool to generate Z-score maps of individual patients:

$$\text{Patient Z score map} = \frac{\left\{ \begin{array}{l} \text{Patient MRTM2 DVR map} \\ - \text{Average HC MRTM2 DVR map} \end{array} \right\}}{\left\{ \begin{array}{l} \text{Standard deviation HC} \\ \text{MRTM2 DVR map} \end{array} \right\}}$$

Data analysis

Definition of cortical and subcortical [^{18}F]PI-2620-positive clusters. The rationales of a cluster-based analysis were robust kinetic modeling in volumes large enough in relation to the resolution of the PET system and evaluation in regions that likely comprise tau in the patient. Thus, we set conservative thresholds for the

cluster size and [^{18}F]PI-2620-positivity. Furthermore, we used predefined brain volumes (defined by lobes and basal ganglia compartments) for anatomical cluster definition. Predefined regions of the Hammers atlas and the atlas of the basal ganglia^{42,43} were used for tissue classification in Z-score maps. We defined frontal, parietal, temporal, and occipital lobes as cortical target regions as well as the putamen and the globus pallidus as subcortical target regions. Within each target region, clusters exceeding 20 voxels (volume: 160 mm^3 , corresponding to a $5.0 \times 5.0 \times 6.4\text{ mm}$ sphere) of elevated DVR ($\geq 2.5\text{ SD}$ vs. eleven healthy controls) were classified as [^{18}F]PI-2620-positive. The strict threshold was used to avoid inclusion of voxels with artificially high values, caused by spillover from compartments adjacent to the brain (i.e. venous sinuses). The cluster volume was recorded. Figure 1 (b) illustrates the definition of these assumed tau-positive clusters. All further analyses were based on [^{18}F]PI-2620 binding in these clusters.

Kinetic modeling and extraction of [^{18}F]PI-2620 binding parameters. We evaluated different kinetic modeling approaches to test for robustness of similar parameters among these models. Non-invasive kinetic modelling approaches (simplified reference tissue modeling approaches 1 & 2 (SRTM & SRTM2) and MRTM2) were separately ran for all [^{18}F]PI-2620-positive clusters with the cerebellar reference tissue by PMOD. R1 values as a surrogate of delivery as well as k_2 & k_{2a} efflux rate parameters as surrogate of dissociation from the target were extracted from SRTM and SRTM2. A lower limit of 0.006/min and an upper limit of 0.6/min were set for k_{2a} and clusters reaching these limits were excluded. DVR values as a parameter for overall binding magnitude were extracted from all models and reported for MRTM2. A lower limit of 0 and an upper limit of 5 were set for DVR and clusters reaching these limits were excluded. Delivery, efflux rate and DVR deriving from different models were correlated with each other to test for their robustness. k_2' and t^* (equilibration time) were fixed across models. In addition, late binding phase uptake as a surrogate for the binding magnitude was obtained from static images between 30 and 60 minutes p.i. (SUVR_{30-60}). The cluster-to-cerebellum SUVRs were computed in each frame for a model-independent evaluation of the signal kinetic. Linear functions were calculated for all intervals i-60 min p.i. starting at 9 min p.i. (i.e. 9–60 min p.i., 11–60 min p.i., etc.) and the slopes were used for characterizing the post-perfusion binding phase.

Statistics

A sample size of 6 patients per group (3/4R and 4R) gave a power of >0.8 when using previous DVR data³² for sample size estimation ($\alpha=0.05$; cortex 3/4R: mean 1.17 SD 0.20; cortex 4R: mean 0.89 SD 0.07) by G*Power (V3.1.9.2, Kiel, Germany). Regional cluster volumes, R1-values, k2 & k2a values, DVR, SUVR₃₀₋₆₀, and the slope were compared between 3/4R and 4R tauopathies by a two-sample t-test. For comparisons between different tau-positive regions, a one-way analysis of variance was applied (>2 comparison groups). All analyses were conducted using SPSS 25 (V25, IBM, Ehningen, Germany) and GraphPad Prism 8 (GraphPad Software, San Diego, USA). Receiver operating characteristics (ROC) were used to calculate the area under the curve (AUC) for discriminating 3/4R vs. 4R tauopathy by the above read-outs. Furthermore, a principal component analysis (PCA) of five parameters (R1 with highest AUC, k2 & k2a with highest AUC, DVR, SUVR₃₀₋₆₀, slope with highest AUC) was performed in SPSS and also subject to ROC evaluation. Linear relationship of the data was tested by a correlation matrix and items with a correlation coefficient <0.3 were discarded. The Kaiser-Meyer-Olkin (KMO) measure and Bartlett's test of sphericity were used to test for sampling adequacy and suitability for data reduction. Components with an Eigenvalue >1.0 were extracted and a varimax rotation was included.

Data availability

Data of this manuscript are available through contacting the corresponding author upon reasonable request.

Results

Demographics and [¹⁸F]PI-2620-positive clusters in clinically diagnosed 3/4R and 4R tauopathies

10 patients with a clinically diagnosed 3/4R tauopathy (10 AD continuum) and 29 patients with a clinically diagnosed 4R tauopathy (14 CBS, 15 PSP) according to current diagnostic criteria, all with a discernible [¹⁸F]PI-2620 cortical signal in visual evaluation, were enrolled for this evaluation. 3/4R tauopathy patients (65.7 ± 10.1 y; 70% female), 4R tauopathy patients (71.0 ± 7.2 y; 38% female) and healthy controls (67.5 ± 6.7 y; 73% female) did not differ significantly in age.

Suitability of the reference tissue was validated by similarity of time-activity-curves, SUV (3/4R: 0.36 ± 0.07 g/ml; 4R: 0.37 ± 0.09 g/ml; healthy controls: 0.38 ± 0.08 g/ml), and their coefficients of variation (3/4R: 18%; 4R: 25%; healthy controls: 21%) in the study groups (Supplemental Figure 2). The frequency and regional volumes of cortical and subcortical [¹⁸F]PI-2620-positive clusters in 3/4R and 4R tauopathies are shown in Table 1. The 3/4R tauopathy group showed [¹⁸F]PI-2620-positive clusters in nearly all cortical regions, whereas the frequency of [¹⁸F]PI-2620-positive clusters in cortical regions was lower in 4R cases. The 4R tauopathy group showed a higher percentage of [¹⁸F]PI-2620-positive subcortical clusters when compared to 3/4R cases (77% vs. 35%, $p < 0.0001$).

The volume of combined cortical [¹⁸F]PI-2620-positive clusters was larger for the 3/4R tauopathy group when compared to the 4R tauopathy group

Table 1. Frequency and regional volume of target clusters in 3/4R (10 patients) and 4R tauopathies (29 patients).

	3/4R tauopathy		4R tauopathy		P-value (volume)
	Volume (mean \pm SD (ccm))	n	Volume (mean \pm SD (ccm))	n	
Cortical	54.4 \pm 51.6	79	4.8 \pm 11.1	167	<0.0001
Frontal L	76.2 \pm 85.4	10	6.4 \pm 14.5	26	0.0002
Frontal R	79.2 \pm 92.0	10	8.7 \pm 19.3	25	0.0007
Occipital L	41.8 \pm 27.1	10	6.4 \pm 10.2	15	0.0001
Occipital R	38.1 \pm 30.7	10	4.7 \pm 8.9	18	0.0002
Parietal L	45.2 \pm 34.7	10	3.4 \pm 7.0	20	<0.0001
Parietal R	50.0 \pm 35.0	9	3.0 \pm 6.6	20	<0.0001
Temporal L	55.2 \pm 18.1	10	3.0 \pm 5.7	21	<0.0001
Temporal R	48.8 \pm 34.4	10	2.2 \pm 4.2	22	<0.0001
Subcortical	1.8 \pm 1.9	14	2.0 \pm 1.7	89	0.6871
Putamen L	1.3 \pm 1.3	4	2.8 \pm 1.8	24	0.1245
Putamen R	2.5 \pm 2.4	7	2.8 \pm 1.8	27	0.6802
G. Pallidus L	–	0	0.8 \pm 0.3	17	–
G. Pallidus R	0.9 \pm 0.8	3	1.0 \pm 0.6	21	0.8076

Note: P values derive from an unpaired t-test for the comparison of regional cluster volumes between 3/4R and 4R tauopathies. L: left; R: right; SD: standard deviation.

($54.4 \pm 51.6 \text{ mm}^3$ vs. $4.8 \pm 11.1 \text{ mm}^3$, $p < 0.0001$), whereas there was no volume difference between both groups for combined subcortical clusters ($1.8 \pm 1.9 \text{ mm}^3$ vs. $2.0 \pm 1.7 \text{ mm}^3$, $p = 0.687$).

Kinetic modeling parameters in comparison between 3/4R and 4R tauopathies

To estimate kinetic properties of [^{18}F]PI-2620, R1 and k2 & k2a-values were compared between groups of 3/4R and 4R tauopathies and between cortical and subcortical brain regions (Table 2). 88% of the MRTM2 defined [^{18}F]PI-2620-positive clusters resulted in modeling parameters within the defined threshold ranges for the applied kinetic models. Delivery, efflux and binding parameters of different models correlated highly with each other (delivery: all $R > 0.9$; k2 & k2a: all $R > 0.99$).

In cortical regions, [^{18}F]PI-2620-positive clusters of 4R tauopathy cases had higher R1 (all $p < 0.05$) and k2 & k2a (all $p < 0.0001$) values when compared to 3/4R tauopathy cases, suggesting a faster tracer delivery and efflux from the target in the presence of 4R tau (Figure 2(a)). Subcortical clusters did not show differences of R1 and k2 & k2a values between 4R and 3/4R tauopathies, indicating similar delivery and efflux of [^{18}F]PI-2620 to subcortical regions for both types of tau (Figure 2(b)).

Next, we asked whether [^{18}F]PI-2620 binding characteristics are different between cortical and subcortical brain regions. 3/4R tauopathy subjects had elevated R1

and elevated k2 & k2a values in subcortical areas, when compared to [^{18}F]PI-2620-positive cortical clusters (Figure 2(c)). Within 4R-tauopathies, R1 of SRTM2 was lower in cortical clusters when compared to subcortical clusters (0.88 ± 0.20 vs. 0.96 ± 0.14 , $p = 0.0018$; Figure 2(d)). We observed the lowest k2 & k2a values in cortical clusters of 3/4R tauopathy cases.

Binding magnitude in comparison between 3/4R and 4R tauopathies

[^{18}F]PI-2620 binding was assessed for the full 60-minutes scan (DVR) and a binding surrogate was obtained for the late uptake phase (SUVR₃₀₋₆₀). 3/4R tauopathy cases showed significantly higher DVR values in all cortical [^{18}F]PI-2620-positive clusters when compared to 4R tauopathies (Table 3).

SUVR₃₀₋₆₀ were consistently higher in [^{18}F]PI-2620-positive cortical clusters of 3/4R tauopathy patients when compared to 4R tauopathy patients. Subcortical areas indicated a higher binding magnitude for [^{18}F]PI-2620-positive clusters in patients with 4R tauopathies when compared to 3/4R tauopathies.

Slope of binding during the post-perfusion phase

[^{18}F]PI-2620 time-SUVR curves of both diagnostic groups clearly separated over time for all cortical brain areas but not for subcortical regions (Figure 3 (a) and (b)). Time-SUVR curves of 3/4R subjects showed a continuous increase in all cortical areas

Table 2. Delivery (R1) and efflux (k2 & k2a) parameters of [^{18}F]PI-2620-positive clusters in cortical and subcortical brain areas.

	SRTM R1 (unitless \pm SD)	SRTM2 R1 (unitless \pm SD)	SRTM k2 (1/min \pm SD)	SRTM k2a (1/min \pm SD)	SRTM2 k2a (1/min \pm SD)
Cortical PI-2620-positive clusters					
3/4R	0.83 ± 0.10	0.83 ± 0.10	0.06 ± 0.07	0.05 ± 0.07	0.05 ± 0.07
4R	0.92 ± 0.21	0.88 ± 0.20	0.17 ± 0.21	0.15 ± 0.19	0.15 ± 0.19
p value (3/4R vs. 4R)	0.0007	0.0380	<0.0001	<0.0001	<0.0001
HC	0.87 ± 0.11	0.83 ± 0.08	0.17 ± 0.23	0.19 ± 0.26	0.07 ± 0.17
Subcortical PI-2620-positive clusters					
3/4R	1.02 ± 0.15	1.02 ± 0.15	0.25 ± 0.20	0.19 ± 0.16	0.19 ± 0.16
4R	0.96 ± 0.14	0.96 ± 0.14	0.21 ± 0.14	0.16 ± 0.11	0.16 ± 0.11
p value (3/4R vs. 4R)	0.1515	0.1431	0.3657	0.2924	0.2698
HC	0.77 ± 0.10	0.77 ± 0.09	0.14 ± 0.14	0.16 ± 0.17	0.07 ± 0.10
3/4R tauopathies					
Cortical	0.83 ± 0.10	0.83 ± 0.10	0.06 ± 0.07	0.05 ± 0.07	0.05 ± 0.07
Subcortical	1.02 ± 0.15	1.02 ± 0.15	0.25 ± 0.20	0.19 ± 0.16	0.19 ± 0.16
p value (cortical vs. subcortical)	<0.0001	<0.0001	<0.0001	<0.0001	<0.0001
4R tauopathies					
Cortical	0.92 ± 0.21	0.88 ± 0.20	0.17 ± 0.21	0.15 ± 0.19	0.15 ± 0.19
Subcortical	0.96 ± 0.14	0.96 ± 0.14	0.21 ± 0.14	0.16 ± 0.11	0.16 ± 0.11
p value (cortical vs. subcortical)	0.1019	0.0018	0.1545	0.8293	0.8293

Note: Values of healthy controls (HC) were extracted from atlas regions and serve for an orienting comparison, whereas values of 3/4R and 4R tauopathies were derived from [^{18}F]PI-2620 positive clusters.

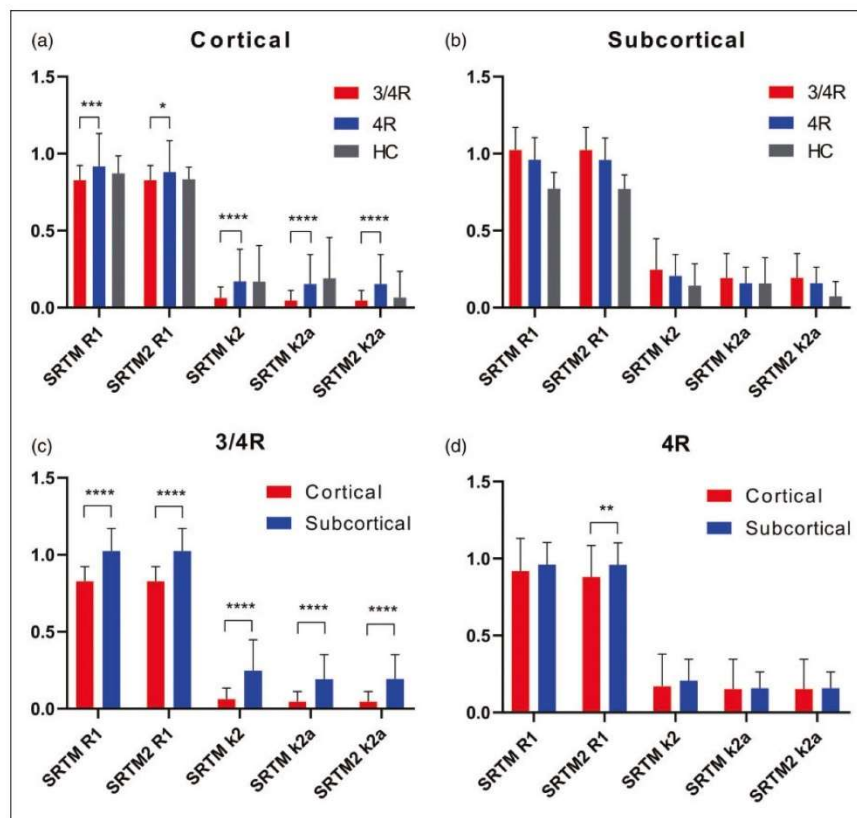


Figure 2. Kinetic modelling parameter of delivery and efflux of [^{18}F]PI-2620 in comparison of clinically diagnosed 3/4R ($n = 10$) and 4R ($n = 29$) tauopathies. Delivery and efflux of 4R tauopathy patients were higher in [^{18}F]PI-2620-positive cortical clusters (a) but not different in subcortical clusters (b). Subcortical clusters showed higher delivery and/or efflux parameters when compared to cortical clusters regardless of the patient group (c, d). Data of healthy controls (HC) were extracted from atlas regions and serve for an orienting comparison. Error bars represent standard deviation of study groups. * $p < 0.05$, ** $p < 0.01$, *** $p < 0.001$, and **** $p < 0.0001$ indicate significant differences between 3/4R and 4R tauopathies as assessed by an unpaired Student's t-test.

over nearly all frames, whereas cortical time-SUVR curves of 4R subjects reached a plateau at 30 min after injection for parietal cortex or even decreased from 30 min after injection for frontal cortex (Supplemental Figure 3). In subcortical regions, time-SUVR curves of 3/4R subjects did not separate from those of 4R subjects in both putamen and globus pallidus and showed a similar decrease from 30 to 60 min p.i. (Supplemental Figure 3).

Based on these findings we plotted single frame [^{18}F]PI-2620 SUVR as a linear function of time between 9 to 60 min and extracted the slope of the equation for each single cluster to enable a quantitative comparison between 3/4R and 4R tauopathies. The slope was nearly exclusively positive in cortical regions and nearly exclusively negative in subcortical regions for

all evaluated time intervals, regardless of the assumed tau isoform (Figure 3(a) and (b)). Strikingly, in cortical regions the slope of 3/4R tauopathy cases was much steeper when compared to 4R tauopathy cases for all time intervals, also discernible by visual interpretation of single cases (Figure 3(c)). The strongest discrimination of the slope between 3/4R and 4R tauopathies was observed for the time interval between 9 and 60 min (slope₉₋₆₀: $0.016/\text{min} \pm 0.008/\text{min}$ vs. $0.006/\text{min} \pm 0.007/\text{min}$, $p < 0.0001$, AUC: 0.824; Figure 4(a)). In the direct contrast to cortical areas, subcortical regions only indicated minor differences of the slope between 3/4R and 4R tauopathies, comprising stronger negative values in 4R tauopathies for late time intervals (i.e. slope₄₀₋₆₀: $-0.002/\text{min} \pm 0.008/\text{min}$ vs. $-0.010/\text{min} \pm 0.011/\text{min}$; $p = 0.010$).

Table 3. Distribution volume ratios (DVR) and standardized uptake value ratios between 30 and 60 minutes post injection (SUV₃₀₋₆₀) of [¹⁸F]PI-2620-positive clusters in cortical and subcortical brain areas.

	SUV ₃₀₋₆₀														
	DVR						SUV ₃₀₋₆₀								
	3/4R tauopathy		4R tauopathy		P		Healthy controls		3/4R tauopathy		4R tauopathy		P		Healthy controls
Mean ± SD	n	Mean ± SD	n	Mean ± SD	n	Mean ± SD	n	Mean ± SD	n	Mean ± SD	n	Mean ± SD	n	Mean ± SD	n
Cortical	1.38 ± 0.18	79	1.13 ± 0.10	167	<0.0001	88	1.76 ± 0.34	79	1.31 ± 0.20	167	<0.0001	88	1.05 ± 0.06	88	<0.0001
Frontal L	1.27 ± 0.12	10	1.11 ± 0.06	26	<0.0001	11	1.58 ± 0.26	10	1.26 ± 0.11	26	<0.0001	11	1.01 ± 0.06	11	<0.0001
Frontal R	1.24 ± 0.17	10	1.10 ± 0.07	25	0.0012	11	1.54 ± 0.32	10	1.24 ± 0.14	25	0.0005	11	1.00 ± 0.05	11	0.0023
Occipital L	1.45 ± 0.19	10	1.20 ± 0.09	15	0.0002	11	1.84 ± 0.41	10	1.38 ± 0.27	15	<0.0001	11	1.10 ± 0.05	11	<0.0001
Occipital R	1.43 ± 0.19	10	1.14 ± 0.05	18	<0.0001	11	1.83 ± 0.37	10	1.30 ± 0.14	18	<0.0001	11	1.09 ± 0.04	11	<0.0001
Parietal L	1.44 ± 0.23	10	1.09 ± 0.06	20	<0.0001	11	1.84 ± 0.39	10	1.28 ± 0.11	20	<0.0001	11	1.04 ± 0.05	11	<0.0001
Parietal R	1.43 ± 0.21	9	1.07 ± 0.08	20	<0.0001	11	1.86 ± 0.39	9	1.25 ± 0.14	20	<0.0001	11	1.04 ± 0.04	11	<0.0001
Temporal L	1.42 ± 0.09	10	1.20 ± 0.13	21	<0.0001	11	1.83 ± 0.17	10	1.38 ± 0.29	21	<0.0001	11	1.06 ± 0.06	11	<0.0001
Temporal R	1.40 ± 0.12	10	1.18 ± 0.15	22	0.0003	11	1.79 ± 0.27	10	1.40 ± 0.29	22	0.0011	11	1.07 ± 0.05	11	0.0011
Subcortical	1.22 ± 0.17	14	1.32 ± 0.09	89	0.0012	44	1.16 ± 0.25	14	1.38 ± 0.17	89	<0.0001	44	0.98 ± 0.14	44	<0.0001
Putamen L	1.24 ± 0.20	4	1.35 ± 0.08	24	0.0569	11	1.15 ± 0.26	4	1.37 ± 0.15	24	0.0200	11	0.89 ± 0.09	11	0.0200
Putamen R	1.18 ± 0.20	7	1.30 ± 0.12	27	0.0539	11	1.14 ± 0.30	7	1.29 ± 0.18	27	0.0978	11	0.88 ± 0.09	11	0.0978
G. Pallidus L	–	0	1.32 ± 0.06	17	–	11	0.87 ± 0.07	0	1.46 ± 0.17	17	–	11	1.05 ± 0.08	11	–
G. Pallidus R	1.28 ± 0.07	3	1.31 ± 0.08	21	0.5417	11	1.24 ± 0.17	3	1.44 ± 0.14	21	0.0337	11	1.12 ± 0.11	11	0.0337

Note: Values of healthy controls (HC) were extracted from atlas regions and serve for an orienting comparison, whereas values of 3/4R and 4R tauopathies were derived from [¹⁸F]PI-2620 positive clusters. L: left; R: right.

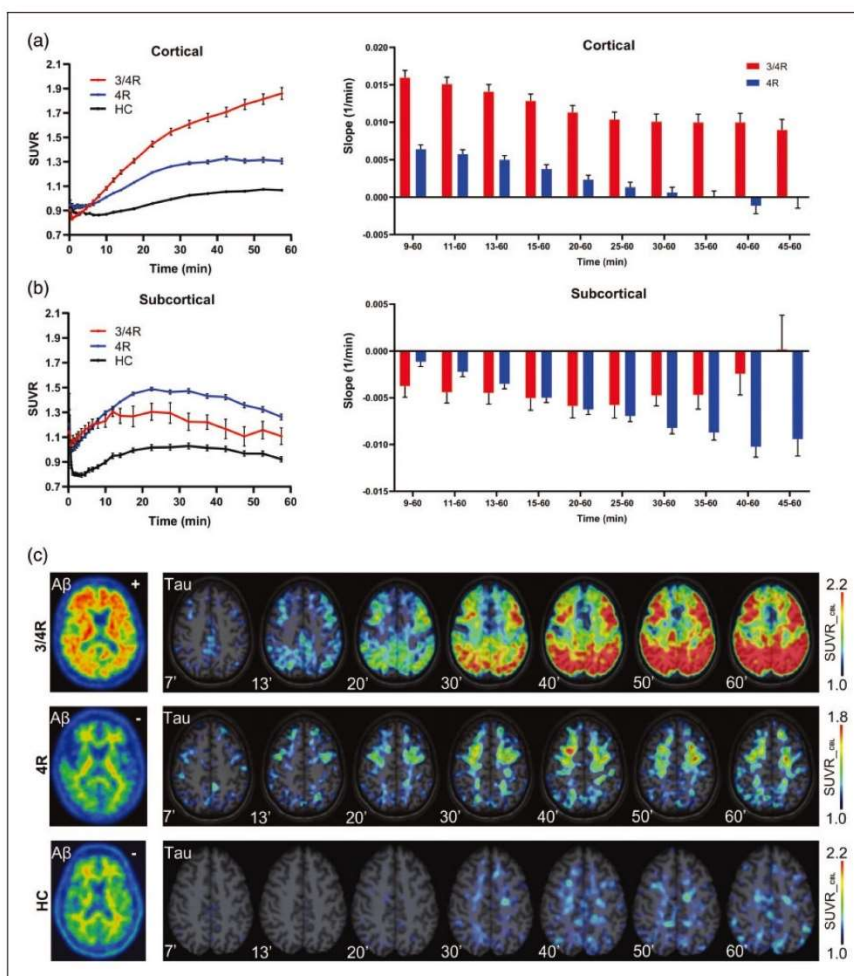


Figure 3. (a,b) Time–SUVR curves in the comparison of clinically diagnosed 3/4R ($n = 10$), 4R ($n = 29$) tauopathies, and healthy controls (HC) together with the slope of different time intervals during the post-perfusion phase. Time–SUVR values of HC were extracted from atlas regions, whereas time–SUVR values of 3/4R and 4R tauopathies were derived from [^{18}F]PI-2620 positive clusters. (c) Native β -amyloid-PET images together with tau-PET SUVR images of cortical areas for exemplary cases of patients with 3/4R and 4R tauopathies and a healthy control in different time frames of the post-perfusion phase. Axial slices show [^{18}F]PI-2620 SUVR upon an MRI atlas. Error bars represent standard error (SEM) of single frame values and intervals in study groups.

Merged value of all kinetic modeling parameters for the discrimination of 3/4R and 4R tauopathies

A comparison of kinetic modeling parameters, DVR, SUVR, and slopes of 3/4R and 4R tauopathies were conducted to estimate the feasibility of predicting a 3/4R tauopathy by [^{18}F]PI-2620 PET. To this end we performed a ROC analysis and computed AUC of all evaluated parameters.

AUCs of the different slope intervals were highest for the longest interval (slope₉₋₆₀, AUC: 0.824) and decreased with elapsed scan duration (slope₄₅₋₆₀,

AUC: 0.714; Figure 4(a)). AUCs for delivery and efflux parameters from different kinetic models were similar (Figure 4(b)). ROC of DVR (AUC: 0.922) and SUVR₃₀₋₆₀ (AUC: 0.906) resulted in a stronger prediction of a 3/4R tauopathy in cortical [^{18}F]PI-2620-positive clusters when compared to the best slope₉₋₆₀ (AUC: 0.824), the best delivery (AUC: 0.654) and the best efflux discriminations (AUC: 0.716; Figure 4(c)).

The principal component analysis resulted in a KMO sampling adequacy of 0.539 and Bartlett's test of sphericity was significant ($p < 0.001$). We found two

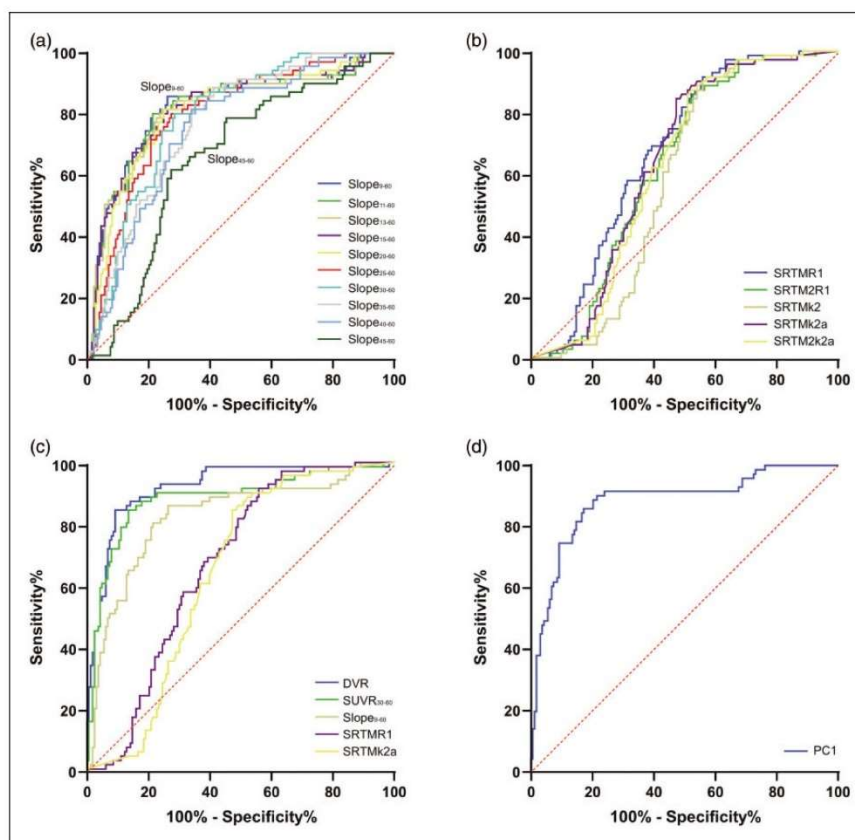


Figure 4. ROC comparison for differentiation of 3/4 R ($n=10$) tauopathies from 4 R ($n=29$) tauopathies. ROC curves are shown for (a) slopes in different intervals of the post-perfusion phase, (b) delivery and efflux parameters deriving from different modelling approaches, (c) in contrast of all single study read outs, and (d) for the principal component 1 of all read outs. Only read outs of cortical clusters were used for the ROC analysis.

principal components with an Eigenvalue > 1.0 (principal component 1: 2.729, principal component 2: 1.491) which explained 84.4% of the variance. The component matrix for the principal component 1 was 0.980 for $SUVR_{30-60}$, 0.908 for DVR and 0.901 for $slope_{9-60}$. The component matrix for the principal component 2 was 0.879 for $R1_{SRTM}$ and 0.877 for $k2a_{SRTM}$. AUC for the discrimination of 3/4R and 4R tauopathies by principal component 1 was 0.899 (Figure 4(d)) and 0.669 for principal component 2.

Discussion

This is the first study investigating the kinetic and binding characteristics of [^{18}F]PI-2620 in different brain regions of clinically diagnosed 3/4R and 4R tauopathies by non-invasive reference tissue modelling. We demonstrate that [^{18}F]PI-2620-positive clusters of

clinically diagnosed 4R tauopathy cases have higher delivery and efflux parameters when compared to similar clusters in clinically diagnosed 3/4R tauopathies. This finding was also reflected by lower slopes of time-activity-ratio curves between 9 and 60 minutes after tracer injection for cortical clusters in 4R tauopathies when compared to 3/4R tauopathies. We consider this effect as the *in vivo* correlate of the reported lower [^{18}F]PI-2620 affinity to 4R tau *in vitro*. Binding characteristics in subcortical brain regions are dominated by higher delivery and efflux when compared to cortical regions. Ultimately, the assumed presence of 3/4R and 4R tau in the individual brain can be differentiated by the kinetic and binding characteristics of [^{18}F]PI-2620.

In this study, we report kinetic modeling results for dynamic 0- to 60-min [^{18}F]PI-2620 PET scans in patients with 3/4R and 4R tauopathies. We observed

enhanced R1 and k2 & k2a values in cortical [^{18}F]PI-2620-positive clusters of the 4R tauopathy group compared to the 3/4R tauopathy group (Table 2). The stronger efflux of the tracer from the target in 4R tauopathies was visually confirmed by clearly separated cortical time-SUVR curves of 3/4R- and 4R-tau cases with increasing scan duration and the visual inspection of single frame images. In particular, SUVR of all cortical regions of 3/4R-tau cases kept increasing over time, while time-SUVR curves of parietal and frontal cortices of 4R tau-cases reached a plateau or had a slight decrease in the late phase (Supplemental Figure 3). This indicates that 4R-tau cases have a slightly higher delivery rate from blood to assumed tau-positive cortical target regions and a significantly higher clearance rate to blood. The higher efflux parameters suggest a less stable binding of [^{18}F]PI-2620 to 4R tau in comparison to 3/4R tau which is in line with the lower affinity of this tracer to synthetic 4R tau fibrils when compared to 3/4R fibrils.²⁵ The radioligand [^{18}F]flortaucipir, aka [^{18}F]AV-1451, is the by far most widely studied tau-PET tracer to date. Similar to our study, one previous study clearly demonstrated that AV-1451 has unique *in vivo* binding properties for assumed AD-like tau pathology among MAPT mutation carriers.⁴⁴ Besides the consistent *in vivo* retention of [^{18}F]AV-1451, *in vitro* autoradiography suggest that [^{18}F]AV-1451 displays strong binding affinity to paired helical filaments tau in Alzheimer's disease, but exhibits low affinity to tau aggregates primarily made of straight tau filaments in these non-Alzheimer tauopathies.^{5,45,46} Similarly, another study has shown poor binding of [^{18}F]AV-1451 to non-AD tauopathies that have an accumulation of either 3R or 4R tau.⁴⁷ The reasons for the binding differences of [^{18}F]PI-2620 and [^{18}F]AV-1451 for 3/4R and 4R tau isoforms are not yet understood. A potential explanation could be based on a different configuration of tracer binding pockets in the different forms of tau aggregates. Cryo-electron microscopy (cryoEM) studies recently showed that paired helical filaments and straight filaments of 3/4R tau from AD contained the same C-shape protofibril structure whereas the 4R tau-structure obtained from CBD was distinctly different.⁴⁸ Detailed analysis of the tracer binding sites at the ultra-structure level using cryoEM could potentially elucidate the mechanisms behind the different specificity of [^{18}F]PI-2620 and other tau tracers to different isoforms and filaments of tau. Kroth and coworkers recently described the preclinical comparison of [^{18}F]AV1451 and [^{18}F]RO948 with other fluoropyridine regioisomers.²⁵ They found that different regioisomers gave rise to a remarkably diverse set of characteristics with regard to their binding affinity for AD and PSP tau, off-target binding to beta-amyloid and

monoamine oxidases A or B as well as global brain uptake and washout in mice. Based on this preclinical comparison, [^{18}F]PI-2620 was selected as clinical candidate with optimized binding to AD but also to PSP.

Tracer kinetics and binding characteristics of [^{18}F]PI-2620 in clusters of subcortical areas were not different between clinically diagnosed 3/4R and 4R tauopathies. Since inverted U-shape time-SUVR curves of [^{18}F]PI-2620 were also observed in healthy controls,³² we speculate that the effect of binding affinity to tau deposition is dominated by the general tracer kinetics in subcortical regions. Our findings of higher initial uptake and much faster clearance in the putamen and the globus pallidus in comparison to cortical regions are similar to reports on kinetic characteristics of [^{18}F]AV-1451.^{49–51} Keeping in mind that our [^{18}F]PI-2620 study analyzed assumed tau-positive clusters and earlier [^{18}F]AV-1451 studies used predefined brain regions, the increasing time-SUVR curves for AD subjects and the inverted U-shape of time-SUVR curves for 4R tauopathy subjects of our study correspond well with the aforementioned studies. Similar to our obtained delivery parameter R1, k1 of [^{18}F]AV-1451 was highest in the putamen and lower for cortical regions.⁵⁰ Another study on [^{18}F]AV-1451 showed that the putamen of AD subjects has a higher SUVR at the initial wash-in stage, reaching a steady-state condition at 40–50 min post-injection.⁵² Generally, lower subcortical SUVR of [^{18}F]PI-2620 in comparison to [^{18}F]AV-1451 might suggest lower off-target binding in the basal ganglia, which would be an improvement of next-generation tau-PET imaging.^{14,32} These findings indicate that some subcortical binding of both tracers is probably caused by yet unknown mechanisms potentially involving a secondary binding site with different kinetics or extra off-target binding in addition to the specific binding to tau aggregates. Another potential mechanism could rely on different capillary permeability between brain regions, supposing a higher capillary permeability in subcortical areas, which implies an increased extraction through the blood-brain barrier, in the putamen and the globus pallidus but not in the cerebral cortex.⁵³ Although we cannot rule out non-specific binding or off-target binding, the clear basal ganglia [^{18}F]PI-2620 binding pattern of some AD cases (~30%) could be explained by a recent Japanese autopsy study, which reported on the presence of tau in the basal ganglia of AD cases.⁵⁴ Our current data support the hypothesis that even low deposition of 3/4R tau in the basal ganglia of AD could cause a higher PET signal when compared to strong 4R tau deposition in the basal ganglia of PSP cases.

The main focus of our study was to translate non-invasive kinetic modelling of [^{18}F]PI-2620 PET data into an application for differential diagnosis.

The differentiation of tauopathies is important since there are overlapping clinical syndromes in presence of different tau isoforms. For example, there is an underestimated overlap of the phenotype (amnesic mild cognitive impairment) between AD and argyrophilic grain disease at early stages³⁴ and AD-CBS and 4R CBS both manifest in motor areas of the frontal lobe.⁵⁵ As an internal validation of our data, we applied different non-invasive approaches of simplified and multilinear kinetic modelling and observed highly similar parameters of binding characteristics between them. We suggested earlier that the development of selective 4R tracers could facilitate the differentiation of 4R-tauopathies not only from healthy controls but also from AD cases with predominant presence of 3/4R tau.³¹ Despite the different magnitude and spatial extent of brain tau deposition, [¹⁸F]PI-2620 binding properties were already able to differentiate 3/4R from 4R tauopathies. Importantly, this was not only true for regions exclusively assumed tau-positive in either of 3/4R or 4R tauopathies but also in overlapping regions, i.e. the frontal cortex. Thus, although [¹⁸F]PI-2620 is likely not specific to 3/4R- or 4R tau, the AUC of kinetic modeling parameter and binding characteristics suggest feasibility of differential diagnosis between 3/4R and 4R tauopathies. We implemented a principal component analysis which did not indicate higher AUC values for discrimination when compared to single parameters of binding magnitude. This is probably related to the composition of our patient cohort, which includes a high proportion of severe cases in the 3/4R group. Thus, a potential additive value of assessing the principal component of all parameters or the slope of the late binding phase needs to be explored by future cases with similar binding magnitude. The rationale for the assessment of the slope in the late binding phase was based on the possibility to assess this parameter also in a late imaging window between 30 and 60 minutes p.i. While the slope between 9 and 60 minutes p.i. separated better between 3/4R and 4R tauopathy patients, the discrimination was still present for the slope between 30 and 60 minutes p.i., providing an alternative when economic reasons or patient compliance do not allow dynamic scanning. The methodology could be of interest for target engagement when future anti-tau treatments are specific for 3/4R tau or 4R isoforms. The assessment of the early phase as a surrogate biomarker of neuronal injury⁵⁶ adds another part to the toolbox of this tracer when dynamic imaging is performed. The current dataset was too small to evaluate multi-parameter classification approaches or artificial intelligence for prediction of 3/4R and 4R tauopathy cases but such methods are likely interesting when larger [¹⁸F]PI-2620 cohorts will be available.

Among the limitations of the study we focused on non-invasive kinetic modeling and our data are lacking full quantification by arterial blood sampling. Thus, we are not able to test for effects of different tracer plasma levels and tracer metabolism of [¹⁸F]PI-2620 in the investigated subjects. Furthermore, our assumptions of modeling parameters rely on simplified reference region methodology which can be subject to bias and variability when compared to arterial input measures. However, due to the rare incidence and severe disability of 4R tauopathy patients our current dataset likely provides a good compromise between clinical feasibility and accuracy. To account for the prerequisites of reference tissue modeling we chose the previously established cerebellar reference tissue excluding the dentate nucleus to generate a compartment with assumed negligible specific binding in 3/4R and 4R tauopathies.³² We used a simple linear fit for the slope of the late binding phase and we note that this fit is imperfect for cases with an inverted U-shape of their time-activity-curve. While more flexible fits could further improve the methodology, the proposed approach will more likely be transferable to clinical scenarios. Clinical applicability was also the reason to not apply partial volume effect correction in the current study design. This is a limitation, as atrophy is related to lower fit values of R1 and lower [¹⁸F]PI-2620 binding. We used the slope of the time-activity-ratio-curve to characterize the late binding phase and also found a strong discrimination between 3/4R and 4R tauopathies. This index should be less affected by atrophy since atrophy would affect all frames of the late binding phase at a similar magnitude. Future studies should investigate the impact of atrophy on kinetic modeling parameters by comparison of patients with mild and strong neurodegeneration. Future work should also investigate the impact of factors associated with tau binding (such as *APOE*) on kinetic modeling parameters in larger cohorts. We note that diagnoses of the heterogeneous patient cohort were built on clinical diagnosis criteria, but they were lacking postmortem validation. Therefore, clinical misdiagnosis could bias the primary outcome measures of this study. Because clinical 3R tauopathy patients were not enrolled in this study, we were not able to investigate the kinetic and binding characteristics of [¹⁸F]PI-2620 to 3R tau *in vivo*.

In conclusion, [¹⁸F]PI-2620 binding characteristics in cortical regions differentiate between 3/4R- and 4R-tauopathies and might serve as a supportive read-out in the diagnostic workup of neurodegenerative disorders. Higher tracer clearance in 4R tauopathies indicates less stable binding when compared to 3/4R-tauopathies, deserving attention when performing

comparative studies between patients with presence of different tau isoforms.

Funding

The author(s) disclosed receipt of the following financial support for the research, authorship, and/or publication of this article: LMI provided financial support to separate studies from which data are included in this analysis. G.U.H. was funded by the Deutsche Forschungsgemeinschaft (DFG, German Research Foundation) under Germany's Excellence Strategy within the framework of the Munich Cluster for Systems Neurology (EXC 2145 SyNergy – ID 390857198, G.U.H., P.B., S.Z., M.B.) the NOMIS foundation (FTLD project, G.U.H.), and VolkswagenStiftung/Lower Saxony Ministry for Science/Petermax-Müller Foundation (Etiology and Therapy of Synucleinopathies and Tauopathies). This project was supported by the German Center for Neurodegenerative Diseases (DZNE, DescribePSP Study) and the German Parkinson's Association (DPG, ProPSP Study).

Acknowledgements

We thank all patients, their care-givers, cyclotron, radiochemistry and PET imaging crews. Life Molecular Imaging (LMI) provided material support for the manufacturing of PI-2620 and was involved in the analysis and interpretation of the data.

Declaration of conflicting interests

The author(s) declared the following potential conflicts of interest with respect to the research, authorship, and/or publication of this article: M.B. received speaker honoraria from GE healthcare and LMI and is an advisor of LMI. M.T.B. received speaker's honoraria from Medtronic, Boston Scientific, Abbott (formerly St. Jude), GE Medical, UCB, Bial and research funding from the Felgenhauer-Stiftung, Forschungspool Klinische Studien (University of Cologne), H2020, Medtronic and Boston Scientific. C.P. received research funding from Lüneburg heritage. G.U.H. received research support from GE Healthcare and Neuropore; has ongoing research collaborations with Orion and Prothena; serves as a consultant for AbbVie, AlzProtect, Asceneuron, Biogen, Biohaven, Lundbeck, Novartis, Roche, Sanofi, UCB; received honoraria for scientific presentations from AbbVie, Biogen, Roche, Teva, UCB, and Zambon; and holds a patent on PERK Activation for the Treatment of Neurodegenerative Diseases (PCT/EP2015/068734). G.R. received honoraria for scientific presentations from Biogen and serves as a consultant for UCB. All other authors do not report a conflict of interest.

Authors' contributions

Dr Brendel had full access to all of the data in the study and takes responsibility for the integrity of the data and the accuracy of the data analysis.




Concept and design: Barthel, van Eimeren, Marek, Barret, Russell, Stephens, Bartenstein, Levin, Höglinger, Drzezga, Sabri, Ziegler, Boening, Brendel.

Acquisition, analysis, or interpretation of data: Song, Beyer, Kaiser, Barthel, van Eimeren, Marek, Nitschmann, Scheifele, Palleis, Respondek, Kern, Biechele, Hammes, Bischof, Barbe, Onur, Jessen, Saur, Schroeter, Rumpf, Rullmann, Schildan, Patt, Neumaier, Barret, Madonia, Russell, Stephens, Mueller, Roeber, Boetzel, Danek, Classen, Bartenstein, Villemagne, Höglinger, Drzezga, Seibyl, Sabri, Boening, Ziegler, Brendel. Drafting of the manuscript: Song, Beyer, Barthel, van Eimeren, Mueller, Drzezga, Sabri, Ziegler, Brendel.

Critical revision of the manuscript for important intellectual content: Song, Beyer, Kaiser, Barthel, van Eimeren, Marek, Nitschmann, Scheifele, Palleis, Respondek, Kern, Biechele, Hammes, Bischof, Barbe, Onur, Jessen, Saur, Schroeter, Rumpf, Rullmann, Schildan, Patt, Neumaier, Barret, Madonia, Russell, Stephens, Mueller, Roeber, Herms, Boetzel, Danek, Levin, Classen, Höglinger, Bartenstein, Villemagne, Drzezga, Seibyl, Sabri, Boening, Ziegler, Brendel. Statistical analysis: Song, Brendel.

Supervision: Beyer, Barthel, van Eimeren, Marek, Barret, Russell, Herms, Boetzel, Bartenstein, Villemagne, Levin, Höglinger, Drzezga, Seibyl, Sabri, Ziegler, Brendel.

ORCID iDs

Olivier Barret  <https://orcid.org/0000-0003-4247-184X>
David S Russell  <https://orcid.org/0000-0002-9105-2943>
Adrian Danek  <https://orcid.org/0000-0001-8857-5383>
Matthias Brendel  <https://orcid.org/0000-0002-9247-2843>

Supplementary material

Supplemental material for this article is available online.

References

- Pontecorvo MJ, Devous MD, Sr., Navitsky M, et al. Relationships between flortaucipir PET tau binding and amyloid burden, clinical diagnosis, age and cognition. *Brain* 2017; 140: 748–763.
- Bejanin A, Schonhaut DR, La Joie R, et al. Tau pathology and neurodegeneration contribute to cognitive impairment in Alzheimer's disease. *Brain* 2017; 140: 3286–3300.
- Nelson PT, Alafuzoff I, Bigio EH, et al. Correlation of Alzheimer disease neuropathologic changes with cognitive status: a review of the literature. *J Neuropathol Exp Neurol* 2012; 71: 362–381.
- Scholl M, Maass A, Mattsson N, et al. Biomarkers for tau pathology. *Mol Cell Neurosci* 2019; 97: 18–33.
- Coakeley S, Cho SS, Koshimori Y, et al. Positron emission tomography imaging of tau pathology in progressive supranuclear palsy. *J Cereb Blood Flow Metab* 2017; 37: 3150–3160.
- Iqbal K, Liu F and Gong CX. Tau and neurodegenerative disease: the story so far. *Nat Rev Neurol* 2016; 12: 15–27.
- Spillantini MG and Goedert M. Tau pathology and neurodegeneration. *Lancet Neurol* 2013; 12: 609–622.
- Iqbal K, Liu F, Gong CX, et al. Tau in Alzheimer disease and related tauopathies. *Curr Alzheimer Res* 2010; 7: 656–664.

9. Thal DR, Attems J and Ewers M. Spreading of amyloid, tau, and microvascular pathology in Alzheimer's disease: findings from neuropathological and neuroimaging studies. *J Alzheimers Dis* 2014; 42(Suppl 4): S421–429.
10. Liscic RM, Srulijes K, Groger A, et al. Differentiation of progressive supranuclear palsy: clinical, imaging and laboratory tools. *Acta Neurol Scand* 2013; 127: 362–370.
11. Dickson DW. Neuropathologic differentiation of progressive supranuclear palsy and corticobasal degeneration. *J Neurol* 1999; 246(Suppl 2): II6–15.
12. Grijalvo-Perez AM and Litvan I. Cortico basal degeneration. *Semin Neurol* 2014; 34: 160–173.
13. Taniguchi-Watanabe S, Arai T, Kametani F, et al. Biochemical classification of tauopathies by immunoblot, protein sequence and mass spectrometric analyses of sarkosyl-insoluble and trypsin-resistant tau. *Acta Neuropathol* 2016; 131: 267–280.
14. Leuzy A, Chiotis K, Lemoine L, et al. Tau PET imaging in neurodegenerative tauopathies – still a challenge. *Mol Psychiatry* 2019; 24: 1112–1134.
15. Leuzy A, Heurling K, Ashton NJ, et al. In vivo detection of Alzheimer's disease. *Yale J Biol Med* 2018; 91: 291–300.
16. Johnson KA, Schultz A, Betensky RA, et al. Tau positron emission tomographic imaging in aging and early Alzheimer disease. *Ann Neurol* 2016; 79: 110–119.
17. Scholl M, Lockhart SN, Schonhaut DR, et al. PET imaging of tau deposition in the aging human brain. *Neuron* 2016; 89: 971–982.
18. Harada R, Okamura N, Furumoto S, et al. 18F-THK5351: a novel PET radiotracer for imaging neurofibrillary pathology in Alzheimer disease. *J Nucl Med* 2016; 57: 208–214.
19. Maruyama M, Shimada H, Suhara T, et al. Imaging of tau pathology in a tauopathy mouse model and in Alzheimer patients compared to normal controls. *Neuron* 2013; 79: 1094–1108.
20. Brendel M, Schönecker S, Höglinger G, et al. [(18)F]-THK5351 PET correlates with topology and symptom severity in progressive supranuclear palsy. *Front Aging Neurosci* 2017; 9: 440–2018.
21. Fleisher AS, Pontecorvo MJ, Devous MD, et al. Positron emission tomography imaging with [18F]flortaucipir and postmortem assessment of Alzheimer disease neuropathologic changes. *JAMA Neurol* 2020; 77: 829.
22. Lemoine L, Gillberg PG, Svedberg M, et al. Comparative binding properties of the tau PET tracers THK5117, THK5351, PBB3, and T807 in postmortem Alzheimer brains. *Alzheimers Res Ther* 2017; 9: 96.
23. Ng KP, Pascoal TA, Mathotaarachchi S, et al. Monoamine oxidase B inhibitor, selegiline, reduces (18)F-THK5351 uptake in the human brain. *Alzheimers Res Ther* 2017; 9: 25.
24. Ishiki A, Harada R, Kai H, et al. Neuroimaging-pathological correlations of [(18)F]THK5351 PET in progressive supranuclear palsy. *Acta Neuropathol Commun* 2018; 6: 53.
25. Kroth H, Oden F, Molette J, et al. Discovery and pre-clinical characterization of [(18)F]PI-2620, a next-generation tau PET tracer for the assessment of tau pathology in Alzheimer's disease and other tauopathies. *Eur J Nucl Med Mol Imaging* 2019; 46: 2178–2189.
26. Okamura N, Harada R, Ishiki A, et al. The development and validation of tau PET tracers: current status and future directions. *Clin Transl Imaging* 2018; 6: 305–316.
27. Wang YT and Edison P. Tau imaging in neurodegenerative diseases using positron emission tomography. *Curr Neurol Neurosci Rep* 2019; 19: 45.
28. Fichou Y, Al-Hilaly YK, Devred F, et al. The elusive tau molecular structures: can we translate the recent breakthroughs into new targets for intervention? *Acta Neuropathol Commun* 2019; 7: 31.
29. Mueller A, Bullich S, Barret O, et al. Tau PET imaging with (18)F-PI-2620 in patients with Alzheimer's disease and healthy controls: a first-in-human study. *J Nucl Med* 2020; 61: 911–919.
30. Mormino EC, Toueg TN, Azevedo C, et al. Tau PET imaging with (18)F-PI-2620 in aging and neurodegenerative diseases. *Eur J Nucl Med Mol Imag* 2020; ■: ■.
31. Rösler TW, Tayaranian Marvian A, Brendel M, et al. Four-repeat tauopathies. *Prog Neurobiol* 2019; 180: 101644.
32. Brendel M, Barthel H, van Eimeren T, et al. Assessment of 18F-PI-2620 as a biomarker in progressive supranuclear palsy. *JAMA Neurol* 2020; 77: 1408–1419.
33. Ling H, O'Sullivan SS, Holton JL, et al. Does corticobasal degeneration exist? A clinicopathological re-evaluation. *Brain* 2010; 133: 2045–2057.
34. Rodriguez RD and Grinberg LT. Argyrophilic grain disease: an underestimated tauopathy. *Dement Neuropsychol* 2015; 9: 2–8.
35. Hoglinger GU, Respondek G, Stamelou M, et al. Clinical diagnosis of progressive supranuclear palsy: the movement disorder society criteria. *Mov Disord* 2017; 32: 853–864.
36. Hane FT, Robinson M, Lee BY, et al. Recent progress in Alzheimer's disease research, part 3: diagnosis and treatment. *J Alzheimers Dis* 2017; 57: 645–665.
37. Armstrong MJ, Litvan I, Lang AE, et al. Criteria for the diagnosis of corticobasal degeneration. *Neurology* 2013; 80: 496–503.
38. Dubois B, Feldman HH, Jacova C, et al. Advancing research diagnostic criteria for Alzheimer's disease: the IWG-2 criteria. *Lancet Neurol* 2014; 13: 614–629.
39. Jack CR, Jr., Bennett DA, Blennow K, et al. NIA-AA research framework: toward a biological definition of Alzheimer's disease. *Alzheimers Dement* 2018; 14: 535–562.
40. Jagust WJ, Landau SM, Koeppe RA, et al. The Alzheimer's disease neuroimaging initiative 2 PET core: 2015. *Alzheimers Dement* 2015; 11: 757–771.
41. Ichise M, Liow JS, Lu JQ, et al. Linearized reference tissue parametric imaging methods: application to [11C]DASB positron emission tomography studies of the serotonin transporter in human brain. *J Cereb Blood Flow Metab* 2003; 23: 1096–1112.
42. Hammers A, Allom R, Koeppe MJ, et al. Three-dimensional maximum probability atlas of the human brain, with particular reference to the temporal lobe. *Hum Brain Mapp* 2003; 19: 224–247.

43. Keuken MC, Bazin PL, Backhouse K, et al. Effects of aging on T(1), T(2)*, and QSM MRI values in the sub-cortex. *Brain Struct Funct* 2017; 222: 2487–2505.
44. Jones DT, Knopman DS, Graff-Radford J, et al. In vivo (18)F-AV-1451 tau PET signal in MAPT mutation carriers varies by expected tau isoforms. *Neurology* 2018; 90: e947–e954.
45. Marquie M, Normandin MD, Meltzer AC, et al. Pathological correlations of [F-18]-AV-1451 imaging in non-Alzheimer tauopathies. *Ann Neurol* 2017; 81: 117–128.
46. Marquie M, Normandin MD, Vanderburg CR, et al. Validating novel tau positron emission tomography tracer [F-18]-AV-1451 (T807) on postmortem brain tissue. *Ann Neurol* 2015; 78: 787–800.
47. Lowe VJ, Curran G, Fang P, et al. An autoradiographic evaluation of AV-1451 tau PET in dementia. *Acta Neuropathol Commun* 2016; 4: 58.
48. Zhang W, Tarutani A, Newell KL, et al. Novel tau filament fold in corticobasal degeneration. *Nature* 2020; 580: 283–287.
49. Baker SL, Lockhart SN, Price JC, et al. Reference tissue-based kinetic evaluation of 18F-AV-1451 for tau imaging. *J Nucl Med* 2017; 58: 332–338.
50. Barret O, Alagille D, Sanabria S, et al. Kinetic modeling of the tau PET tracer (18)F-AV-1451 in human healthy volunteers and Alzheimer disease subjects. *J Nucl Med* 2017; 58: 1124–1131.
51. Hahn A, Schain M, Erlandsson M, et al. Modeling strategies for quantification of in vivo (18)F-AV-1451 binding in patients with tau pathology. *J Nucl Med* 2017; 58: 623–631.
52. Shcherbinin S, Schwarz AJ, Joshi A, et al. Kinetics of the tau PET tracer 18F-AV-1451 (T807) in subjects with normal cognitive function, mild cognitive impairment, and Alzheimer disease. *J Nucl Med* 2016; 57: 1535–1542.
53. Pascual B, Rockers E, Bajaj S, et al. Regional kinetics of [18 F] AV-1451 uptake and gadolinium concentration in young and older subjects. In: *Poster presented at: the human amyloid imaging meeting*, January 13–15, Miami Beach, Florida, 2016.
54. Hamasaki H, Honda H, Suzuki SO, et al. Tauopathy in basal ganglia involvement is exacerbated in a subset of patients with Alzheimer's disease: the Hisayama study. *Alzheimers Dement* 2019; 11: 415–423.
55. Sakae N, Josephs KA, Litvan I, et al. Clinicopathologic subtype of Alzheimer's disease presenting as corticobasal syndrome. *Alzheimers Dement* 2019; 15: 1218–1228.
56. Beyer L, Nitschmann A, Barthel H, et al. Early-phase [(18)F]PI-2620 tau-PET imaging as a surrogate marker of neuronal injury. *Eur J Nucl Med Mol Imaging* 2020; 47: 2911–2922.

6. Paper II

European Journal of Nuclear Medicine and Molecular Imaging (2020) 47:2911–2922
<https://doi.org/10.1007/s00259-020-04788-w>

ORIGINAL ARTICLE



Early-phase [¹⁸F]PI-2620 tau-PET imaging as a surrogate marker of neuronal injury

Leonie Beyer¹ · Alexander Nitschmann¹ · Henryk Barthel² · Thilo van Eimeren^{3,4,5,6} · Marcus Unterrainer¹ · Julia Sauerbeck¹ · Ken Marek^{7,8} · Mengmeng Song¹ · Carla Palleis⁹ · Gesine Respondek^{9,10} · Jochen Hammes⁴ · Michael T. Barbe⁵ · Özgür Onur⁵ · Frank Jessen^{6,11,12} · Dorothee Saur¹³ · Matthias L. Schroeter^{14,15,16} · Jost-Julian Rumpf¹² · Michael Rullmann² · Andreas Schildan² · Marianne Patt² · Bernd Neumaier^{17,18} · Olivier Barret^{7,8} · Jennifer Madonia^{7,8} · David S. Russell^{7,8} · Andrew W. Stephens¹⁹ · Sigrun Roeber²⁰ · Jochen Herms^{10,20} · Kai Bötzel⁹ · Johannes Levin^{9,10} · Joseph Classen¹³ · Günter U. Höglinger^{10,21,22} · Peter Bartenstein^{1,23} · Victor Villemagne^{24,25,26} · Alexander Drzezga^{4,6} · John Seibyl^{7,8} · Osama Sabri² · Matthias Brendel^{1,23}

Received: 2 January 2020 / Accepted: 24 March 2020 / Published online: 21 April 2020
 © The Author(s) 2020

Abstract

Purpose Second-generation tau radiotracers for use with positron emission tomography (PET) have been developed for visualization of tau deposits in vivo. For several β -amyloid and first-generation tau-PET radiotracers, it has been shown that early-phase images can be used as a surrogate of neuronal injury. Therefore, we investigated the performance of early acquisitions of the novel tau-PET radiotracer [¹⁸F]PI-2620 as a potential substitute for [¹⁸F]fluorodeoxyglucose ([¹⁸F]FDG).

Methods Twenty-six subjects were referred with suspected tauopathies or overlapping parkinsonian syndromes (Alzheimer's disease, progressive supranuclear palsy, corticobasal syndrome, multi-system atrophy, Parkinson's disease, multi-system atrophy, Parkinson's disease, frontotemporal dementia) and received a dynamic [¹⁸F]PI-2620 tau-PET (0–60 min p.i.) and static [¹⁸F]FDG-PET (30–50 min p.i.). Regional standardized uptake value ratios of early-phase images (single frame SUVR) and the blood flow estimate (R_t) of [¹⁸F]PI-2620-PET were correlated with corresponding quantification of [¹⁸F]FDG-PET (global mean/cerebellar normalization). Reduced tracer uptake in cortical target regions was also interpreted visually using 3-dimensional stereotactic surface projections by three more and three less experienced readers. Spearman rank correlation coefficients were calculated between early-phase [¹⁸F]PI-2620 tau-PET and [¹⁸F]FDG-PET images for all cortical regions and frequencies of disagreement between images were compared for both more and less experienced readers.

Results Highest agreement with [¹⁸F]FDG-PET quantification was reached for [¹⁸F]PI-2620-PET acquisition from 0.5 to 2.5 min p.i. for global mean (lowest $R = 0.69$) and cerebellar scaling (lowest $R = 0.63$). Correlation coefficients (summed 0.5–2.5 min SUVR & R_t) displayed strong agreement in all cortical target regions for global mean ($R_{\text{SUVR}} = 0.76$, $R_{R_t} = 0.77$) and cerebellar normalization ($R_{\text{SUVR}} = 0.68$, $R_{R_t} = 0.68$). Visual interpretation revealed high regional correlations between early-phase tau-PET and [¹⁸F]FDG-PET. There were no relevant differences between more and less experienced readers.

Conclusion Early-phase imaging of [¹⁸F]PI-2620 can serve as a surrogate biomarker for neuronal injury. Dynamic imaging or a dual time-point protocol for tau-PET imaging could supersede additional [¹⁸F]FDG-PET imaging by indexing both the distribution of tau and the extent of neuronal injury.

Keywords Tau · PET · [¹⁸F]PI-2620 · Perfusion · Neuronal injury

This article is part of the Topical Collection on Neurology

Electronic supplementary material The online version of this article (<https://doi.org/10.1007/s00259-020-04788-w>) contains supplementary material, which is available to authorized users.

✉ Matthias Brendel
matthias.brendel@med.uni-muenchen.de

Extended author information available on the last page of the article

Introduction

Tauopathies consist of neurodegenerative diseases including, among others, Alzheimer's disease (AD), frontotemporal dementia and atypical parkinsonian syndromes such as progressive supranuclear palsy (PSP) and corticobasal syndrome (CBS), with the connective

characteristic of misfolded and accumulated tau protein in different parts of the brain [1, 2]. Visualization of tau deposits in vivo has become possible with various tau-targeting ligands for use with positron emission tomography (PET) [3, 4]. While first-generation tau tracers suffered from off-target binding [5, 6] and a resulting large inter- and intra-case variability [7], second-generation tau-PET tracers showed promising first results in vivo with specific binding in affected regions in patients with mild cognitive impairment and AD compared to healthy controls [8–11].

Tau-PET imaging complements an important biomarker for the characterization of neurodegenerative diseases. For AD, it has been proposed to classify the disease according to the biomarkers for amyloid, tau and neuronal injury by the A/T/N scheme [12]. In this classification scheme, neuronal injury in the pathological definition can be determined in vivo by three different diagnostic approaches. Atrophy in structural magnetic resonance tomography and total tau in cerebrospinal fluid are considered as well as hypometabolism in ^{18}F -fluorodeoxyglucose (^{18}F FDG)-PET. This is underpinned by a combined study in prion disease, indicating that metabolic imaging via ^{18}F FDG correlates with neuropathologic changes including neuronal loss [13].

For first-generation tau tracers and several tracers for amyloid-PET imaging, it has been shown that the perfusion-phase images as obtained by these tracers is comparable to glucose metabolism as assessed by ^{18}F FDG-PET and can therefore be used as surrogate biomarker of neuronal injury [14–21]. With respect to cost and radiation exposure, such “one-stop-shop” protocols have the opportunity to examine two important biological markers with one procedure.

In contrast to amyloid imaging where the subjects can only be classified as amyloid-positive or amyloid-negative, tau-PET imaging shows characteristic patterns for several different neurodegenerative entities [3]. Therefore, tau-PET imaging could probably also be used to discriminate a range of tauopathies beyond AD. Due to the lack of specificity of first-generation tau tracers, it is of great interest whether and how the perfusion-phase images as obtained by second-generation tracers can be used as a marker of neuronal injury.

Thus, we aimed to investigate the potential of the second-generation tau-PET ligand ^{18}F PI-2620 [22] as an additional (in addition to detecting tau pathology) biomarker of neuronal injury. We validated early-phase ^{18}F PI-2620 data against ^{18}F FDG-PET and focused on optimizing dynamic or coffee break acquisition protocols for tau-PET imaging with dual biomarker information.

Materials and methods

Study design and patient enrolment

Patients with different suspected tauopathies were referred by dementia or movement disorder experts to ^{18}F PI-2620 tau-PET imaging. We selected all subjects with an additional ^{18}F FDG-PET acquired < 12 months before/after tau-PET imaging. The cohort consisted of patients with different suspected clinical diagnoses and represented a true clinical cross-section in a tertiary centre with a focus on dementia/movement disorders. The most likely clinical differential diagnosis was recorded before ^{18}F PI-2620 tau-PET imaging. All patients provided informed written consent to PET imaging. The study was conducted in accordance with the principles of the Declaration of Helsinki, and approval for scientific data analysis was obtained from the local ethics committee (application number 17–569).

PET imaging

Radiosynthesis

Radiosynthesis of ^{18}F PI-2620 was achieved by nucleophilic substitution on a BOC-protected nitro precursor using an automated synthesis module (IBA, Synthera). The protecting group was cleaved under the radiolabelling conditions. The product was purified by semipreparative HPLC. Radiochemical purity was 99%. Non-decay corrected yields were about 35% with a molar activity of $8 \cdot 10^6$ GBq/mmol at the end of synthesis. ^{18}F FDG was purchased commercially.

PET acquisition and preparation

All patients were scanned at the Department of Nuclear Medicine, LMU Munich, with a Biograph 64 or a Siemens mCT PET/CT scanner (both Siemens, Erlangen, Germany). A low-dose CT scan preceded the PET acquisition and served for attenuation correction. ^{18}F PI-2620-PET was performed in a full dynamic 0–60-min setting initiated upon intravenous injection (~ 10 s) of 185 ± 10 MBq of the ligand. ^{18}F PI-2620-PET data were reconstructed in a series of 23 frames (6×0.5 min, 4×1.0 min, 4×2.0 min, 9×5.0 min). ^{18}F FDG-PET was acquired after injection of 125 ± 10 MBq ^{18}F FDG according to the EANM protocol [23]: fasting conditions > 6 h with a blood glucose < 120 mg/dl (6.7 mm) at time of scanning, silent room with dimmed light, headphones and blindfold 20 min prior and after injection. ^{18}F FDG-PET data were reconstructed in a static 30–50-min frame. PET data were reconstructed iteratively (4 iterations, 21 subsets, 5.0-mm Gauss/5 iterations, 24 subsets, 5.0-mm Gauss) with a matrix

size of $336 \times 336 \times 109 / 400 \times 400 \times 148$, a voxel size of $1.018 \times 1.018 \times 2.027 / 1.018 \times 1.018 \times 1.500 \text{ mm}^3$ and a slice thickness of $2.027 / 1.500 \text{ mm}$. Standard corrections with regard to scatter, decay and random counts were used. Both reconstruction algorithms resulted in images with equal spatial resolution ($8 \times 8 \times 7 \text{ mm}$) as validated by Hofmann phantom measures.

Image processing

All image data were processed and analysed using PMOD (version 3.5, PMOD Technologies Ltd., Zurich, Switzerland). For spatial normalization, tracer-specific templates in the MNI space were created for [^{18}F]PI-2620 (30–60 min) and [^{18}F]-FDG as described previously [14]. Dynamic [^{18}F]PI-2620 images were coregistered to the MNI space by applying the 30–60-min transformation (brain normalization settings: nonlinear warping, 8-mm input smoothing, equal modality, 16 iterations, frequency cut-off 3, regularization 1.0, no thresholding). All images were analysed in MNI space. The regional cerebral blood flow estimate R_1 was computed from the dynamic [^{18}F]PI-2620 images by applying the simplified reference tissue model 2 (SRTM2) as described previously [24, 25], using the cerebellum (excluding the dentate nucleus and superior layers) as a reference region. A total number of ten predefined cortical volumes (bilateral frontal, central region, parietal, temporal, occipital) of interests (VOIs) deriving from the Hammers atlas [26] were delineated in the MNI space and standardized uptake value ratios (SUVr) of all VOIs were extracted for the different images (and different time frames) used for the analysis.

In preparation for visual analyses of all images (after selection of the appropriate time frame), dynamic data frames #2–#5 (0.5–2.5 min) were summed. To account for the lower count statistics of the early-phase images, an additional 6.0-mm Gaussian filter was applied for both ([^{18}F]PI-2620_{0.5–2.5min} & [^{18}F]PI-2620_{R1}).

PET data evaluation

Correlation of single frames of [^{18}F]PI-2620-PET versus [^{18}F]FDG-PET

The optimal early time window for [^{18}F]PI-2620 early-phase imaging in terms of maximal correlation to [^{18}F]FDG-PET was determined. To this end, [^{18}F]PI-2620-PET SUVrs for the ten cortical VOIs were extracted and correlated with the SUVrs of the corresponding [^{18}F]FDG-PET data after normalization of uptake to global mean (GBM) or by use of a cerebellar reference region (CBL). Pearson's correlation coefficients (R) were compared between different time frames and

the selection of the optimal early-phase time window was based on the extent and significance of single frame agreement.

Regional comparison of optimized early-phase [^{18}F]PI-2620_{0.5–2.5min} and [^{18}F]PI-2620_{R1} versus [^{18}F]FDG

The SUVr values of the optimized summed [^{18}F]PI-2620 early-phase image (0.5–2.5 min), the [^{18}F]PI-2620 R_1 image and the [^{18}F]FDG image were correlated for all ten cortical regions to investigate the regional relationship between tau-PET perfusion and glucose metabolism.

Visual analysis of stereotactic surface projections

For visual interpretation of early-phase [^{18}F]PI-2620_{0.5–2.5min}, [^{18}F]PI-2620_{R1} and [^{18}F]FDG-PET images, three-dimensional stereotactic surface projections (3D-SSP) [27] were generated using the software Neurostat (Department of Radiology, University of Washington, Seattle, WA, USA). Voxel-wise Z-scores were calculated in Neurostat by comparing the individual tracer uptake ([^{18}F]PI-2620_{0.5–2.5min}, [^{18}F]PI-2620_{R1} and [^{18}F]FDG) to a historical [^{18}F]FDG-PET database (cognitively healthy individuals, age-matched, $N = 18$).

Three more experienced nuclear medicine physicians (H.B., T.v.E., M.B.) and three less experienced nuclear medicine interns (L.B., M.U., J.S.) visually assessed the 3D-SSP images using the Z-score maps (GBM scaling) and rated cortical regions used in the clinical routine (bilateral frontal, parietal, temporal, occipital cortex areas) from 0 to 3 (0 = no reduction, 1 = low reduction, 2 = intermediate reduction, 3 = severe reduction 0.5 steps were allowed). Furthermore, whole-brain 3D-SSP images were rated binary (0/1) and according to the severity of present neurodegeneration (0 = no/1 = mild/2 = intermediate/3 = severe neurodegeneration; 0.5 steps were allowed). A significant neuronal injury of the patient (A/T/N: N+) was defined by the majority read of binarized [^{18}F]FDG-PET evaluation by the three more experienced physicians. Readers had access to the pre-PET clinical diagnosis. All 3D-SSP images ([^{18}F]PI-2620_{0.5–2.5min}, [^{18}F]PI-2620_{R1} and [^{18}F]FDG) were randomly and blindly (with regard to the type of image) presented to the readers.

Statistical analysis

Correlations of regional SUVr between early-phase [^{18}F]PI-2620 and [^{18}F]FDG images were evaluated using Pearson's correlation coefficient (R) and R values were compared using Fisher's Z-transformation. Quantitative

Table 1 Demographics of the study population

	All	Most likely AD	Most likely 4R-tauopathy	Other
Number of subjects	26	7	13	6
Age (mean \pm SD)	66.0 \pm 10.7	67.4 \pm 9.1	70.7 \pm 6.8	54.2 \pm 11.6
Gender (♂/♀)	♂ 9/♀ 17	♂ 4/♀ 3	♂ 4/♀ 9	♂ 1/♀ 5
Time interval between PI-2620- and FDG-PET (months, mean \pm SD)	1.2 \pm 1.7	1.3 \pm 1.8	1.2 \pm 1.6	1.0 \pm 2.0
Significant neuronal injury [18 F]FDG (% visual)	65	71	77	33

AD, Alzheimer's disease; 4R, 4R-tauopathies (progressive supranuclear palsy, corticobasal syndrome); Other (frontotemporal dementia, multi-system atrophy, Parkinson's disease, unclear phenotype); SD, standard deviation. Significant neuronal injury in FDG-PET was defined by the majority read of more experienced readers

variables were reported as mean \pm standard deviation. Comparison of R values for different normalization approaches was also performed by Fisher's Z-transformation. For visual analysis and the specification of the most likely PET diagnosis, the intra-reader agreement between [18 F]PI-2620_{0.5–2.5min}, [18 F]PI-2620_{R1} and [18 F]FDG was calculated using Spearman's rank correlation coefficients. The disagreement between visual ratings of [18 F]PI-2620_{0.5–2.5min} or [18 F]PI-2620_{R1} and [18 F]FDG was calculated and evaluated as frequency of all brain regions. A significance level of $p < 0.05$ was applied in all analyses. All statistical analyses were performed using SPSS (version 25.0, IBM, Armonk, New York, USA).

Results

Demographics

A total of 26 subjects (age = 66 \pm 11 years, 17 female) were included in the analysis. The cohort consisted of seven subjects with a most likely diagnosis of AD, 13 subjects with movement disorders and most likely diagnosis of PSP or CBS, one case with most likely frontotemporal dementia, two cases with most likely multi-system atrophy, two cases with most likely Parkinson's disease, and one case with cognitive impairment of unknown reason. The mean time interval between both PET investigations was 1.2 \pm 1.7 months. For

Fig. 1 **a** Averaged (across all study subjects) time-activity curve of [18 F]PI-2620 in a cortical composite volume of interest during the dynamic data acquisition. **b** Correlation coefficients (R) between single frames of [18 F]PI-2620-PET and [18 F]FDG-PET (30–50 min p.i.). GBM, global mean scaling; CBL, cerebellar reference region. The time-window used for further analyses is highlighted in grey

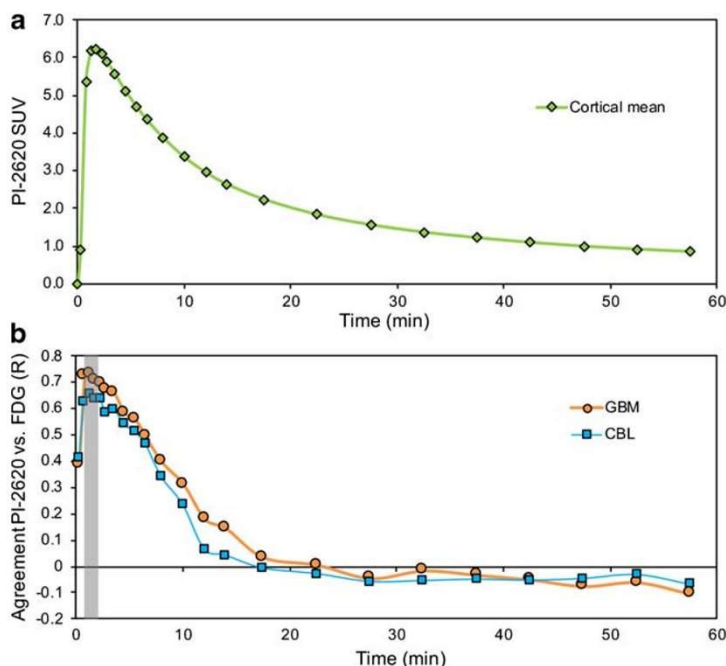


Table 2 Correlation coefficients between single frames of [¹⁸F]PI-2620-PET and [¹⁸F]FDG-PET

Time frames (min post-injection)	R	P _{max}	R	P _{max}
	Global mean normalization		Cerebellar normalization	
0–0.5	0.413	0.684	0.445	0.278
0.5–1.0	0.740	0.002**	0.650	0.036*
1.0–1.5	0.744	0.007**	0.679	0.019*
1.5–2.0	0.721	0.027*	0.665	0.021*
2.0–2.5	0.706	0.018*	0.667	0.041*
2.5–3.0	0.690	0.024*	0.610	0.073
3.0–4.0	0.677	0.042*	0.620	0.045*
4.0–5.0	0.599	0.071	0.550	0.225
5.0–6.0	0.573	0.225	0.519	0.086
6.0–7.0	0.506	0.520	0.452	0.140
7.0–9.0	0.405	0.493	0.309	0.294
9.0–11.0	0.322	0.692	0.184	0.954
11.0–13.0	0.190	0.984	−0.005	0.895
13.0–15.0	0.155	0.983	−0.018	0.995
15.0–20.0	0.040	0.968	−0.082	0.912
20.0–25.0	0.009	0.621	−0.110	0.875
25.0–30.0	−0.047	0.970	−0.149	0.873
30.0–35.0	−0.021	0.909	−0.137	0.961
35.0–40.0	−0.039	0.911	−0.136	0.850
40.0–45.0	−0.055	0.748	−0.144	0.702
45.0–50.0	−0.082	0.961	−0.139	0.937
50.0–55.0	−0.070	0.683	−0.126	0.983
55.0–60.0	−0.117	0.955	−0.162	0.804

FDG, fluorodeoxyglucose; R, correlation coefficient (Pearson, two-sided, Fisher's Z-transformation of all regions); p_{max}, maximum *p* value of all ten cortical regions. **p* < 0.05, ***p* < 0.01

details of the study population see Table 1. Visual binary interpretation (majority read of more experienced readers) revealed a significant neuronal injury to [¹⁸F]FDG-PET in 65% of all cases.

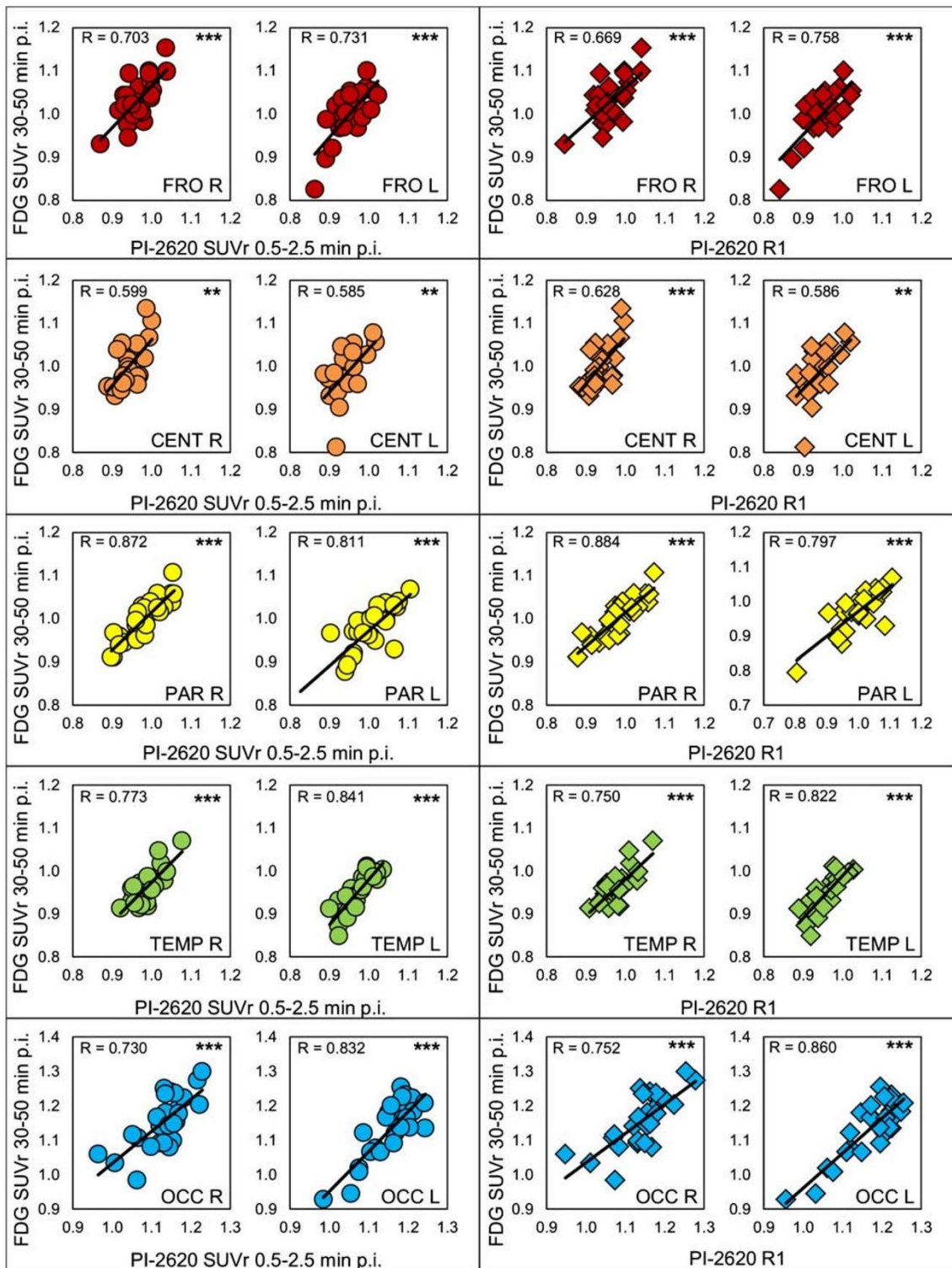
Optimal time window for [¹⁸F]PI-2620-PET early-phase imaging

The VOI-based comparison of single frames of [¹⁸F]PI-2620-PET (6 × 0.5 min, 4 × 1.0 min, 4 × 2 min, 9 × 5.0 min) and [¹⁸F]FDG-PET (30–50 min p.i.) revealed the highest agreement for the frames #2–#5 lasting from 0.5–2.5 min after injection for both global mean scaling ($R_{GBM} = 0.728$) and a cerebellar reference region ($R_{CBL} = 0.665$; Fig. 1). The correlation was statistically significant for all cortical regions for frames #2–#7 for global mean scaling (0.5–4 min after injection), but frames #6–#7 showed overall lower correlation coefficients compared to frames #2–#5 (especially with a cerebellar reference region). Because of the fast wash-out and sufficient count statistics for frames #2–#5, the mean values of the 0.5–2.5 min p.i. time window (frames #2–#5) were used for further semiquantitative and visual analyses. This was as they represented the optimal trade-off between correlation

with the [¹⁸F]FDG-PET data and count statistics. The correlation coefficients between the early [¹⁸F]PI-2620 and [¹⁸F]FDG-PET data and their degree of significance for all frames are shown in Table 2. The correlations coefficients between both normalization approaches were not significantly different (*p* = 0.301).

Semiquantitative VOI-based comparison of early-phase [¹⁸F]PI-2620-PET and [¹⁸F]FDG-PET

The PET parameters in all cortical brain regions showed highly significant correlations with [¹⁸F]FDG-PET for both early-phase [¹⁸F]PI-2620-PET approaches (0.5–2.5 min and R1). There was no significant difference in the correlation coefficients of [¹⁸F]PI-2620_{0.5–2.5min} and [¹⁸F]PI-2620_{R1} with [¹⁸F]FDG-PET ($R_{0.5–2.5min} = 0.762$, $R_{R1} = 0.766$, *p* = 0.487) for global mean normalization. The highest degree of correlation was found in the right parietal cortex ($R_{0.5–2.5min} = 0.872$, $R_{R1} = 0.884$) and the weakest correlation was observed in the left central region ($R_{0.5–2.5min} = 0.585$, $R_{R1} = 0.586$). The semiquantitative comparison of [¹⁸F]PI-2620_{0.5–2.5min} and [¹⁸F]PI-2620_{R1} with [¹⁸F]FDG-PET and cerebellar scaling also showed significant, but overall weaker correlations when



◀ **Fig. 2** Correlation charts of early-phase [^{18}F]PI-2620_{0.5–2.5min} and [^{18}F]PI-2620_{R1} with [^{18}F]FDG-PET SUVr (all global mean normalization). SUVr, standard-uptake-value-ratio; FRO, frontal; CENT, central; PAR, parietal; TEMP, temp; OCC, occipital

compared to global mean normalization for all cortical regions ($R_{0.5–2.5\text{min}} = 0.683$, $R_{R1} = 0.683$, $p = 0.472$). Correlation plots for [^{18}F]PI-2620_{0.5–2.5min} and [^{18}F]PI-2620_{R1} with [^{18}F]FDG-PET (all global mean normalization) are shown in Fig. 2. Corresponding regional values and correlation coefficients determined by comparing regional [^{18}F]PI-2620_{0.5–2.5min} and [^{18}F]PI-2620_{R1} with [^{18}F]FDG-PET SUVr (global mean and cerebellar normalization) are shown in Supplementary Table 1.

Visual 3D-SSP comparison of early-phase [^{18}F]PI-2620-PET and [^{18}F]FDG-PET

After identification of the optimal time window, visual assessment was performed by evaluating 3D-SSP images of early-phase ([^{18}F]PI-2620_{0.5–2.5min} and [^{18}F]PI-2620_{R1}) and [^{18}F]FDG-PET (global mean normalization). Representative images of early-phase [^{18}F]PI-2620_{0.5–2.5min}, [^{18}F]PI-2620_{R1} and [^{18}F]FDG-PET 3D-SSP and exemplary summed 0.5–2.5-min section images for three different most likely diagnoses of neurodegenerative disorders are shown in Fig. 3. In all cases, the regional pattern of hypoperfusion in [^{18}F]PI-2620_{0.5–2.5min} and [^{18}F]PI-2620_{R1} 3D-SSP resembled the hypometabolism pattern in [^{18}F]FDG-PET. Furthermore, exemplary distribution volume ratio images of those cases with the specific tau-PET binding pattern are shown in Supplementary Fig. 1.

Visual interpretation revealed moderate to high regional correlations for the majority of regions between early-phase tau-PET (both PI-2620_{0.5–2.5min} and PI-2620_{R1}) and [^{18}F]FDG-PET (see Table 3).

The frequency of no or only minor disagreement was far higher (0–0.5; 73–83%) when compared to the frequency of moderate (1.0–1.5; 17–25%) or high disagreement (≥ 2.0 ; 1–2%) regardless of using PI-2620_{0.5–2.5min} or PI-2620_{R1} for early-phase assessment (Fig. 4). Frequencies of disagreement were similar for more and less experienced readers (compare Fig. 4a, b).

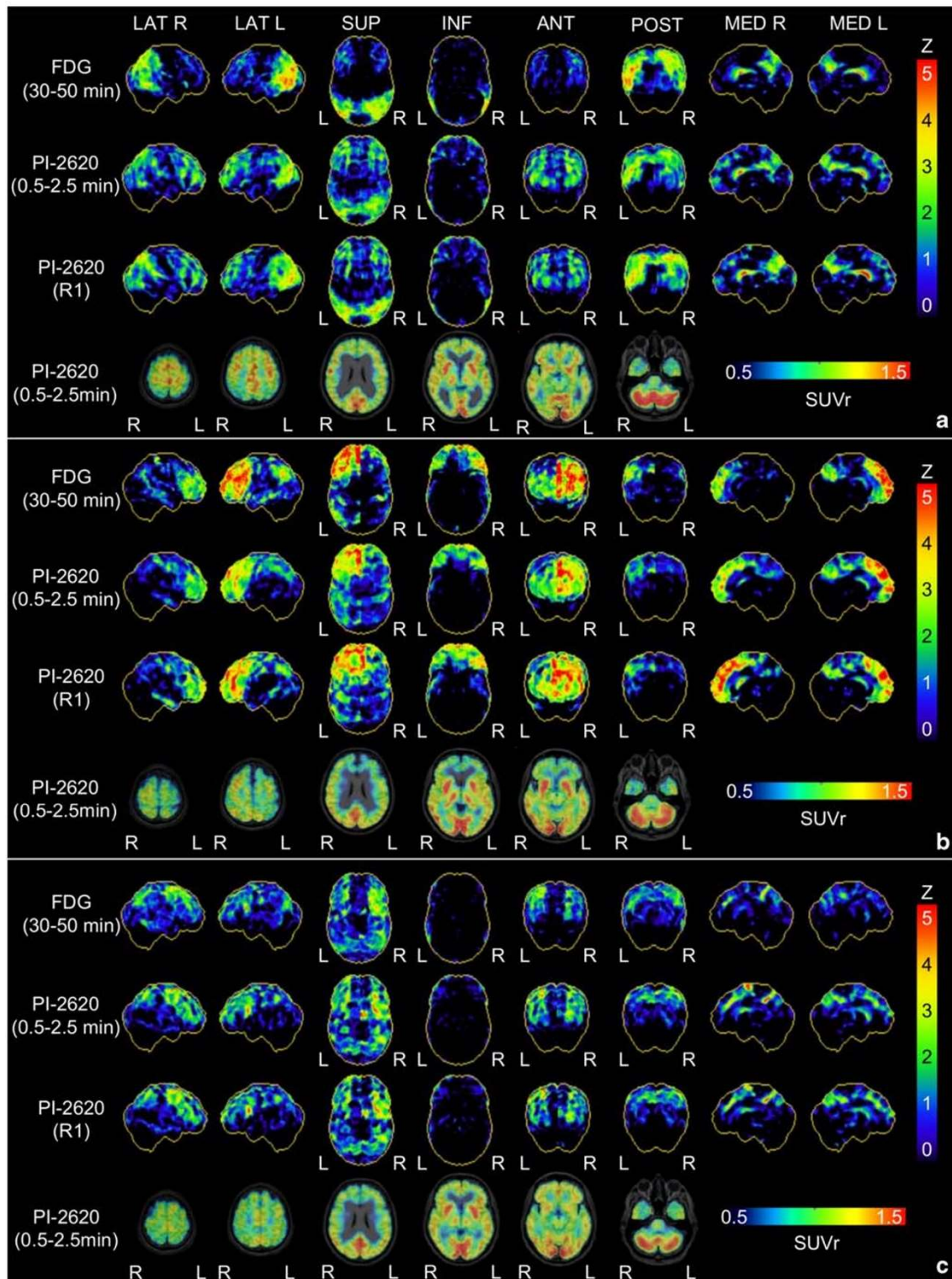
Discussion

Tau-PET imaging is of great interest as tauopathies make up the majority of neurodegenerative diseases [28]. However, not only information on tau-positivity but also on the presence of neuronal injury is considered in current diagnosis or research criteria of AD [12, 29] and non-AD tauopathies [30]. In accordance with previous amyloid-PET studies [14–18, 21], and considering the known limitations of first-generation tau

radiotracers [19, 31], we aimed to evaluate the potential of the early-phase of the second-generation tau-PET radiotracer [^{18}F]PI-2620 [11] as a potential surrogate biomarker of neuronal injury. Our results demonstrate a strong quantitative and visual agreement between reduced perfusion in tau-PET and reduced glucose metabolism in [^{18}F]FDG-PET imaging. Therefore, early-phase tau-PET images may potentially eliminate the need for an additional [^{18}F]FDG-PET. The ability to obtain two different biomarkers reduces costs, time and radiation exposure, and enables improved differential diagnosis through a one-stop-shop procedure, which is especially important for disabled patients.

The semiquantitative comparison of [^{18}F]PI-2620-PET single frames with individual [^{18}F]FDG-PET images revealed the highest agreement at 0.5–2.5 min after injection and decreased steadily until it was no longer significant for all cortical regions later than 4 min after injection. Previous studies evaluating the agreement between early-phase amyloid-PET acquisitions and [^{18}F]FDG-PET suggested time frames up to 10 min after injection, often sparing the first minute after injection [14, 15, 17]. Compared to these studies, we can conclude that the acquisition of early-phase [^{18}F]PI-2620 must include a very early and relatively short time frame to achieve a high agreement between tau-PET and [^{18}F]FDG-PET, likely related to the fast washout of [^{18}F]PI-2620 (Fig. 1a). Although the frames between 0.5 and 4.0 min p.i. indicated a significant correlation with [^{18}F]FDG-PET, we recommend the use of 0.5 to 2.5 min p.i. for early-phase [^{18}F]PI-2620 acquisition as this time window was more robust across different scaling methods. For implementation in study or clinical routine workflows, dynamic or coffee break protocols (included break between early- and late-image acquisitions with the possibility for the patient to rest) could be considered. In this regard, dynamic protocols will have the advantage of being able to perform non-invasive kinetic modelling for the tau-PET readout, which will be important to account for blood flow changes in longitudinal studies [32]. We also propose to exclude the first half minute of acquisition, which showed more variability, likely related to variance in blood flow (i.e., reduced cardiac ejection fraction), site of injection, and variance of manual injection. Therefore, we additionally calculated the regional cerebral blood flow estimate R_1 of [^{18}F]PI-2620 to take such individual differences into account and found similar results by this approach. The VOI-based semiquantitative regional correlation of both the summed early-phase (0.5–2.5 min) and R_1 of [^{18}F]PI-2620 showed a highly significant correlation in all assessed cortical regions and no significant advantage for one of the methods. For clinical implementation, the reconstruction of a summed image seems to be more suitable as it can be easily added to conventional reconstruction algorithms of common PET systems.

All semiquantitative analyses were performed with global mean normalization and whole cerebellum scaling. In



◀ **Fig. 3** Representative 3D-SSP images (Z-score maps) of [^{18}F]FDG-PET, early-phase [^{18}F]PI-2620_{0.5–2.5min} and [^{18}F]PI-2620_{R1} for three different most likely diagnoses of neurodegenerative disorders: **a** Alzheimer's disease, **b** frontotemporal dementia, **c** progressive supranuclear palsy (Richardson syndrome). Surface projections from R, right; L, left; LAT, lateral; SUP, superior; INF, inferior; ANT, anterior; POST, posterior; MED, medial

accordance with our previous investigation on early-phase amyloid-PET [14], the cerebellar normalization approach showed lower correlations for all investigated cortical regions. Since cerebellar perfusion tends to be highly variable, e.g., as a consequence of significant gender differences [33], a global mean normalization is likely superior to cerebellar scaling for interpretation of early-phase tau-PET images at the level of individual patients. Nevertheless, in subjects with an overall high load of neuronal injury or other reasons of a reduced whole brain perfusion (e.g., after ischemic stroke), the cerebellar scaling proved to be a viable alternative approach for normalization.

Based on the semiquantitative results, the visual analysis of summed [^{18}F]PI-2620 perfusion-like images was also performed with 3DSSP images generated by global mean normalization. Both tau-PET early-phase images (summed 0.5–2.5 min and R₁) showed an overall high visual agreement for the detection of neuronal injury with the corresponding metabolic imaging. Less and

more experienced nuclear medicine physicians had no or only minor disagreement between early-phase [^{18}F]PI-2620-PET and metabolic images in the majority of cases, indicating broad clinical applicability. Different patient preparation prior to injection of [^{18}F]FDG (eye patch and noise cancelling according to the EANM protocol [23]) and [^{18}F]PI-2620 (room noise, no eye patch) needs to be considered as a limitation.

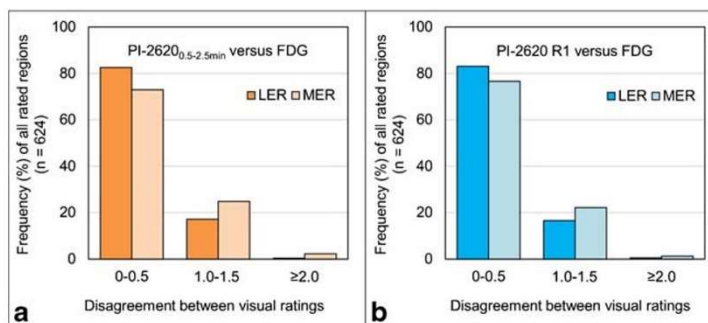
In our population of subjects referred with suspected tauopathies, half of all patients showed a significant neuronal injury pattern. This highlights the potential of this dual-phase protocol for evaluating two different biomarkers with one examination. While the detailed additive value of early-phase tau-PET imaging ultimately needs to be evaluated in larger samples, we already obtained promising results in individual cases. The patient with a final clinical diagnosis of frontotemporal dementia shown in Fig. 3 was initially referred with suspected AD, and the combination of tau-negativity together with a frontal hypoperfusion pattern was in line with the clinical presentation after 1-year follow-up. For the evaluation of perfusion-like images as a surrogate of neuronal injury, the comparison with metabolic imaging has the restriction that even a metabolic correlate might not unequivocally represent the actually existing neuronal injury. Temporary neuronal dysfunctions, for example, in the

Table 3 Spearman's rank correlation coefficients (ρ) between visual assessments of [^{18}F]FDG-PET and early-phase [^{18}F]PI-2620-PET; SUM, summed image 0.5–2.5 min after injection of [^{18}F]PI-2620; LER, less experienced reader; MER, more experienced reader; R, right; L, left; ND, neurodegeneration

	LER1	LER2	LER3	MER1	MER2	MER3
FDG versus SUM	ρ	ρ	ρ	ρ	ρ	ρ
Likelihood of ND	0.661**	0.159	0.335	0.545**	0.404*	0.405*
Frontal R	0.666**	0.579**	0.407*	0.491*	0.403*	0.306
Frontal L	0.738**	0.576**	0.482*	0.550**	0.568**	0.525**
Parietal R	0.876**	0.641**	0.323	0.612**	0.398*	0.803**
Parietal L	0.717**	0.725**	0.478*	0.531**	0.359	0.659**
Temporal R	0.454*	0.517**	0.470*	0.677**	0.294	0.239
Temporal L	0.634**	0.399*	0.658**	0.566**	0.565**	0.321
Occipital R	−0.097	0.385	0.587**	0.676**	0.074	0.692**
Occipital L	0.280	0.476*	0.566**	0.852**	0.554**	0.557**
FDG versus R1	ρ	ρ	ρ	ρ	ρ	ρ
Likelihood of ND	0.541**	0.267	0.526**	0.634**	0.598**	0.593**
Frontal R	0.366	0.447*	0.258	0.432*	0.255	0.326
Frontal L	0.732**	0.576**	0.600**	0.598**	0.558**	0.401*
Parietal R	0.756**	0.726**	0.614**	0.674**	0.508**	0.742**
Parietal L	0.617**	0.714**	0.724**	0.554**	0.654**	0.560**
Temporal R	0.577**	0.493	0.371	0.367	0.337	0.588**
Temporal L	0.670**	0.454*	0.706**	0.557**	0.747**	0.537**
Occipital R	−0.097	0.180	−0.002	0.820**	0.286	0.731**
Occipital L	0.345	0.509**	0.598**	0.801**	0.684**	0.728**

* $p < 0.05$, ** $p < 0.01$

Fig. 4 Disagreement between visual rating of early-phase a [^{18}F]PI-2620_{0.5–2.5min} and b [^{18}F]PI-2620_{R1} 3D-SSP images in contrast to visual rating of [^{18}F]FDG-PET 3D-SSP images for all evaluated brain regions of all cases ($n = 624$). Less experienced (LER) and more experienced (MER) readers are displayed separately



context of a diaschisis or neuroinflammation, cannot be differentiated from the presence of neuronal damage.

Both reduced metabolism in [^{18}F]FDG-PET and reduced perfusion in perfusion-phase images of different radiotracers are influenced and partially caused by partial volume effects and might not purely reflect the underlying neuronal injury. Nevertheless, a close correlation with atrophy in magnetic resonance imaging [34] or neuropathology findings [13] was demonstrated for metabolic imaging via [^{18}F]FDG. Therefore, most classification schemes, such as ATN [12], list [^{18}F]FDG-PET as a surrogate of neuronal injury together with atrophy in structural magnetic resonance imaging and total tau in cerebrospinal fluid. Our findings clearly demonstrate that dual-phase [^{18}F]PI-2620-PET cannot only provide information on “T” [22] but has also the potential to facilitate assessment of “N”.

Conclusions

The present study demonstrates that early-phase imaging of second-generation [^{18}F]PI-2620 tau-PET can serve as a surrogate biomarker for neuronal injury as it shows excellent semi-quantitative and visual agreement with metabolic imaging using [^{18}F]FDG-PET. Dynamic imaging or a dual time-point protocol for tau-PET could replace additional [^{18}F]FDG-PET imaging by indexing two biomarkers in neurodegenerative disease, the distribution of tau and the amount and regional pattern of neuronal injury. The short time required for recording perfusion-like images is a great advantage in terms of patient comfort, examination time, radiation safety and cost-effectiveness.

Acknowledgements The authors thank the staff of the departments of nuclear medicine and neurology at the University Hospital LMU Munich. We thank the patients and their families.

Funding information Open Access funding provided by Projekt DEAL. C.P. received research funding from Lüneburg heritage. M.T.B. received research funding from the Felgenhauer-Stiftung, Forschungspool Klinische Studien (University of Cologne), H2020, Medtronic and Boston Scientific. G.U.H. was funded by the Deutsche Forschungsgemeinschaft (DFG) under Germany’s Excellence Strategy within the framework of the Munich Cluster for Systems Neurology (EXC 2145 SyNergy—ID 390857198), the German Federal Ministry of Education and Research (BMBF, 01EK1605A HitTau), the NOMIS foundation (FTLD project), and received research support from GE Healthcare and Neuropore.

Compliance with ethical standards

Conflict of interest M.B. received speaker honoraria from GE healthcare and LMI and is an advisor of LMI. M.T.B. received speaker’s honoraria from Medtronic, Boston Scientific, Abbott (formerly St. Jude), GE Medical, UCB and Bial. G.U.H. has ongoing research collaborations with Orion and Prothena; serves as a consultant for AbbVie, AlzProtect, Asceneuron, Biogen, Biohaven, Lundbeck, Novartis, Roche, Sanofi, UCB; received honoraria for scientific presentations from AbbVie, Biogen, Roche, Teva, UCB, and Zambon; and holds a patent on PERK Activation for the Treatment of Neurodegenerative Diseases (PCT/EP2015/068734). All other authors declare that they have no conflict of interest.

Ethical approval All procedures performed in studies involving human participants were in accordance with the ethical standards of the institutional and/or national research committee (LMU Munich—application number 17–569) and with the 1964 Helsinki declaration and its later amendments or comparable ethical standards.

Informed consent Informed consent was obtained from all patients. All patients provided informed written consent to PET imaging. The study was conducted in accordance with the principles of the Declaration of Helsinki, and approval for scientific data analysis was obtained from the local ethics committee (application number 17–569).

Open Access This article is licensed under a Creative Commons Attribution 4.0 International License, which permits use, sharing, adaptation, distribution and reproduction in any medium or format, as long as you give appropriate credit to the original author(s) and the source, provide a link to the Creative Commons licence, and indicate if changes were made. The images or other third party material in this article are included in the article’s Creative Commons licence, unless indicated

otherwise in a credit line to the material. If material is not included in the article's Creative Commons licence and your intended use is not permitted by statutory regulation or exceeds the permitted use, you will need to obtain permission directly from the copyright holder. To view a copy of this licence, visit <http://creativecommons.org/licenses/by/4.0/>.

References

- Arendt T, Stieler JT, Holzer M. Tau and tauopathies. *Brain Res Bull*. 2016;126:238–92. <https://doi.org/10.1016/j.brainresbull.2016.08.018>.
- Rosler TW, Tayaranian Marvian A, Brendel M, Nykanen NP, Hollerhage M, Schwarz SC, et al. Four-repeat tauopathies. *Prog Neurobiol*. 2019;101644. <https://doi.org/10.1016/j.pneurobio.2019.101644>.
- Villemagne VL, Okamura N. In vivo tau imaging: obstacles and progress. *Alzheimers Dement*. 2014;10:S254–64. <https://doi.org/10.1016/j.jalz.2014.04.013>.
- Robertson JS, Rowe CC, Villemagne VL. Tau imaging with PET: an overview of challenges, current progress, and future applications. *Quarterly J Nuclear Med Molec Imag*. 2017;61:405–13. <https://doi.org/10.23736/s1824-4785.17.03012-6>.
- Lemoine L, Leuzy A, Chiotis K, Rodriguez-Vieitez E, Nordberg A. Tau positron emission tomography imaging in tauopathies: the added hurdle of off-target binding. *Alzheimers Dement (Amsterdam, Netherlands)*. 2018;10:232–6. <https://doi.org/10.1016/j.dadm.2018.01.007>.
- Chiotis K, Stenkrona P, Almkvist O, Stepanov V, Ferreira D, Arakawa R, et al. Dual tracer tau PET imaging reveals different molecular targets for (11)C-THK5351 and (11)C-PBB3 in the Alzheimer brain. *Eur J Nucl Med Mol Imaging*. 2018;45:1605–17. <https://doi.org/10.1007/s00259-018-4012-5>.
- Wren MC, Lashley T, Arstad E, Sander K. Large inter- and intrase variability of first generation tau PET ligand binding in neurodegenerative dementias. *Acta Neuropathol Commun*. 2018;6:34. <https://doi.org/10.1186/s40478-018-0535-z>.
- Lohith TG, Bennacef I, Vandenbergh R, Vandenbulcke M, Salinas CA, Declercq R, et al. Brain imaging of Alzheimer dementia patients and elderly controls with (18)F-MK-6240, a PET tracer targeting neurofibrillary tangles. *J Nucl Med*. 2019;60:107–14. <https://doi.org/10.2967/jnumed.118.208215>.
- Bethausser TJ, Cody KA, Zammit MD, Murali D, Converse AK, Barnhart TE, et al. In vivo characterization and quantification of neurofibrillary tau PET radioligand (18)F-MK-6240 in humans from Alzheimer disease dementia to young controls. *J Nucl Med*. 2019;60:93–9. <https://doi.org/10.2967/jnumed.118.209650>.
- Wong DF, Comley RA, Kuwabara H, Rosenberg PB, Resnick SM, Ostrowitzki S, et al. Characterization of 3 novel tau radiopharmaceuticals, (11)C-RO-963, (11)C-RO-643, and (18)F-RO-948, in healthy controls and in Alzheimer subjects. *J Nucl Med*. 2018;59:1869–76. <https://doi.org/10.2967/jnumed.118.209916>.
- Kroth H, Oden F, Molette J, Schieferstein H, Capotosti F, Mueller A, et al. Discovery and preclinical characterization of [(18)F]PI-2620, a next-generation tau PET tracer for the assessment of tau pathology in Alzheimer's disease and other tauopathies. *Eur J Nucl Med Mol Imaging*. 2019;46:2178–89. <https://doi.org/10.1007/s00259-019-04397-2>.
- Jack CR Jr, Bennett DA, Blennow K, Carrillo MC, Feldman HH, Frisoni GB, et al. A/T/N: an unbiased descriptive classification scheme for Alzheimer disease biomarkers. *Neurology*. 2016;87:539–47. <https://doi.org/10.1212/wnl.0000000000002923>.
- Mente KP, O'Donnell JK, Jones SE, Cohen ML, Thompson NR, Bizzi A, et al. Fluorodeoxyglucose positron emission tomography (FDG-PET) correlation of histopathology and MRI in prion disease. *Alzheimer Dis Assoc Disord*. 2017;31:1–7. <https://doi.org/10.1097/wad.000000000000188>.
- Daerr S, Brendel M, Zach C, Mille E, Schilling D, Zacherl MJ, et al. Evaluation of early-phase [(18)F]-florbetaben PET acquisition in clinical routine cases. *Neuroimage Clin*. 2017;14:77–86. <https://doi.org/10.1016/j.nicl.2016.10.005>.
- Hsiao IT, Huang CC, Hsieh CJ, Hsu WC, Wey SP, Yen TC, et al. Correlation of early-phase 18F-florbetapir (AV-45/Amyvid) PET images to FDG images: preliminary studies. *Eur J Nucl Med Mol Imaging*. 2012;39:613–20. <https://doi.org/10.1007/s00259-011-2051-2>.
- Florek L, Tiepolt S, Schroeter ML, Berrouschot J, Saur D, Hesse S, et al. Dual time-point [18F]florbetaben PET delivers dual biomarker information in mild cognitive impairment and Alzheimer's disease. *J Alzheimers Dis*. 2018;66:1105–16. <https://doi.org/10.3233/jad-180522>.
- Tiepolt S, Hesse S, Patt M, Luthardt J, Schroeter ML, Hoffmann KT, et al. Early [(18)F]florbetaben and [(11)C]PIB PET images are a surrogate biomarker of neuronal injury in Alzheimer's disease. *Eur J Nucl Med Mol Imaging*. 2016;43:1700–9. <https://doi.org/10.1007/s00259-016-3353-1>.
- Meyer PT, Hellwig S, Amtage F, Rottenburger C, Sahn U, Reuland P, et al. Dual-biomarker imaging of regional cerebral amyloid load and neuronal activity in dementia with PET and 11C-labeled Pittsburgh compound B. *J Nucl Med*. 2011;52:393–400. <https://doi.org/10.2967/jnumed.110.083683>.
- Brendel M, Wagner L, Levin J, Zach C, Lindner S, Bartenstein P, et al. Perfusion-phase [(18)F]THK5351 tau-PET imaging as a surrogate marker for neurodegeneration. *J Alzheimers Dis Rep*. 2017;1:109–13. <https://doi.org/10.3233/adr-170023>.
- Rodriguez-Vieitez E, Leuzy A, Chiotis K, Saint-Aubert L, Wall A, Nordberg A. Comparability of [(18)F]THK5317 and [(11)C]PIB blood flow proxy images with [(18)F]FDG positron emission tomography in Alzheimer's disease. *J Cereb Blood Flow Metab*. 2017;37:740–9. <https://doi.org/10.1177/0271678x16645593>.
- Rostomian AH, Madison C, Rabinovici GD, Jagust WJ. Early 11C-PIB frames and 18F-FDG PET measures are comparable: a study validated in a cohort of AD and FTL D patients. *J Nucl Med*. 2011;52:173–9. <https://doi.org/10.2967/jnumed.110.082057>.
- Mueller A, Bullich S, Barret O, Madonia J, Berndt M, Papin C, et al. Tau PET imaging with (18)F-PI-2620 in patients with Alzheimer's disease and healthy controls: a first-in-human study. *J Nucl Med*. 2019. <https://doi.org/10.2967/jnumed.119.236224>.
- Varrone A, Asenbaum S, Vander Borght T, Booi J, Nobili F, Nagren K, et al. EANM procedure guidelines for PET brain imaging using [18F]FDG, version 2. *Eur J Nucl Med Mol Imaging*. 2009;36:2103–10. <https://doi.org/10.1007/s00259-009-1264-0>.
- Lammertsma AA, Hume SP. Simplified reference tissue model for PET receptor studies. *NeuroImage*. 1996;4:153–8. <https://doi.org/10.1006/nimg.1996.0066>.
- Wu Y, Carson RE. Noise reduction in the simplified reference tissue model for neuroreceptor functional imaging. *J Cereb Blood Flow Metab*. 2002;22:1440–52. <https://doi.org/10.1097/01.WCB.0000033967.83623.34>.
- Hammers A, Allom R, Koepp MJ, Free SL, Myers R, Lemieux L, et al. Three-dimensional maximum probability atlas of the human brain, with particular reference to the temporal lobe. *Hum Brain Mapp*. 2003;19:224–47. <https://doi.org/10.1002/hbm.10123>.
- Minoshima S, Frey KA, Koeppe RA, Foster NL, Kuhl DE. A diagnostic approach in Alzheimer's disease using three-dimensional stereotactic surface projections of fluorine-18-FDG PET. *J Nucl Med*. 1995;36:1238–48.
- Erkkinen MG, Kim MO, Geschwind MD. Clinical neurology and epidemiology of the major neurodegenerative diseases. *Cold Spring Harb Perspect Biol*. 2018;10. <https://doi.org/10.1101/cshperspect.a033118>.
- Jack CR Jr, Bennett DA, Blennow K, Carrillo MC, Dunn B, Haeberlein SB, et al. NIA-AA research framework: toward a

- biological definition of Alzheimer's disease. *Alzheimers Dement.* 2018;14:535–62. <https://doi.org/10.1016/j.jalz.2018.02.018>.
30. Hoglinger GU, Respondek G, Stamelou M, Kurz C, Josephs KA, Lang AE, et al. Clinical diagnosis of progressive supranuclear palsy: the movement disorder society criteria. *Mov Disord.* 2017;32:853–64. <https://doi.org/10.1002/mds.26987>.
31. Ng KP, Pascoal TA, Mathotaarachchi S, Therriault J, Kang MS, Shin M, et al. Monoamine oxidase B inhibitor, selegiline, reduces 18F-THK5351 uptake in the human brain. *Alzheimers Res Ther.* 2017;9:25. <https://doi.org/10.1186/s13195-017-0253-y>.
32. van Berckel BN, Ossenkoppele R, Tolboom N, Yaqub M, Foster-Dingley JC, Windhorst AD, et al. Longitudinal amyloid imaging using 11C-PiB: methodologic considerations. *J Nucl Med.* 2013;54:1570–6. <https://doi.org/10.2967/jnumed.112.113654>.
33. Amen DG, Trujillo M, Keator D, Taylor DV, Willeumier K, Meysami S, et al. Gender-based cerebral perfusion differences in 46,034 functional neuroimaging scans. *J Alzheimers Dis.* 2017;60:605–14. <https://doi.org/10.3233/jad-170432>.
34. Alvarez-Linera Prado J, Jimenez-Huete A. Neuroimaging in dementia. *Clin Radiol Correlat Radiol.* 2019;61:66–81. <https://doi.org/10.1016/j.rx.2018.08.004>.

Publisher's note Springer Nature remains neutral with regard to jurisdictional claims in published maps and institutional affiliations.

Affiliations

Leonie Beyer¹ · Alexander Nitschmann¹ · Henryk Barthel² · Thilo van Eimeren^{3,4,5,6} · Marcus Unterrainer¹ · Julia Sauerbeck¹ · Ken Marek^{7,8} · Mengmeng Song¹ · Carla Palleis⁹ · Gesine Respondek^{9,10} · Jochen Hammes⁴ · Michael T. Barbe⁵ · Özgür Onur⁵ · Frank Jessen^{6,11,12} · Dorothee Saur¹³ · Matthias L. Schroeter^{14,15,16} · Jost-Julian Rumpf¹² · Michael Rullmann² · Andreas Schildan² · Marianne Patt² · Bernd Neumaier^{17,18} · Olivier Barret^{7,8} · Jennifer Madonia^{7,8} · David S. Russell^{7,8} · Andrew W. Stephens¹⁹ · Sigrun Roeber²⁰ · Jochen Herms^{10,20} · Kai Bötzel⁹ · Johannes Levin^{9,10} · Joseph Classen¹³ · Günter U. Höglinger^{10,21,22} · Peter Bartenstein^{1,23} · Victor Villemagne^{24,25,26} · Alexander Drzezga^{4,6} · John Seibyl^{7,8} · Osama Sabri² · Matthias Brendel^{1,23}

¹ Department of Nuclear Medicine, University Hospital of Munich LMU Munich, Marchioninstraße 15, 81377 Munich, Germany

² Department of Nuclear Medicine, University of Leipzig, Leipzig, Germany

³ Cognitive Neuroscience, Institute for Neuroscience and Medicine (INM-3), Research Centre Juelich, Juelich, Germany

⁴ Department of Nuclear Medicine, University Hospital Cologne, Cologne, Germany

⁵ Department of Neurology, University of Cologne, Faculty of Medicine and University Hospital Cologne, Cologne, Germany

⁶ German Center for Neurodegenerative Diseases (DZNE), Bonn, Germany

⁷ InviCRO, LLC, Boston, MA, USA

⁸ Molecular Neuroimaging, inviCRO, New Haven, CT, USA

⁹ Department of Neurology, University Hospital of Munich, LMU Munich, Munich, Germany

¹⁰ German Center for Neurodegenerative Diseases (DZNE), Munich, Germany

¹¹ Department of Psychiatry, University Hospital Cologne, Cologne, Germany

¹² Center for Memory Disorders, University Hospital Cologne, Cologne, Germany

¹³ Department of Neurology, University of Leipzig Medical Center, Leipzig, Germany

¹⁴ Clinic for Cognitive Neurology, University of Leipzig, Leipzig, Germany

¹⁵ LIFE - Leipzig Research Center for Civilization Diseases, University of Leipzig, Leipzig, Germany

¹⁶ Max-Planck-Institute of Human Cognitive and Brain Sciences, Leipzig, Germany

¹⁷ Institute of Neuroscience and Medicine, Nuclear Chemistry (INM-5), Forschungszentrum Juelich GmbH, Juelich, Germany

¹⁸ Institute of Radiochemistry and Experimental Molecular Imaging, University Clinic Cologne, Cologne, Germany

¹⁹ Life Molecular Imaging GmbH, Berlin, Germany

²⁰ Center for Neuropathology and Prion Research, University Hospital of Munich, LMU Munich, Munich, Germany

²¹ Department of Neurology, Technische Universität München, Munich, Germany

²² Department of Neurology, Hannover Medical School, Hannover, Germany

²³ Munich Cluster for Systems Neurology (SyNergy), Munich, Germany

²⁴ Department of Molecular Imaging & Therapy, Austin Health, Heidelberg, VIC, Australia

²⁵ The Florey Institute of Neuroscience and Mental Health, The University of Melbourne, Melbourne, VIC, Australia

²⁶ Department of Medicine, Austin Health, The University of Melbourne, Melbourne, VIC, Australia

References

1. Kovacs, G.G., *Concepts and classification of neurodegenerative diseases*. *Handb Clin Neurol*, 2017. **145**: p. 301-307.
2. Forman, M.S., J.Q. Trojanowski, and V.M. Lee, *Neurodegenerative diseases: a decade of discoveries paves the way for therapeutic breakthroughs*. *Nat Med*, 2004. **10**(10): p. 1055-63.
3. Dugger, B.N. and D.W. Dickson, *Pathology of Neurodegenerative Diseases*. Cold Spring Harb Perspect Biol, 2017. **9**(7).
4. Kovacs, G., *Current Concepts of Neurodegenerative Diseases*. *Eur Med J Neurol*, 2014. **1**: p. 78-86.
5. Kovacs, G.G. and H. Budka, *Current concepts of neuropathological diagnostics in practice: neurodegenerative diseases*. *Clin Neuropathol*, 2010. **29**(5): p. 271-88.
6. Lee, V.M., M. Goedert, and J.Q. Trojanowski, *Neurodegenerative tauopathies*. *Annu Rev Neurosci*, 2001. **24**: p. 1121-59.
7. Dickson, D.W., et al., *Neuropathology of frontotemporal lobar degeneration-tau (FTLD-tau)*. *J Mol Neurosci*, 2011. **45**(3): p. 384-9.
8. Spillantini, M.G. and M. Goedert, *Tau pathology and neurodegeneration*. *Lancet Neurol*, 2013. **12**(6): p. 609-22.
9. Kovacs, G.G., *Invited review: Neuropathology of tauopathies: principles and practice*. *Neuropathol Appl Neurobiol*, 2015. **41**(1): p. 3-23.
10. Scholl, M., et al., *Biomarkers for tau pathology*. *Mol Cell Neurosci*, 2019. **97**: p. 18-33.
11. Rosler, T.W., et al., *Four-repeat tauopathies*. *Prog Neurobiol*, 2019. **180**: p. 101644.
12. Arendt, T., J.T. Stieler, and M. Holzer, *Tau and tauopathies*. *Brain Res Bull*, 2016. **126**(Pt 3): p. 238-292.
13. Espinoza, M., et al., *Differential incorporation of tau isoforms in Alzheimer's disease*. *J Alzheimers Dis*, 2008. **14**(1): p. 1-16.
14. Holtzman, D.M., J.C. Morris, and A.M. Goate, *Alzheimer's disease: the challenge of the second century*. *Sci Transl Med*, 2011. **3**(77): p. 77sr1.
15. Rossi, G., et al., *Different mutations at V363 MAPT codon are associated with atypical clinical phenotypes and show unusual structural and functional features*. *Neurobiol Aging*, 2014. **35**(2): p. 408-17.
16. Goedert, M., *Tau filaments in neurodegenerative diseases*. *FEBS Lett*, 2018. **592**(14): p. 2383-2391.
17. Trojanowski, J.Q., et al., *Distribution of tau proteins in the normal human central and peripheral nervous system*. *J Histochem Cytochem*, 1989. **37**(2): p. 209-15.
18. Cleveland, D.W., S.Y. Hwo, and M.W. Kirschner, *Physical and chemical properties of purified tau factor and the role of tau in microtubule assembly*. *J Mol Biol*, 1977. **116**(2): p. 227-47.
19. Cleveland, D.W., S.Y. Hwo, and M.W. Kirschner, *Purification of tau, a microtubule-associated protein that induces assembly of microtubules from purified tubulin*. *J Mol Biol*, 1977. **116**(2): p. 207-25.

20. Weingarten, M.D., et al., *A protein factor essential for microtubule assembly*. Proc Natl Acad Sci U S A, 1975. **72**(5): p. 1858-62.
21. Goedert, M., et al., *Multiple isoforms of human microtubule-associated protein tau: sequences and localization in neurofibrillary tangles of Alzheimer's disease*. Neuron, 1989. **3**(4): p. 519-26.
22. Andreadis, A., *Tau gene alternative splicing: expression patterns, regulation and modulation of function in normal brain and neurodegenerative diseases*. Biochim Biophys Acta, 2005. **1739**(2-3): p. 91-103.
23. Goedert, M., et al., *Cloning and sequencing of the cDNA encoding an isoform of microtubule-associated protein tau containing four tandem repeats: differential expression of tau protein mRNAs in human brain*. EMBO J, 1989. **8**(2): p. 393-9.
24. Goedert, M. and R. Jakes, *Expression of separate isoforms of human tau protein: correlation with the tau pattern in brain and effects on tubulin polymerization*. EMBO J, 1990. **9**(13): p. 4225-30.
25. Wang, Y.T. and P. Edison, *Tau Imaging in Neurodegenerative Diseases Using Positron Emission Tomography*. Curr Neurol Neurosci Rep, 2019. **19**(7): p. 45.
26. Okamura, N., et al., *The development and validation of tau PET tracers: current status and future directions*. Clin Transl Imaging, 2018. **6**(4): p. 305-316.
27. Siddiqua, A. and M. Margittai, *Three- and four-repeat Tau coassemble into heterogeneous filaments: an implication for Alzheimer disease*. J Biol Chem, 2010. **285**(48): p. 37920-6.
28. Butner, K.A. and M.W. Kirschner, *Tau protein binds to microtubules through a flexible array of distributed weak sites*. J Cell Biol, 1991. **115**(3): p. 717-30.
29. Goode, B.L. and S.C. Feinstein, *Identification of a novel microtubule binding and assembly domain in the developmentally regulated inter-repeat region of tau*. J Cell Biol, 1994. **124**(5): p. 769-82.
30. Buee, L., et al., *Tau protein isoforms, phosphorylation and role in neurodegenerative disorders*. Brain Res Brain Res Rev, 2000. **33**(1): p. 95-130.
31. Park, S.A., S.I. Ahn, and J.M. Gallo, *Tau mis-splicing in the pathogenesis of neurodegenerative disorders*. BMB Rep, 2016. **49**(8): p. 405-13.
32. Jeganathan, S., et al., *Global hairpin folding of tau in solution*. Biochemistry, 2006. **45**(7): p. 2283-93.
33. Iqbal, K., F. Liu, and C.X. Gong, *Tau and neurodegenerative disease: the story so far*. Nat Rev Neurol, 2016. **12**(1): p. 15-27.
34. Maas, T., J. Eidenmuller, and R. Brandt, *Interaction of tau with the neural membrane cortex is regulated by phosphorylation at sites that are modified in paired helical filaments*. J Biol Chem, 2000. **275**(21): p. 15733-40.
35. Arima, K., *Ultrastructural characteristics of tau filaments in tauopathies: immuno-electron microscopic demonstration of tau filaments in tauopathies*. Neuropathology, 2006. **26**(5): p. 475-83.
36. Buee, L. and A. Delacourte, *Comparative biochemistry of tau in progressive supranuclear palsy, corticobasal degeneration, FTDP-17 and Pick's disease*. Brain Pathol, 1999. **9**(4): p. 681-93.
37. Josephs, K.A., *Current Understanding of Neurodegenerative Diseases Associated With the Protein Tau*. Mayo Clin Proc, 2017. **92**(8): p. 1291-1303.

38. Crary, J.F., et al., *Primary age-related tauopathy (PART): a common pathology associated with human aging*. Acta Neuropathol, 2014. **128**(6): p. 755-66.
39. Goedert, M. and M.G. Spillantini, *A century of Alzheimer's disease*. Science, 2006. **314**(5800): p. 777-81.
40. Braak, H. and E. Braak, *Neuropathological stageing of Alzheimer-related changes*. Acta Neuropathol, 1991. **82**(4): p. 239-59.
41. Masters, C.L., et al., *Amyloid plaque core protein in Alzheimer disease and Down syndrome*. Proc Natl Acad Sci U S A, 1985. **82**(12): p. 4245-9.
42. Grundke-Iqbal, I., et al., *Microtubule-associated protein tau. A component of Alzheimer paired helical filaments*. J Biol Chem, 1986. **261**(13): p. 6084-9.
43. Hardy, J., et al., *Genetic dissection of Alzheimer's disease and related dementias: amyloid and its relationship to tau*. Nat Neurosci, 1998. **1**(5): p. 355-8.
44. Selkoe, D.J. and J. Hardy, *The amyloid hypothesis of Alzheimer's disease at 25 years*. EMBO Mol Med, 2016. **8**(6): p. 595-608.
45. Iqbal, K., et al., *Tau in Alzheimer disease and related tauopathies*. Curr Alzheimer Res, 2010. **7**(8): p. 656-64.
46. Thal, D.R., J. Attems, and M. Ewers, *Spreading of amyloid, tau, and microvascular pathology in Alzheimer's disease: findings from neuropathological and neuroimaging studies*. J Alzheimers Dis, 2014. **42 Suppl 4**: p. S421-9.
47. Goedert, M., A. Klug, and R.A. Crowther, *Tau protein, the paired helical filament and Alzheimer's disease*. J Alzheimers Dis, 2006. **9**(3 Suppl): p. 195-207.
48. Braak, H., et al., *Stages of the pathologic process in Alzheimer disease: age categories from 1 to 100 years*. J Neuropathol Exp Neurol, 2011. **70**(11): p. 960-9.
49. Coakeley, S., et al., *Positron emission tomography imaging of tau pathology in progressive supranuclear palsy*. J Cereb Blood Flow Metab, 2017. **37**(9): p. 3150-3160.
50. Liscic, R.M., et al., *Differentiation of progressive supranuclear palsy: clinical, imaging and laboratory tools*. Acta Neurol Scand, 2013. **127**(5): p. 362-70.
51. Dickson, D.W., *Neuropathologic differentiation of progressive supranuclear palsy and corticobasal degeneration*. J Neurol, 1999. **246 Suppl 2**: p. 116-15.
52. Grijalvo-Perez, A.M. and I. Litvan, *Corticobasal degeneration*. Semin Neurol, 2014. **34**(2): p. 160-73.
53. Taniguchi-Watanabe, S., et al., *Biochemical classification of tauopathies by immunoblot, protein sequence and mass spectrometric analyses of sarkosyl-insoluble and trypsin-resistant tau*. Acta Neuropathol, 2016. **131**(2): p. 267-280.
54. Dickson, D.W., et al., *Neuropathology of variants of progressive supranuclear palsy*. Curr Opin Neurol, 2010. **23**(4): p. 394-400.
55. Ouchi, H., et al., *Pathology and sensitivity of current clinical criteria in corticobasal syndrome*. Mov Disord, 2014. **29**(2): p. 238-44.
56. Ling, H., et al., *Does corticobasal degeneration exist? A clinicopathological re-evaluation*. Brain, 2010. **133**(Pt 7): p. 2045-57.
57. Mukaetova-Ladinska, E.B., et al., *Biochemical and anatomical redistribution of tau protein in Alzheimer's disease*. Am J Pathol, 1993. **143**(2): p. 565-78.

58. Leuzy, A., et al., *Tau PET imaging in neurodegenerative tauopathies-still a challenge*. Mol Psychiatry, 2019. **24**(8): p. 1112-1134.
59. Leuzy, A., et al., *In vivo Detection of Alzheimer's Disease*. Yale J Biol Med, 2018. **91**(3): p. 291-300.
60. Jack, C.R., Jr., et al., *A/T/N: An unbiased descriptive classification scheme for Alzheimer disease biomarkers*. Neurology, 2016. **87**(5): p. 539-47.
61. Hsiao, I.T., et al., *Correlation of early-phase 18F-florbetapir (AV-45/Amyvid) PET images to FDG images: preliminary studies*. Eur J Nucl Med Mol Imaging, 2012. **39**(4): p. 613-20.
62. Daerr, S., et al., *Evaluation of early-phase [(18)F]-florbetaben PET acquisition in clinical routine cases*. Neuroimage Clin, 2017. **14**: p. 77-86.
63. Tiepolt, S., et al., *Early [(18)F]florbetaben and [(11)C]PiB PET images are a surrogate biomarker of neuronal injury in Alzheimer's disease*. Eur J Nucl Med Mol Imaging, 2016. **43**(9): p. 1700-9.
64. Florek, L., et al., *Dual Time-Point [18F]Florbetaben PET Delivers Dual Biomarker Information in Mild Cognitive Impairment and Alzheimer's Disease*. J Alzheimers Dis, 2018. **66**(3): p. 1105-1116.
65. Meyer, P.T., et al., *Dual-biomarker imaging of regional cerebral amyloid load and neuronal activity in dementia with PET and 11C-labeled Pittsburgh compound B*. J Nucl Med, 2011. **52**(3): p. 393-400.
66. Brendel, M., et al., *Perfusion-Phase [(18)F]THK5351 Tau-PET Imaging as a Surrogate Marker for Neurodegeneration*. J Alzheimers Dis Rep, 2017. **1**(1): p. 109-113.
67. Rodriguez-Vieitez, E., et al., *Comparability of [(18)F]THK5317 and [(11)C]PiB blood flow proxy images with [(18)F]FDG positron emission tomography in Alzheimer's disease*. J Cereb Blood Flow Metab, 2017. **37**(2): p. 740-749.
68. Rostomian, A.H., et al., *Early 11C-PIB frames and 18F-FDG PET measures are comparable: a study validated in a cohort of AD and FTLN patients*. J Nucl Med, 2011. **52**(2): p. 173-9.
69. Hashimoto, H., et al., *Radiosynthesis, photoisomerization, biodistribution, and metabolite analysis of 11C-PBB3 as a clinically useful PET probe for imaging of tau pathology*. J Nucl Med, 2014. **55**(9): p. 1532-8.
70. Kimura, Y., et al., *PET Quantification of Tau Pathology in Human Brain with 11C-PBB3*. J Nucl Med, 2015. **56**(9): p. 1359-65.
71. Wood, H., *Alzheimer disease: [11C]PBB3--a new PET ligand that identifies tau pathology in the brains of patients with AD*. Nat Rev Neurol, 2013. **9**(11): p. 599.
72. Lemoine, L., et al., *Comparative binding properties of the tau PET tracers THK5117, THK5351, PBB3, and T807 in postmortem Alzheimer brains*. Alzheimers Res Ther, 2017. **9**(1): p. 96.
73. Harada, R., et al., *18F-THK5351: A Novel PET Radiotracer for Imaging Neurofibrillary Pathology in Alzheimer Disease*. J Nucl Med, 2016. **57**(2): p. 208-14.
74. Harada, R., et al., *[(18)F]THK-5117 PET for assessing neurofibrillary pathology in Alzheimer's disease*. Eur J Nucl Med Mol Imaging, 2015. **42**(7): p. 1052-61.
75. Marquie, M., et al., *Validating novel tau positron emission tomography tracer [F-18]-AV-1451 (T807) on postmortem brain tissue*. Ann Neurol, 2015. **78**(5): p. 787-800.

76. Ono, M., et al., *Distinct binding of PET ligands PBB3 and AV-1451 to tau fibril strains in neurodegenerative tauopathies*. Brain, 2017. **140**(3): p. 764-780.
77. Johnson, K.A., et al., *Tau positron emission tomographic imaging in aging and early Alzheimer disease*. Ann Neurol, 2016. **79**(1): p. 110-9.
78. Scholl, M., et al., *PET Imaging of Tau Deposition in the Aging Human Brain*. Neuron, 2016. **89**(5): p. 971-982.
79. Maruyama, M., et al., *Imaging of tau pathology in a tauopathy mouse model and in Alzheimer patients compared to normal controls*. Neuron, 2013. **79**(6): p. 1094-108.
80. Brendel, M., et al., *[(18)F]-THK5351 PET Correlates with Topology and Symptom Severity in Progressive Supranuclear Palsy*. Front Aging Neurosci, 2017. **9**: p. 440.
81. Fleisher, A.S., et al., *Positron Emission Tomography Imaging With [18F]flortaucipir and Postmortem Assessment of Alzheimer Disease Neuropathologic Changes*. JAMA Neurol, 2020. **77**(7): p. 829-839.
82. Okamura, N., et al., *Non-invasive assessment of Alzheimer's disease neurofibrillary pathology using 18F-THK5105 PET*. Brain, 2014. **137**(Pt 6): p. 1762-71.
83. Ishiki, A., et al., *Longitudinal Assessment of Tau Pathology in Patients with Alzheimer's Disease Using [18F]THK-5117 Positron Emission Tomography*. PLoS One, 2015. **10**(10): p. e0140311.
84. Chien, D.T., et al., *Early clinical PET imaging results with the novel PHF-tau radioligand [F-18]-T807*. J Alzheimers Dis, 2013. **34**(2): p. 457-68.
85. Lowe, V.J., et al., *An autoradiographic evaluation of AV-1451 Tau PET in dementia*. Acta Neuropathol Commun, 2016. **4**(1): p. 58.
86. Xia, C.F., et al., *[(18)F]T807, a novel tau positron emission tomography imaging agent for Alzheimer's disease*. Alzheimers Dement, 2013. **9**(6): p. 666-76.
87. Brier, M.R., et al., *Tau and Abeta imaging, CSF measures, and cognition in Alzheimer's disease*. Sci Transl Med, 2016. **8**(338): p. 338ra66.
88. Cho, H., et al., *In vivo cortical spreading pattern of tau and amyloid in the Alzheimer disease spectrum*. Ann Neurol, 2016. **80**(2): p. 247-58.
89. Cho, H., et al., *Tau PET in Alzheimer disease and mild cognitive impairment*. Neurology, 2016. **87**(4): p. 375-83.
90. Gordon, B.A., et al., *The relationship between cerebrospinal fluid markers of Alzheimer pathology and positron emission tomography tau imaging*. Brain, 2016. **139**(Pt 8): p. 2249-60.
91. Pontecorvo, M.J., et al., *Relationships between flortaucipir PET tau binding and amyloid burden, clinical diagnosis, age and cognition*. Brain, 2017. **140**(3): p. 748-763.
92. Wang, L., et al., *Evaluation of Tau Imaging in Staging Alzheimer Disease and Revealing Interactions Between beta-Amyloid and Tauopathy*. JAMA Neurol, 2016. **73**(9): p. 1070-7.
93. Jang, Y.K., et al., *Head to head comparison of [(18)F] AV-1451 and [(18)F] THK5351 for tau imaging in Alzheimer's disease and frontotemporal dementia*. Eur J Nucl Med Mol Imaging, 2018. **45**(3): p. 432-442.

94. Marquie, M., et al., *[F-18]-AV-1451 binding correlates with postmortem neurofibrillary tangle Braak staging*. *Acta Neuropathol*, 2017. **134**(4): p. 619-628.
95. Dronse, J., et al., *In vivo Patterns of Tau Pathology, Amyloid-beta Burden, and Neuronal Dysfunction in Clinical Variants of Alzheimer's Disease*. *J Alzheimers Dis*, 2017. **55**(2): p. 465-471.
96. Ossenkoppele, R., et al., *Associations between tau, Abeta, and cortical thickness with cognition in Alzheimer disease*. *Neurology*, 2019. **92**(6): p. e601-e612.
97. Tosun, D., et al., *Association between tau deposition and antecedent amyloid-beta accumulation rates in normal and early symptomatic individuals*. *Brain*, 2017. **140**(5): p. 1499-1512.
98. Bejanin, A., et al., *Tau pathology and neurodegeneration contribute to cognitive impairment in Alzheimer's disease*. *Brain*, 2017. **140**(12): p. 3286-3300.
99. Buckley, R.F., et al., *Region-Specific Association of Subjective Cognitive Decline With Tauopathy Independent of Global beta-Amyloid Burden*. *JAMA Neurol*, 2017. **74**(12): p. 1455-1463.
100. Phillips, J.S., et al., *Tau PET imaging predicts cognition in atypical variants of Alzheimer's disease*. *Hum Brain Mapp*, 2018. **39**(2): p. 691-708.
101. Malpetti, M., et al., *Microglial activation and tau burden predict cognitive decline in Alzheimer's disease*. *Brain*, 2020. **143**(5): p. 1588-1602.
102. Digma, L.A., et al., *Tau and atrophy: domain-specific relationships with cognition*. *Alzheimers Res Ther*, 2019. **11**(1): p. 65.
103. Villemagne, V.L., et al., *Amyloid beta deposition, neurodegeneration, and cognitive decline in sporadic Alzheimer's disease: a prospective cohort study*. *Lancet Neurol*, 2013. **12**(4): p. 357-67.
104. Ishiki, A., et al., *Tau imaging with [(18) F]THK-5351 in progressive supranuclear palsy*. *Eur J Neurol*, 2017. **24**(1): p. 130-136.
105. Shimizu, S., et al., *Case of progressive supranuclear palsy detected by tau imaging with [(18) F]THK-5351 before the appearance of characteristic clinical features*. *Geriatr Gerontol Int*, 2018. **18**(3): p. 501-502.
106. Schonhaut, D.R., et al., *(18) F-flortaucipir tau positron emission tomography distinguishes established progressive supranuclear palsy from controls and Parkinson disease: A multicenter study*. *Ann Neurol*, 2017. **82**(4): p. 622-634.
107. Smith, R., et al., *Increased basal ganglia binding of (18) F-AV-1451 in patients with progressive supranuclear palsy*. *Mov Disord*, 2017. **32**(1): p. 108-114.
108. Whitwell, J.L., et al., *[(18) F]AV-1451 tau positron emission tomography in progressive supranuclear palsy*. *Mov Disord*, 2017. **32**(1): p. 124-133.
109. Hammes, J., et al., *Elevated in vivo [18F]-AV-1451 uptake in a patient with progressive supranuclear palsy*. *Mov Disord*, 2017. **32**(1): p. 170-171.
110. Kikuchi, A., et al., *In vivo visualization of tau deposits in corticobasal syndrome by 18F-THK5351 PET*. *Neurology*, 2016. **87**(22): p. 2309-2316.
111. Smith, R., et al., *In vivo retention of (18)F-AV-1451 in corticobasal syndrome*. *Neurology*, 2017. **89**(8): p. 845-853.
112. Cho, H., et al., *(18)F-AV-1451 binds to motor-related subcortical gray and white matter in corticobasal syndrome*. *Neurology*, 2017. **89**(11): p. 1170-1178.

113. Chiotis, K., et al., *Longitudinal changes of tau PET imaging in relation to hypometabolism in prodromal and Alzheimer's disease dementia*. Mol Psychiatry, 2018. **23**(7): p. 1666-1673.
114. McMillan, C.T., et al., *Multimodal evaluation demonstrates in vivo (18)F-AV-1451 uptake in autopsy-confirmed corticobasal degeneration*. Acta Neuropathol, 2016. **132**(6): p. 935-937.
115. Josephs, K.A., et al., *[18F]AV-1451 tau-PET uptake does correlate with quantitatively measured 4R-tau burden in autopsy-confirmed corticobasal degeneration*. Acta Neuropathol, 2016. **132**(6): p. 931-933.
116. Niccolini, F., et al., *Disease-related patterns of in vivo pathology in Corticobasal syndrome*. Eur J Nucl Med Mol Imaging, 2018. **45**(13): p. 2413-2425.
117. Vermeiren, C., et al., *The tau positron-emission tomography tracer AV-1451 binds with similar affinities to tau fibrils and monoamine oxidases*. Mov Disord, 2018. **33**(2): p. 273-281.
118. Hostetler, E.D., et al., *Preclinical Characterization of 18F-MK-6240, a Promising PET Tracer for In Vivo Quantification of Human Neurofibrillary Tangles*. J Nucl Med, 2016. **57**(10): p. 1599-1606.
119. Ishiki, A., et al., *Neuroimaging-pathological correlations of [(18)F]THK5351 PET in progressive supranuclear palsy*. Acta Neuropathol Commun, 2018. **6**(1): p. 53.
120. Harada, R., et al., *Correlations of (18)F-THK5351 PET with Postmortem Burden of Tau and Astrogliosis in Alzheimer Disease*. J Nucl Med, 2018. **59**(4): p. 671-674.
121. Ng, K.P., et al., *Monoamine oxidase B inhibitor, selegiline, reduces (18)F-THK5351 uptake in the human brain*. Alzheimers Res Ther, 2017. **9**(1): p. 25.
122. Ng, K.P., et al., *Rasagiline, a monoamine oxidase B inhibitor, reduces in vivo [(18)F]THK5351 uptake in progressive supranuclear palsy*. Neuroimage Clin, 2019. **24**: p. 102091.
123. Saint-Aubert, L., et al., *Tau PET imaging: present and future directions*. Mol Neurodegener, 2017. **12**(1): p. 19.
124. Marquie, M., et al., *Lessons learned about [F-18]-AV-1451 off-target binding from an autopsy-confirmed Parkinson's case*. Acta Neuropathol Commun, 2017. **5**(1): p. 75.
125. Coakeley, S., et al., *[(18)F]AV-1451 binding to neuromelanin in the substantia nigra in PD and PSP*. Brain Struct Funct, 2018. **223**(2): p. 589-595.
126. Baker, S.L., A. Maass, and W.J. Jagust, *Considerations and code for partial volume correcting [(18)F]-AV-1451 tau PET data*. Data Brief, 2017. **15**: p. 648-657.
127. Vemuri, P., et al., *Tau-PET uptake: Regional variation in average SUVR and impact of amyloid deposition*. Alzheimers Dement (Amst), 2017. **6**: p. 21-30.
128. Winer, J.R., et al., *Associations Between Tau, beta-Amyloid, and Cognition in Parkinson Disease*. JAMA Neurol, 2018. **75**(2): p. 227-235.
129. Fichou, Y., et al., *The elusive tau molecular structures: can we translate the recent breakthroughs into new targets for intervention?* Acta Neuropathol Commun, 2019. **7**(1): p. 31.
130. Kroth, H., et al., *Discovery and preclinical characterization of [(18)F]PI-2620, a next-generation tau PET tracer for the assessment of tau pathology in*

- Alzheimer's disease and other tauopathies*. Eur J Nucl Med Mol Imaging, 2019. **46**(10): p. 2178-2189.
131. Agüero, C., et al., *Autoradiography validation of novel tau PET tracer [¹⁸F]-MK-6240 on human postmortem brain tissue*. Acta Neuropathol Commun, 2019. **7**(1): p. 37.
 132. Sanabria Bohorquez, S., et al., *[¹⁸F]GTP1 (Genentech Tau Probe 1), a radioligand for detecting neurofibrillary tangle tau pathology in Alzheimer's disease*. Eur J Nucl Med Mol Imaging, 2019. **46**(10): p. 2077-2089.
 133. Honer, M., et al., *Preclinical Evaluation of (¹⁸F)-RO6958948, (¹¹C)-RO6931643, and (¹¹C)-RO6924963 as Novel PET Radiotracers for Imaging Tau Aggregates in Alzheimer Disease*. J Nucl Med, 2018. **59**(4): p. 675-681.
 134. Beyer, L. and M. Brendel, *Imaging of Tau Pathology in Neurodegenerative Diseases: An Update*. Semin Nucl Med, 2020.
 135. Mueller, A., et al., *Tau PET imaging with (¹⁸F)-PI-2620 in Patients with Alzheimer Disease and Healthy Controls: A First-in-Humans Study*. J Nucl Med, 2020. **61**(6): p. 911-919.
 136. Mormino, E.C., et al., *Tau PET imaging with (¹⁸F)-PI-2620 in aging and neurodegenerative diseases*. Eur J Nucl Med Mol Imaging, 2020.
 137. Barret, O., et al., *INITIAL CLINICAL PET STUDIES WITH THE NOVEL TAU AGENT 18-F PI-2620 IN ALZHEIMER'S DISEASE AND CONTROLS*. Journal of Nuclear Medicine, 2017. **58**: p. 630-630.
 138. Villemagne, V., et al., *Evaluation of ¹⁸F-PI-2620, a second-generation selective tau tracer for the assessment of Alzheimer's and non-Alzheimer's tauopathies*. Journal of Nuclear Medicine, 2018. **59**: p. 410-410.
 139. Bullich, S., et al., *Evaluation of Dosimetry, Quantitative Methods, and Test-Retest Variability of (¹⁸F)-PI-2620 PET for the Assessment of Tau Deposits in the Human Brain*. J Nucl Med, 2020. **61**(6): p. 920-927.
 140. Mormino, E.C., et al., *P4-315: TAU PET IMAGING WITH 18F-PI2620 IN AGING AND ALZHEIMER'S DISEASE*. Alzheimer's & Dementia, 2018. **14**(7S_Part_30): p. P1577-P1578.
 141. Brendel, M., et al., *Assessment of 18F-PI-2620 as a Biomarker in Progressive Supranuclear Palsy*. JAMA Neurol, 2020. **77**(11): p. 1408-1419.

Acknowledgements

I owe thanks to many people who helped me during my doctoral study. First of all, I would like to express my greatest appreciation to my supervisors Prof. Dr. Peter Bartenstein and Dr. Matthias Brendel for offering me such an excellent opportunity to perform my doctoral study on such a fascinating and inspiring research topic in their team. Since our first contact, I was deeply impressed by Prof. Dr. Peter Bartenstein's modesty and gentleness and Dr. Matthias Brendel's passion and enthusiasm for science. It is of great fortune for me to have the two best supervisors in the world! Additional thanks to Dr. Matthias Brendel for his continuous guidance and support throughout my doctoral study. He is not only a good supervisor, but also a superior mentor to me. My doctoral study here will be a precious unforgettable experience in my life.

I would also like to thank all my colleagues in our team who created an enjoyable atmosphere and helped me. I would like to highlight Dr. Leonie Beyer and Dr. Maximilian Scheifele, to whom I am truly grateful for their cooperation on the projects.

My heartfelt thank also goes to my dear friends Sicheng Tang, Pan Gao, Bingwen Yu, Dongxu Zhao, and Yi Tan. We had many happy days and moments over these years in Munich.

I sincerely appreciate the China Scholarship Council for providing me economic support during my doctoral study.

In particular, I would like to give my special gratitude to my husband Qilin Tang for always encouraging me and giving valuable advices and endless help. Thank him for always being by my side. I can hardly achieve what I have done without him!

At last, I would like to express my deepest respect and gratitude to my family for their endless love, inspiration and support.